METHODS OF MULTIPARAMETER INVERSION OF SEISMIC DATA USING THE ACOUSTIC AND ELASTIC BORN APPROXIMATIONS

Thesis by

Ronan Le Bras

In Partial Fulfillment of the Requirements

for the Degree of

Doctor of Philosophy

California Institute of Technology

Pasadena, California

1985

(Submitted June 4th, 1985)

A mes parents,

qui m'ont enseigné la valeur du travail.

Aknowledgements

Throughout my stay at the Seismo-Lab, I have enjoyed the company of the faculty and of my colleague graduate students, past and present. I am very happy to have had my first contact with American life in this environment. Bernard Minster was my initial adviser for too short a period and motivated me to pursue research in Geophysics. This thesis has been conducted under the supervision of Robert Clayton from whom I learned a great many things, and whose best quality among many was always to be available.

Don Helmberger and Dave Harkrider provided support for part of my graduate student career and were always ready for advice. Tom Ahrens was a good academic adviser. Hsui-Lin Liu, Steve Hartzell and Tom Heaton helped me with strong ground motion modeling and data in the early stages of my career here.

The French foreign service allowed me to accomplish my national service as a research assistant at the Seismo-Lab, and my thanks go to Don Anderson who made some of the necessary arrangements.

Mario Vassiliou and Chris Creaven introduced me to many subtleties of the English language. Actually, Mario introduced me to subtleties of many languages. Holly Eissler, Steve Grand and Gene Humpheys have been great classmates and friends. Jiajun Zhang was a good tennis partner and friend. Henry Nataf was a good friend and conversationalist.

Marianne Walck is gratefully aknowledged for her organization of memorable ski trips and of the softball team, which enlightened many summer afternoons. I also want to thank my officemates, Ed Corbett, Tom Hearn, Mark Richards and Doug

Schmitt for conversations about science and other diverse topics.

This thesis owes a lot to the constant positive attitude of John Louie (how do you manage that, John ?), with whom I had a lot of discussions about seismic experiments and signal processing. I had interesting discussions with Christof Stork about tomography and Born approximation. Luciana Astiz read this thesis very carefully and critically. Lazlo Lenches drafted the most professional looking figures in this thesis.

A fellowship from Phillips Petroleum Company supported me financially during part of my stay at the Seimo-Lab.

Abstract

This thesis presents two different forms of the Born approximations for acoustic and elastic wavefields and discusses their application to the inversion of seismic data. The Born approximation is valid for small amplitude heterogeneities superimposed over a slowly varying background. The first method is related to frequency-wavenumber migration methods. It is shown to properly recover two independent acoustic parameters within the bandpass of the source time function of the experiment for contrasts of about 5 percent from data generated using an exact theory for flat interfaces. The independent determination of two parameters is shown to depend on the angle coverage of the medium. For surface data, the impedance profile is well recovered.

The second method explored is mathematically similar to iterative tomographic methods recently introduced in the geophysical literature. Its basis is an integral relation between the scattered wavefield and the medium parameters obtained after applying a far-field approximation to the first-order Born approximation. The Davidon-Fletcher-Powell algorithm is used since it converges faster than the steepest descent method. It consists essentially of successive backprojections of the recorded wavefield, with angular and propagation weighing coefficients for density and bulk modulus. After each backprojection, the forward problem is computed and the residual evaluated. Each backprojection is similar to a before-stack Kirchhoff migration and is therefore readily applicable to seismic data. Several examples of reconstruction for simple point scatterer models are performed. Recovery of the amplitudes of the anomalies are improved with successive iterations. Iterations also improve the sharpness of the images.

The elastic Born approximation, with the addition of a far-field approximation is shown to correspond physically to a sum of WKBJ-asymptotic scattered rays. Four types of scattered rays enter in the sum, corresponding to P-P, P-S, S-P and S-S pairs of incident-scattered rays. Incident rays propagate in the background medium, interacting only once with the scatterers. Scattered rays propagate as if in the background medium, with no interaction with the scatterers. An example of P-wave impedance inversion is performed on a VSP data set consisting of three offsets recorded in two wells.

Table of Contents

Introduction

The standard processing techniques for analyzing seismic reflection profiles mostly aim at locating "reflectors" in the earth that can be identified as boundaries between geological units. The reflections arise from contrasts in elastic parameters and density between different media in the Earth. The standard processing methods take advantage of the offset information to do a velocity analysis using for example semblance methods (Taner and Koehler,1969) and the traces are then stacked according to the move-out velocity determined by the velocity spectrum. In so doing, the variation of the amplitude with offset is lost. This variation contains important information, since it is a function of the variation of the reflection coefficient with the angle of incidence, the transmission losses, the anelastic attenuation, and the radiation pattern of the source. Some of these effects can be accounted for. For instance, the radiation pattern of the source used can be estimated. The anelastic attenuation effect on a reflected wave is a function of the difference in paths' length for different offsets. For a simple Q model, this can also be accounted for. The transmission losses at strong impedance contrasts are more delicate to take into account; however, if the medium doesn't present such contrasts, they can be neglected. If an acoustic model is chosen to simulate the experiment, the reflection coefficient depends upon the contrast in any two independent physical variables, density, bulk modulus, impedance and velocity. It is a function of the Lamé 's parameters and density in an elastic model. Usually, the stacked midpoint gathers are assumed to represent zero-offset

reflections, the amplitudes of which are proportional to the impedance contrast. In recent years methods to infer the nature of reflectors through the impedance contrast giving rise to the reflections have been presented in the literature (Oldenburg et al.,1983, Carrion and Patton,1983). Those methods are referred to as inversions as opposed to the more commonly used migrations, since they aim at estimating the medium parameters rather than at getting the image of a reflector.

The Born approximation for scattered wavefield was first introduced in physics to study particle and wave interactions and is intensively used in that field (e.g., Schiff, 1968). The basic assumption behind the approximation is that the incident wave is not very perturbed by the interaction, or that the scattered wave has a much smaller amplitude than the incident wave. This type of approximation to a wavefield has also been used in geophysics. Tanimoto (1984a, 1984b) used the Born approximation to calculate long period surface waves in a slightly heterogeneous earth. In seismic reflection several authors, working on the problem of seismic data inversion have used the approximation. Bleistein and Cohen (1982) consider the acoustic wave equation for a uniform medium and introduce a velocity perturbation into the differential equation. They deduce an integral relation between the perturbation and the scattered wavefield. They apply this method on stacked common midpoint data and therefore loose the offset information. Raz (1981) pointed out that it is necessary to have data for several offsets to be able to separate bulk modulus from density variations. Knowing both the density and the bulk modulus could prove to be a powerful way of better identifying the materials composing the underlying medium (Gardner et al., 1974). An exploitation of the variation of the amplitude of seismic data with offset to deduce rheology properties has been proposed by Gassaway and Richgels

(1983). Ostrander (1984) shows that the variations of the amplitude of a reflected wave with offset yields precious information about the Poisson's ratio of anomalously high amplitude reflections (bright spot). He applies this on data recorded in an oil field and is able to discriminate convincingly between a gas saturated rock layer and a basalt layer from their Poisson's ratio.

Clayton and Stolt (1981) proposed a method that fully exploits the offset information contained in standard data. It is based on a Born model for the reflected field. They use the exact equation in a two dimensionally varying medium and introduce perturbations in both density and bulk modulus. Their approach is an attempt to retrieve more information and separate these two variables. For a multi-offset survey it becomes theoretically possible to invert the data for the relative variations of these two variables with depth and distance along the recording line or midpoint.
Their approach to the inversion problem is in the frequency-wavenumber domain. They show that the wavefield under the Born approximation can be expressed as a linear combination of the acoustic parameters, density and bulk modulus. This relationship is obtained in the midpoint-offset and depth wavenumber space. The method is presented in more detail in the first part of Chapter 1.

Examples of applications of the frequency-wavenumber method are performed on synthetic seismograms and discussed in the second chapter of this dissertation. Both one dimensionally varying models and two dimensionally varying models are presented and discussed.

Using the same linear approximation as Clayton and Stolt (1981)(Born approximation) to the acoustic wavefield, we further simplify its expression. A far-field approximation is applied. This is presented in the second part of Chapter 1. Using

this far-field approximation, an expression for the scattered wavefield under the Born approximation is obtained in the space-time domain. The seismograms may be computed as a linear integral operator over the model space.

Since the problem is reduced to a linear one, the theory of linear inversion can now be applied. However, the very large size of the seismic reflection typical data sets makes a classical least-square inversion impractical. Instead, we use a different approach, similar to Nercessian et al. (1984). The idea behind the method, like in any inversion method, is to reach the minimum of an objective function (L_2 norm of the residuals). The minimum of the function is approached in an iterative manner. This falls into the class of optimization problems (Fletcher, 1980). Among several methods available to solve such problems, the Davidon-Fletcher-Powell is one of the more powerful and presents several advantages. For a quadratic function, it converges in a finite number of iterations and provides us with an estimate of the model's variance. Each step of the Davidon-Fletcher-Powell method is essentially a backprojection of the residuals obtained from the previous iterations and resembles tomographic methods applied to travel time residuals (e.g., Humphreys et al., 1984) with the added advantage of allowing us to know the resolution matrix at the convergence point. The term of backprojection is used here in a generalized sense since the projection is not along straight lines as is the case in tomographic imaging used in the medical profession. Clayton and Comer (1985) have used a similar type of backprojection to invert travel time data for slownesses in a whole earth model. In their case, the data (travel times) are projected along curved rays. In our case, the wavefield is projected along constant time trajectories. When the background velocity is constant these trajectories are ellipses but they are arbitrary when the background velocity is a more

general function of space.

The basic iteration step is therefore very similar to a before-stack Kirchhoff migration of the residuals. The only difference is that angular coefficients are applied to obtain two different sections representing the density variations and the bulk modulus variations, respectively.

Several applications of the tomographic-like method are presented in Chapter 3. The data used are generated using a direct Born approximation approach in some of the examples and a finite-difference formulation for one of the models. All examples discussed in that part present two-dimensional variations.

Chapter 4 develops the elastic counterpart of the acoustic theory presented in the previous chapters. A comparison of the exact reflection coefficient for an elastic interface with the coefficients derived under the Born approximation is presented and discussed. The equivalent of the method developed in Chapter 3 for an acoustic model is adapted to the elastic model. The same types of approximations (Born, WKBJ, far-field) are developed, following the formulation introduced by Clayton (1981). The iterative backprojection method can then be applied to obtain three images representing the relative variations of the two Lamé 's constants and density. The formulation of the method is more difficult for the elastic model, since we have to deal simultaneously with displacements, which are the recorded data and potentials (compressional and shear). Potentials are used since they can be expressed and propagated in a simpler way than displacements.

The elastic model is, of course, more accurate to describe seismic waves and the amplitudes should be interpreted in terms of the elastic model. This is especially true in cases where dips are substantial or when the incidence angle on reflectors is far

from normal, because of the more efficient shear-wave conversions. Also, in the case of a Vertical Seismic Profile experiment, incidence angles may vary a lot and give rise to heavy conversions to shear waves. The backprojection method is particularly suitable in the case of a VSP experiment since it is adaptable to any source-receivers geometries.

Chapter 5 presents an application of the Born inversion by backprojection on a VSP data set.

Chapter 1

Presentation of a Born Approximation and Far-field Approximation for a Scattered Acoustic Wavefield

Abstract

The Born approximation to an acoustic wavefield is introduced in the case of an acoustic medium that can be considered as the sum of a medium with slowly varying acoustic parameters and superimposed small amplitude density and bulk-modulus anomalies. The simple case of a layer over a half-space is discussed and illustrates the limitations of the Born approximation: inaccuracy close to the critical angle and beyond, and inaccuracy for large differences in the media parameters. A further, far-field approximation is introduced in the expression for the scattered wavefield. The wavefield can then be expressed as a sum of scattered asymptotic rays.

Introduction

The general topic of this thesis is the use of the Born approximation in the analysis of seismic reflection data. The Born approximation can be derived from a perturbation analysis on the acoustic wave equation supposing small variations of the acoustic parameters. Clayton and Stolt (1981) have used this approximation and derived an expression for the scattered wavefield in the frequency-wavenumber space. From this expression, a method was devised to invert seismic data by identifying

them to the expression obtained under the approximation. The wavefield is found to be a linear combination of the functions describing the variations of density and bulk-modulus in the midpoint-wavenumber and depth-wavenumber space. Thus, a simple linear inversion may be applied to retrieve these two functions from the transformed data. An outline of the calculations leading to the expression of the wavefield as a function of wavenumbers is presented in the first part of this chapter. In the very simple case of one interface between two half-spaces, the Born approximation is shown to correspond to a simple linearization of the Cagniard-de Hoop reflection coefficient. A comparison of the exact reflected wave with the wave computed under the approximation is presented and discussed.

From Clayton and Stolt's (1981) expression for the scattered wavefield, we introduce a far-field approximation. Using the stationary phase method on the expression for the wavefield we get an expression in the time-space domain. The expression obtained can be analyzed term by term. It is simple to interpret it intuitively. It consists of a time delay term obtainable from elementary ray theory, a geometrical spreading factor that can also be obtained from ray theory in the absence of caustics and a reflection coefficient factor, which contains the information about the scattering properties of the medium. Using this simplified expression of the scattered wavefield, we can construct synthetic seismograms. A comparison between these synthetic seismograms generated using the Born and far-field approximations and synthetic seismograms generated using a finite difference method is presented.

Born approximation in the frequency-wavenumber domain

First, we present a short outline of the theory developed by Clayton and Stolt (1981) and a rapid review of the theory.

Consider an acoustic medium characterized by its bulk modulus κ and density ρ. Both of these parameters are space variables. We consider that each is a sum of two functions. One of these functions is slowly varying. We note them with the subscript 0 (κ_0 and ρ_0). Superimposed on that background medium is a rapidly varying (high spatial frequency) medium. We note them $\Delta\kappa$ and $\Delta\rho$. The magnitude of the superimposed medium is supposed to be much smaller than the background medium. Let P be the pressure field. It satisfies the wave equation in a two-dimensional space:

$$\left[\frac{\omega^2}{\kappa} + \nabla.\frac{1}{\rho}\nabla\right]P = \delta(x-x_0)\delta(z-z_0)S(\omega), \tag{1.1}$$

where x_0 and z_0 are the coordinates of the location of the source and $S(\omega)$ the Fourier transform of the source-time function, ω being the frequency. We can write this differential equation as the action of a linear operator L over the pressure field P :

$$LP = \delta(x-x_0)\delta(z-z_0)S(t). \tag{1.2}$$

The solution to this equation is a Green's function that can be formally written as the inverse of the L operator:

$$G = -L^{-1}. \tag{1.3}$$

This Green's function cannot be obtained analytically in the general case of a laterally varying medium. However, it is possible to calculate it for a background medium with constant acoustic parameters or acoustic parameters that vary slowly

with depth (using the WKBJ approximation in this last case). The Green's function for the background medium is noted G_0. The Green's function for the general medium can be expressed in terms of the Green's function for the slowly varying medium as :

$$G = G_0 + G_0(L - L_0)G. \tag{1.4}$$

This is an exact equation, called the Lippman-Schwinger equation. The first-order Born approximation arises when G on the right-hand side of the equation is replaced with G_0. This is physically justified when the scattered field is small compared to the incident wavefield G_0. Therefore, under the Born approximation, the Green's functions for the general medium is expressed as :

$$G = G_0 + G_0 V G_0. \tag{1.5}$$

The scattering potential V is a linear operator. It is expressed explicitly as :

$$V = \omega^2 \left[\frac{1}{\kappa} - \frac{1}{\kappa_0} \right] + \nabla \cdot \left[\frac{1}{\rho} - \frac{1}{\rho_0} \right] \nabla. \tag{1.6}$$

It is convenient to define the two variables a_1 and a_2 as $a_1 = \frac{\kappa_0}{\kappa} - 1$ and $a_2 = \frac{\rho_0}{\rho} - 1$. The scattering potential is then :

$$V = \omega^2 \frac{a_1}{\kappa_0} + \nabla \cdot \frac{a_2}{\rho_0} \nabla \tag{1.7}$$

The reflection data can be identified as the recorded wavefield minus the direct arrival. The direct arrivals can be approximated by $G_0 S(\omega)$ (in the frequency domain) where $S(\omega)$ is the Fourier transform of the source-time function. Using the

Born approximation, the scattered data can then be identified as :

$$D(x_g, x_s, \omega) = G_0(x_g, 0; x, z) V(x, z) G_0(x, z; x_s, 0) S(\omega), \tag{1.8}$$

where x_g is the abscissa of the geophone location, x_s the abscissa of the source location, both at the surface($z=0$). The variables x and z are repeated, meaning an integration over their domain. This relation between the scattered data field and the scattering potential is a linear relation. We can take advantage of this to invert the data for the parameters defining the rapid variations of the acoustic medium.

Constant background velocity

In the case of a constant background medium (ρ_0 and κ_0 constant), the relation can be reduced to a very simple one in the frequency-wavenumber domain :

$$D(k_g, k_s, \omega) = \frac{-\rho_0}{4 q_s q_g} \left[\frac{\omega^2}{v_0^2} a_1(k_g - k_s, -q_g - q_s) + (q_g q_s - k_g k_s) a_2(k_g - k_s, -q_g - q_s) \right] S(\omega).$$

where k_s and k_g are the horizontal wavenumbers associated with the source and geophone coordinates, respectively. q_s and q_g are defined as :

$$q_x = \frac{-\omega}{v_0} \left(1 - \frac{v_0^2 k_x^2}{\omega^2} \right)^{1/2} \tag{1.9}$$

where the subscript x is either s or g.

Introducing the variable k_z defined as $k_z = -q_g - q_s$ and transforming to the midpoint-offset notation, the wavefield can be expressed as :

$$D(k_m, k_h, \omega) = \frac{-\rho_0}{4} \left[A\,1(k_z, k_m, k_h)\ a_1(k_m, k_z) + A\,2(k_z, k_m, k_h)\ a_2(k_m, k_z) \right] S(\omega).$$

where :

$$A\,1(k_z, k_m, k_h) = \frac{(k_z^2+k_h^2)(k_z^2+k_m^2)}{k_z^4-k_m^2k_h^2} \quad \text{and} \quad A\,2(k_z, k_m, k_h) = \frac{(k_z^2-k_h^2)(k_z^2+k_m^2)}{k_z^4-k_m^2k_h^2}$$

where $k_m = k_g - k_s$ and $k_h = k_g + k_s$ are, respectively, the midpoint and half-offset wavenumbers.

This equation is the basis for the construction of an inverse algorithm to estimate the variations of a_1 and a_2. The basic steps of this algorithm can be easily deduced from it. The algorithm is explicitly explained in Chapter 2, and inversions tested in simple cases.

Before using the inversion algorithm, however, we want to test the validity of the Born approximation on a few examples.

Validity of the Born approximation in the single interface case

To assess the validity of the Born approximation, we compared the Born approximation reflection coefficient with the exact reflection coefficient in the case of a very simple model. The model consists of two adjacent acoustic half-spaces. It was found that the Born approximation in this case is equivalent to linearizing the exact Cagniard-de Hoop reflection coefficient with respect to the relative variations in density and velocity ($\frac{\Delta\rho}{\rho}$ and $\frac{\Delta c}{c}$). This is shown in Appendix A. Summarizing the calculations conducted in that Appendix, the Cagniard-de Hoop reflection coefficient can be approximated as :

$$R(p) \approx \frac{1}{2}\left[\alpha + \frac{\beta}{(1-p^2c_1^2)}\right] \tag{1.10}$$

where:

$$\alpha = \frac{\Delta c}{c} \qquad \beta = \frac{\Delta \rho}{\rho} \qquad p \text{ is the slowness}$$

when the two half-spaces are sufficiently close to each other in terms of their acoustic parameters.

The reflected waves can then be expressed in the following way, using the Cagniard-de Hoop method :

$$\Phi_R(x,0,s) = \frac{F(s)}{\pi} \operatorname{Im} \left\{ \int_0^{i\infty} e^{-s(px+2\eta_1 z_0)} \frac{R(p)}{2\eta_1} dp \right\}. \tag{1.11}$$

F(s) is the Laplace transform of the source time function, Im denotes the imaginary parts, R(p) is the reflection coefficient . Index 1 refers to the half-space containing the source and index 2 to the other one ρ is the density, c the velocity and p the horizontal slowness and η the horizontal slowness.

The path of integration can be continuously deformed such that the quantity $px+2\eta_1 z_0$ is real and can be readily identified to time. The reflected waves computed using the approximation are very comparable to the waves computed using the exact reflection coefficient. To illustrate this, we present Figure 1.1. It shows a comparison of synthetic seismograms computed with the Cagniard-de Hoop method both with and without approximation. The bottom record-section in each figure is the exact theoretical reflected wave for a line source situated in the upper half-space, at two kilometers above the reflector. The record-section at the top of each figure is the reflected wave computed using the Born approximation (or equivalently the linearized Cagniard-de Hoop reflection coefficient). The densities and velocities of the two half-spaces are indicated on the figures.

It is apparent, as expected, that the more different the media are, the more the approximation diverges from the exact expression for the reflected wave. It is, however, good as long as the step variation of the acoustic parameters is small. It also appears that the approximation does better for near-normal incidence angles.

The two examples presented on Figure 1.1 show two different kinds of contrasts between the two half-spaces. The sections to the left are for a 2.5% contrast in velocity and no density contrast. In that case, the amplitude of the reflected wave increases with offset. The amplitudes are very reasonably accurate in the Born approximation section, within 3% of the exact value for the largest offset shown which corresponds to an incidence angle slightly larger than 45° on the interface. The sections on the right are for a contrast of 2.5% in density and no velocity contrast. The amplitudes can be seen to decrease with offset in this case. The approximated section is not distinguishable from the exact section for this case of a model with only density contrast.

The method of inversion described in Clayton and Stolt (1981) should therefore do a good job in retrieving the relative variations in density and velocity, or bulk modulus from the amplitude variation of the reflected waves with offset. The limitations of the method may come from several causes. The transmission losses can modify the amplitude of the reflected wave so that the true relative density and velocity contrasts are not recovered properly. Also the refraction of rays at the interface is not included in the theory. This modifies the true incidence angle and the interpretation of the amplitude of the reflected wave at that angle.

Figure 1.2 presents an illustration of these approximations. It shows record sections for two flat layer models. Synthetic seismograms are computed both exactly and

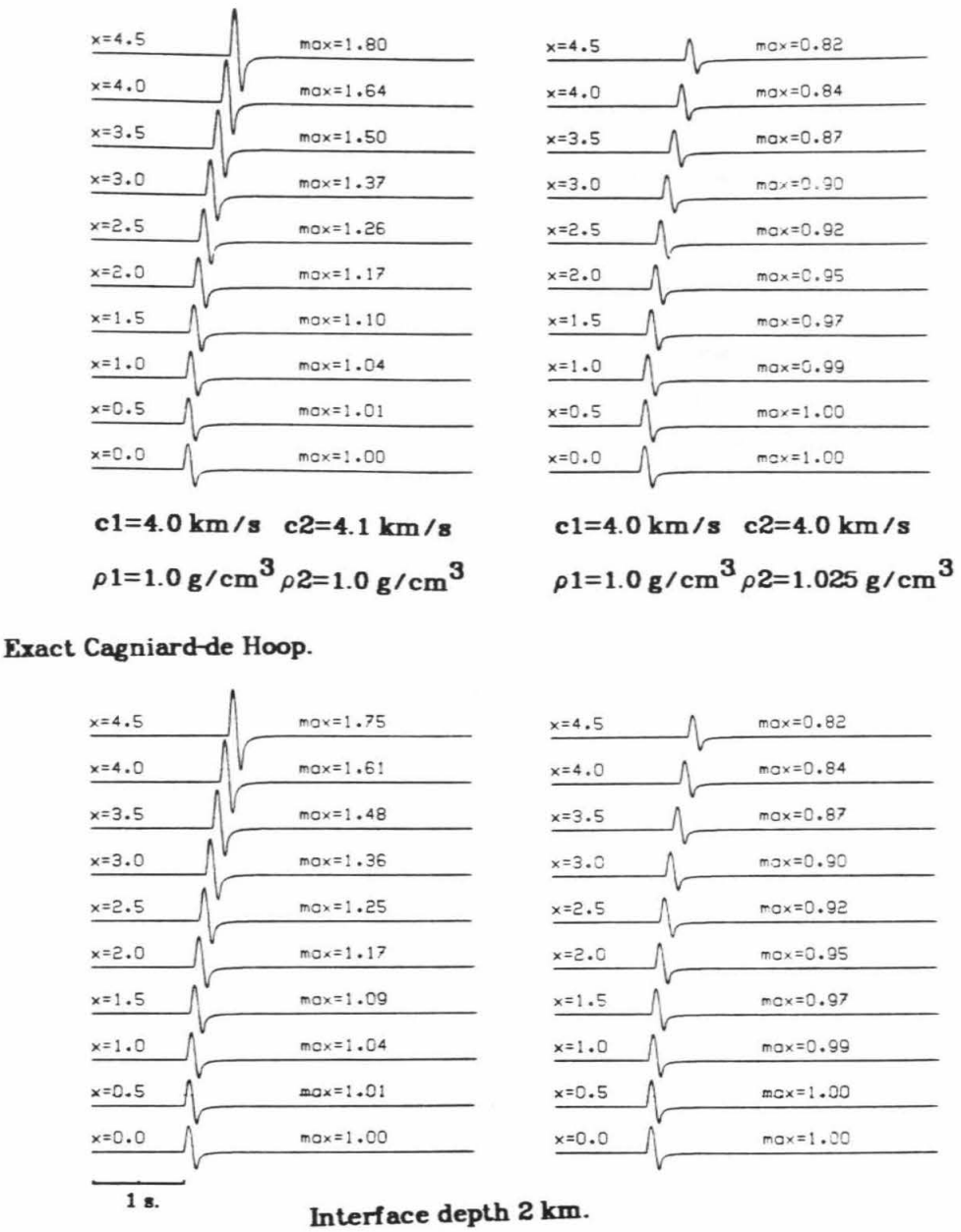

Figure 1.1 - Synthetic acoustic seismograms computed with the exact reflection coefficient (Bottom) and the approximate Born reflection coefficient (Top), for a model with one layer over a half-space. The contrast is only in velocity for the examples to the left and in density for the example to the right.

under the Born approximation using the Cagniard-de Hoop method. The two models are given in the following table :

Table 1.1

	Model 1		Model 2	
	velocity (km/s)	density (g/cm^3)	velocity (km/s)	density (g/cm^3)
Layer 1	4.0	1.0	4.0	1.0
Layer 2	4.5	1.1	4.1	1.0
Half-space	5.0	1.2	4.2	1.1

The two models are different in the sense that Model 1 has a much higher variation from a background of v=4.0 km/s and $\rho = 1.0$ km/cm^3. The figure shows that, as expected, the approximation does better for Model 2 . However, even for this model, with variations of 20% maximum from the background density and 5% from the background velocity, the amplitude at normal incidence from the second reflector is not very well approximated. The variations with offset, however, are fairly accurately reproduced with the Born approximation. For Model 1, the Born model is not accurate. In that case, the critical angle is 62° for the first interface and this corresponds to about 3.9 kms of offset. At that distance, the reflected wave reaches a maximum on the exact section. This is, of course, not well reproduced on the approximate section.

The arrival time effect is small and hardly visible on the figure at that scale, but is nevertheless present. It will introduce an error in the location of the second interface.

Far-field approximation

At the beginning of this chapter, the Born approximation was introduced for the scattered wavefield. The general expression for the wavefield was found to be :

$$D = G_o \, V G_o \, S(\omega) \tag{1.12}$$

where G_o notes the Green's function for a slowly varying background velocity. V is the scattering potential assumed to be small for the approximation to be valid. $S(\omega)$ is the Fourier transform of the source time function.

The Green's function G_o has an analytic expression under the WKBJ (e.g., Aki and Richards, 1980) approximation. In Appendix B, a derivation of a far-field approximation in addition to the Born and WKBJ approximations is performed. The far-field approximation is justified since, in the geometries considered for seismic exploration, the distances traveled by reflected waves vary from a few wavelengths to tens of wavelengths. The result of applying this additional approximation leads to express the wavefield in terms of a sum of geometrical rays.

$$D(x_s, x_g, t) = \int_\Omega d\Omega \, A(x_s, x) \, A(x, x_g) \left[a_1(x) + a_2(x) \cos\theta \right] \dot{S}(t - t_1 - t_2). \tag{1.13}$$

where Ω is the domain of integration of x.

Figure 1.4 illustrates the meaning of each of the terms in the integrand. The first two factors $A(x_s, x)$ and $A(x, x_g)$ represent the geometric spreading attenuation

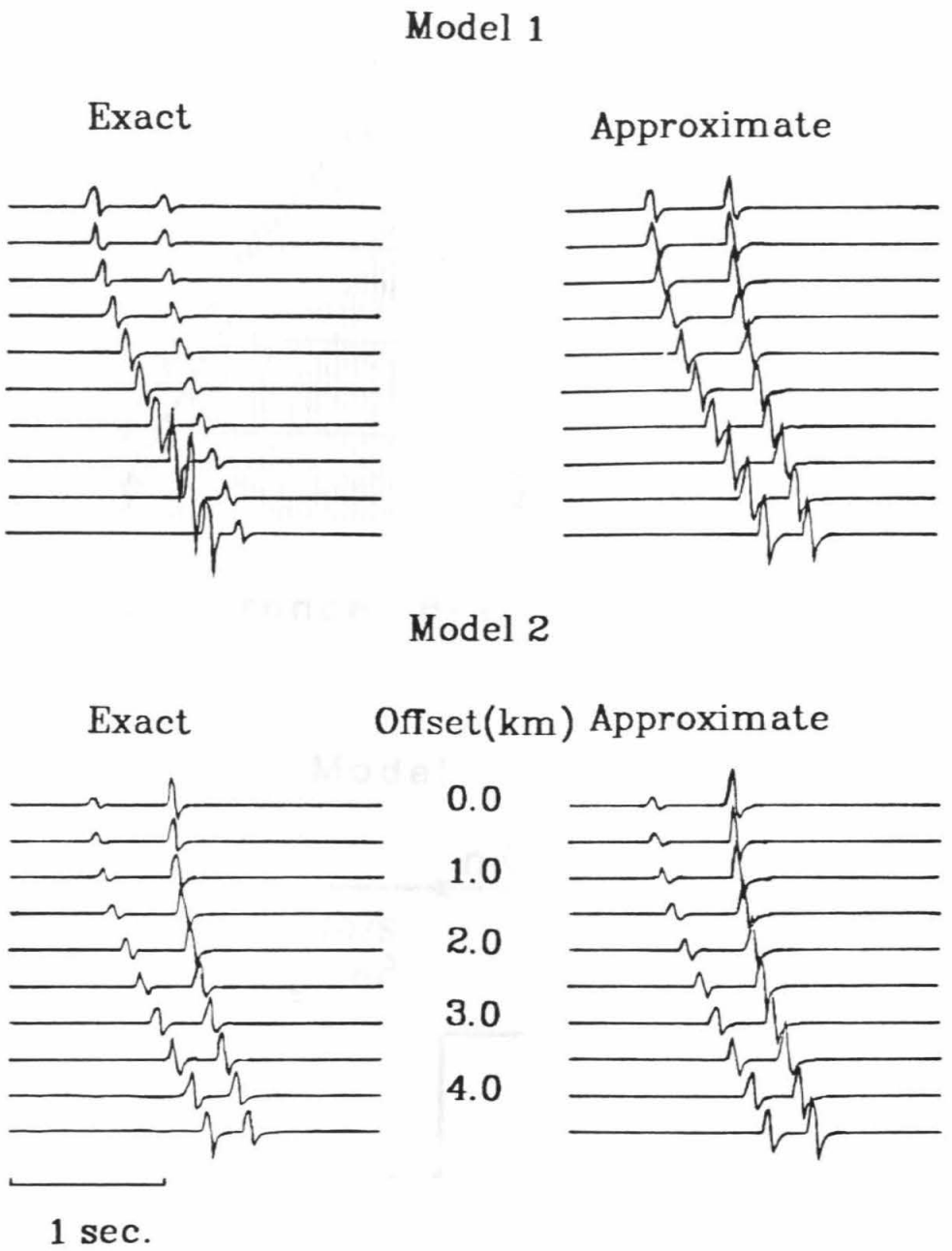

Figure 1.2 - Synthetic acoustic seismograms computed using a Cagniard-de Hoop method. The parameters for these two models are given in Table 1.1.

factors. They can be calculated from ray geometrical considerations. The third factor $a_1 + a_2 \cos\theta$ is an angle dependent scattering coefficient. This provides the information on the nature of the scatterers in the medium. Figure 1.5 shows the variations of this factor as a function of the angle between an incident and scattered ray for different types of scatterers. It illustrates the uniform radiation pattern for a bulk modulus scatterer and the two-lobed pattern for a density scatterer. This translates into a scattering pattern dominant in the backward direction for an impedance scatterer and in the forward direction for a velocity scatterer. Finally, $\dot{S}(t-t_1-t_2)$ is the derivative of the source time function of the source, shifted in time by t_1+t_2. t_1 is the travel time (computed from the smoothly varying velocity model) between x_s and x , and t_2 the travel time between x and the receiver x_g. θ is the angle between the two rays at the scattering point.

Equation (1.13) provides a simple way of computing the scattered wavefield for a smoothly varying background. It is used intensively in Chapter 3 as the basis for an iterative inversion method . The inversion method involves computing the forward problem. This is done in practice in the following way, for seismic reflection geometries :

1 - Given the smoothly varying background velocity, a set of travel times is computed for rays joining the origin point (0,0) to all points in an array (x, y).

2 - The ray parameters p are computed at each of the point of the array.

3 - From the knowledge of the ray parameter variations, the geometrical spreading factor is obtained.

Figure 1.6 displays the travel times, the sine of the angle of the ray with the vertical, the cosine of the same angle , and the geometrical spreading factor for the

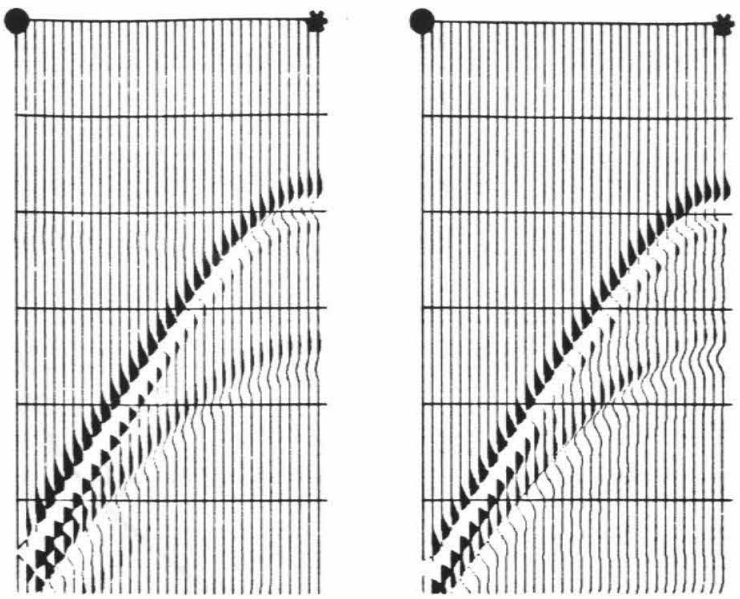

Finite Difference Born Approximation

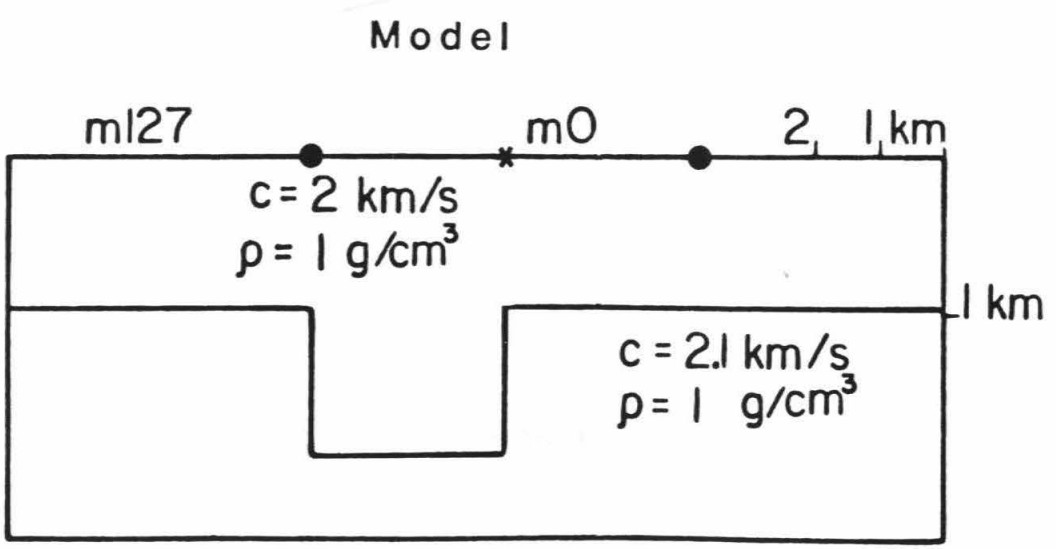

Figure 1.3 - Comparison of synthetic seismograms computed using the Born and far-field approximation and a finite difference method. The section to the right is the approximate calculation. The sections are midpoint gathers computed for the model shown in the lower part of the figure. The position of the midpoint is indicated by a star, the positions of the source and receiver by a dot for the largest offset.

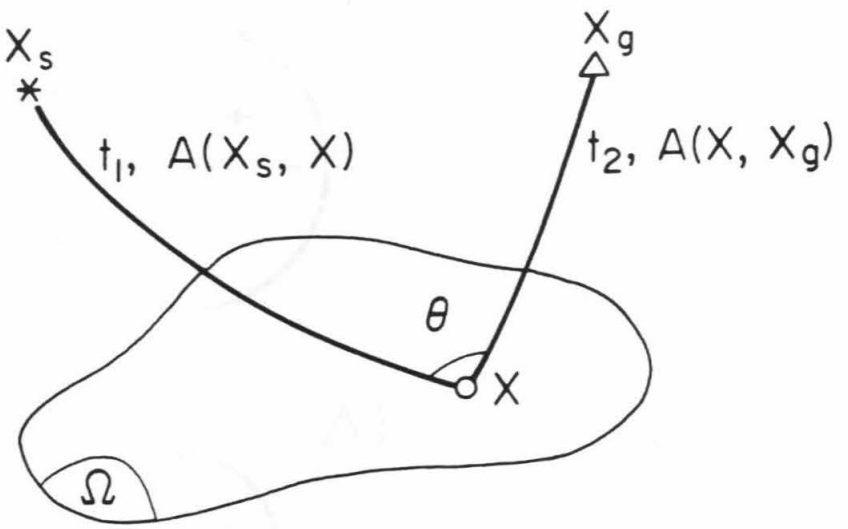

Figure 1.4 - Illustration of the far-field Born approximation geometry.

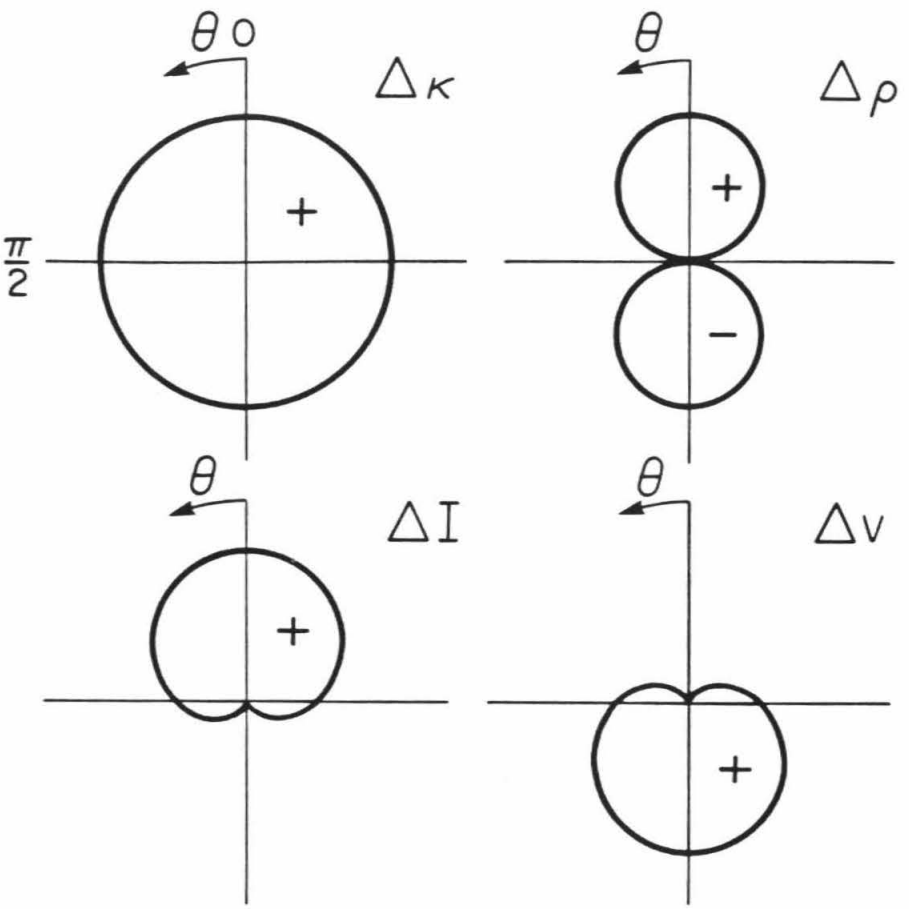

Figure 1.5 - The scattering coefficients as a function of the angle θ between incident and scattered rays for a bulk modulus κ, density ρ, impedance I and velocity v inhomogeneity.

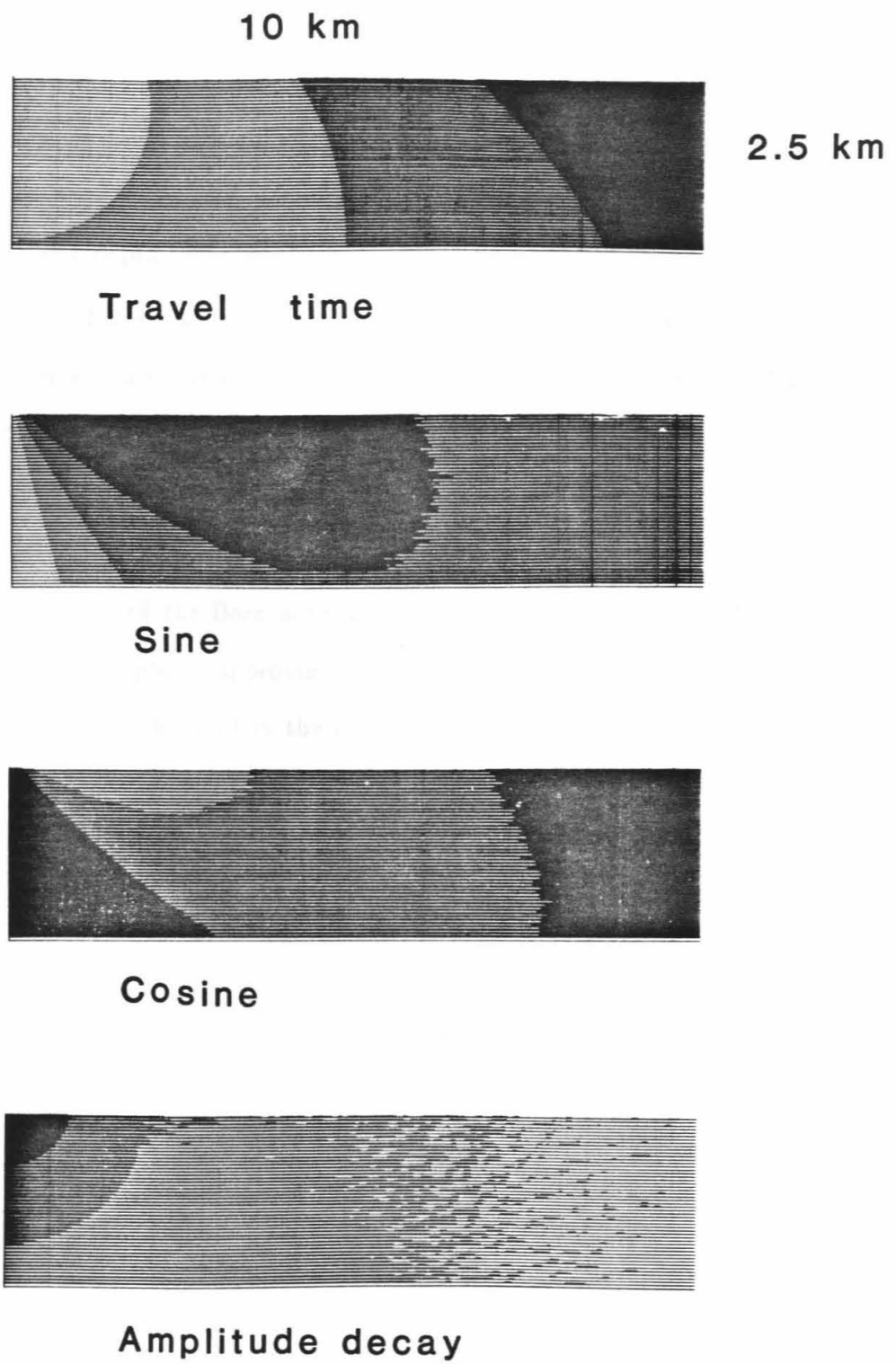

Figure 1.6 - Functions representing the travel-time, sine of the ray, cosine of the ray and geometrical spreading factor as a function of depth and distance along strike for a linear velocity increase with depth.

ray joining the origin to the (x,y) point. From the knowledge of these functions, the expression for the scattered wavefield can be computed using Equation (1.13). These examples were computed for a laterally homogeneous model presenting a linear increase with depth : $v(z) = 2.5 + 0.343z$.

Figure 1.3 shows a comparison of synthetic seismograms computed using a finite-difference method and the Born and far-field approximations. The background medium in this case was constant, with a velocity of 2km/s and a density of $1 g/cm^3$.

Conclusion

We presented the Born approximation to a scattered wavefield and developed a further ray-asymptotic approximation on the propagation Green's functions. These developments will be used in the following chapters to devise inversion methods and test them on synthetic and actual data.

Chapter 2

Tests of a Frequency-Wavenumber Born Inversion Algorithm on Exact Synthetic Data

Abstract

From the expression of the Born approximation in the frequency-wavenumber domain, a simple two parameters inversion algorithm is devised. The algorithm is tested for one-dimensional media on synthetic seismograms generated using a Cagniard-de Hoop method, and for two-dimensional media on synthetic finite-difference seismograms. Profiles of density and bulk-modulus are recovered within the frequency bandpass of the source time function used to generate the synthetics. The limit in offset is shown to influence the ability of the algorithm to resolve between the two acoustic parameters. When the data are too limited in offset, a good reconstruction of the impedance is still obtainable.

Introduction

In the first chapter, an expression for the scattered wavefield under the Born approximation was given in the frequency- offset wavenumber and midpoint wavenumber domain. That expression can be used as the basis for an inversion algorithm of the scattered wavefield for the acoustic parameters of the underlying

medium as has been proposed by Clayton and Stolt (1981). The scattered wavefield was expressed as a linear combination with known coefficients of the bulk-modulus and density as functions of the depth wavenumber and midpoint wavenumber:

$$D(k_m, k_h, \omega) = \frac{-\rho_0}{4}\left[A\,1(k_m, k_z, k_h)\; a_1(k_m, k_z) + A\,2(k_m, k_z, k_h)\; a_2(k_m, k_z)\right] S(\omega).$$

Clearly, the functions a_1 and a_2 can be estimated over each point in k_m, k_z by doing a simple least-squares fitting over the k_h.

The algorithm proposed by Clayton and Stolt (1981) to obtain the variations a_1 and a_2 can be summarized in the following simple procedures :

(1) - Three dimensional Fourier transform of the midpoint gather of the data over time, midpoint and offset.

(2) - Deconvolution of the source-time function.

(3) - Transformation of the wavefield into the k_m, k_h, k_z space.

(4) - Inversion for $a_1(k_m, k_z)$ and $a_2(k_m, k_z)$.

(5) - Inverse Fourier transform to get $a_1(m, z)$ and $a_2(m, z)$.

In this chapter, several examples of application of the above method are presented. Both one dimensionally varying media and two dimensionally varying media are considered. The data were generated using synthetic techniques which take into account loss of energy at interfaces, multiple reflections, refractions and other phenomena not included in the first Born approximation. It is therefore a good test of the validity of the proposed method to be applied to actual data.

The essential advantage of implementing this inversion technique is the rapidity with which Fourier transforms are performed on computers. The first step of the

procedure involves a three-dimensional Fourier transform. The dimension of the cube of data sets the speed of execution for this part of the processing, which is the most time-consuming. If the spectrum of the source time function is band limited, the storage space for the cube of data in the wavenumber-frequency space can be greatly reduced by keeping only the information contained into that bandwidth.

Transforming the field into the depth wavenumber domain involves an interpolation to be done on the data set. This is also true for the F-K migration method. It is a delicate step. To avoid introducing artifacts due to the interpolation, the time traces lengths should be long enough. The functions in the frequency domain will then be smoothed to allow interpolation.

The plane interface case

The method of inversion was tested on very simple models consisting of two interfaces and a line source . The Green's functions for the waves reflected off the medium were computed using the exact Cagniard-de Hoop method. Only the primary reflection rays were included in the synthetically generated data. The amplitudes of the multiply reflected rays are of much smaller amplitude for the models considered.

The reflected waves were computed for 128 offset distances. A source time function consisting of a sine wave over the length of its period (0.16 seconds) was convolved with the Green's functions. The record section thus obtained (e.g., Figure 2.2) is then Fourier transformed over time and offset. The source function introduced into

the data is deconvolved over a limited bandwidth. This limits the amount of information to be recovered from the data in the wavenumber space. The function obtained then depends on frequency and offset wavenumber. Using the relation $k_h^2+k_z^2=4\frac{\omega^2}{c_1^2}$ which is the wavenumber-frequency form of the wave equation for a uniform velocity medium, the wavefield is then expressed as a function of depth and offset wavenumbers. This last step corresponds to an F-K migration (Stolt, 1978). The function thus obtained is identifiable to the left-hand side of Equation A.2 in Appendix A. It is then possible to invert Equation A.2 for $\frac{\Delta\kappa}{\kappa}$ and $\frac{\Delta\rho}{\rho}$ as a function of k_z. An inverse Fourier transform then gives these two parameters as a function of depth.

Synthetic seismograms for the models listed in Table 2.1 have been computed and inverted using the method described above.

Table 2.1

	Model 1 (Figure 2.1)		Model 2 (Figure 2.2)		Model 3 (Figure 2.3)	
	velocity km/s	density g/cm^3	velocity km/s	density g/cm^3	velocity km/s	density g/cm^3
Layer 1	4.0	1.0	4.0	1.0	4.0	1.0
Layer 2	4.0	1.05	4.1	1.0	4.1	1.0
Half-space	4.1	1.05	4.1	1.05	4.1	0.95

The seismograms and the results of the inversions are shown on Figures 2.1 to 2.3 .

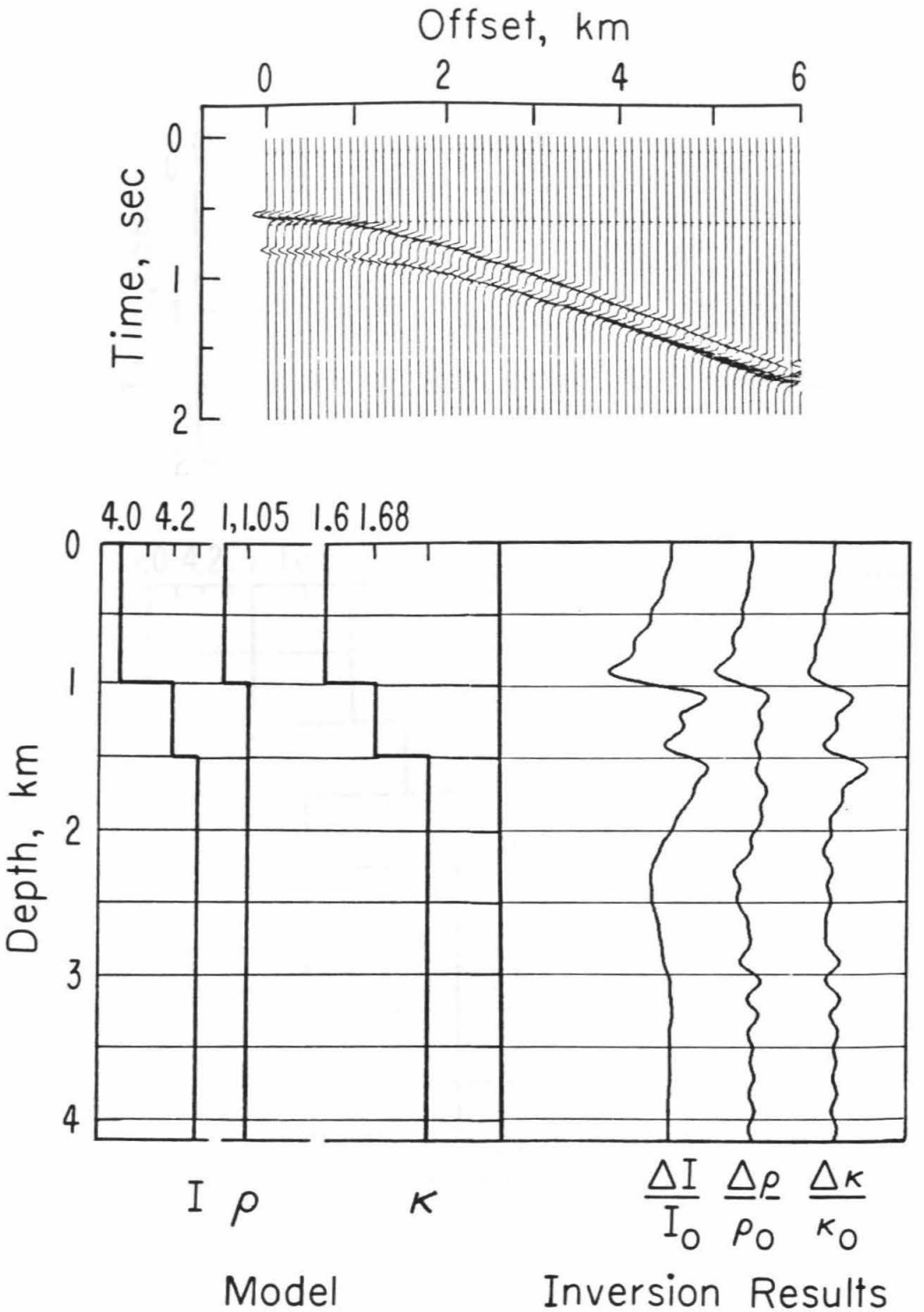

Figure 2.1 - Top of figure : synthetic section computed for the model to the lower left. The result of the F-K domain Born inversion method is shown to the lower right. ρ is density, κ bulk modulus, and I impedance. (Model 1, Table 2-1).

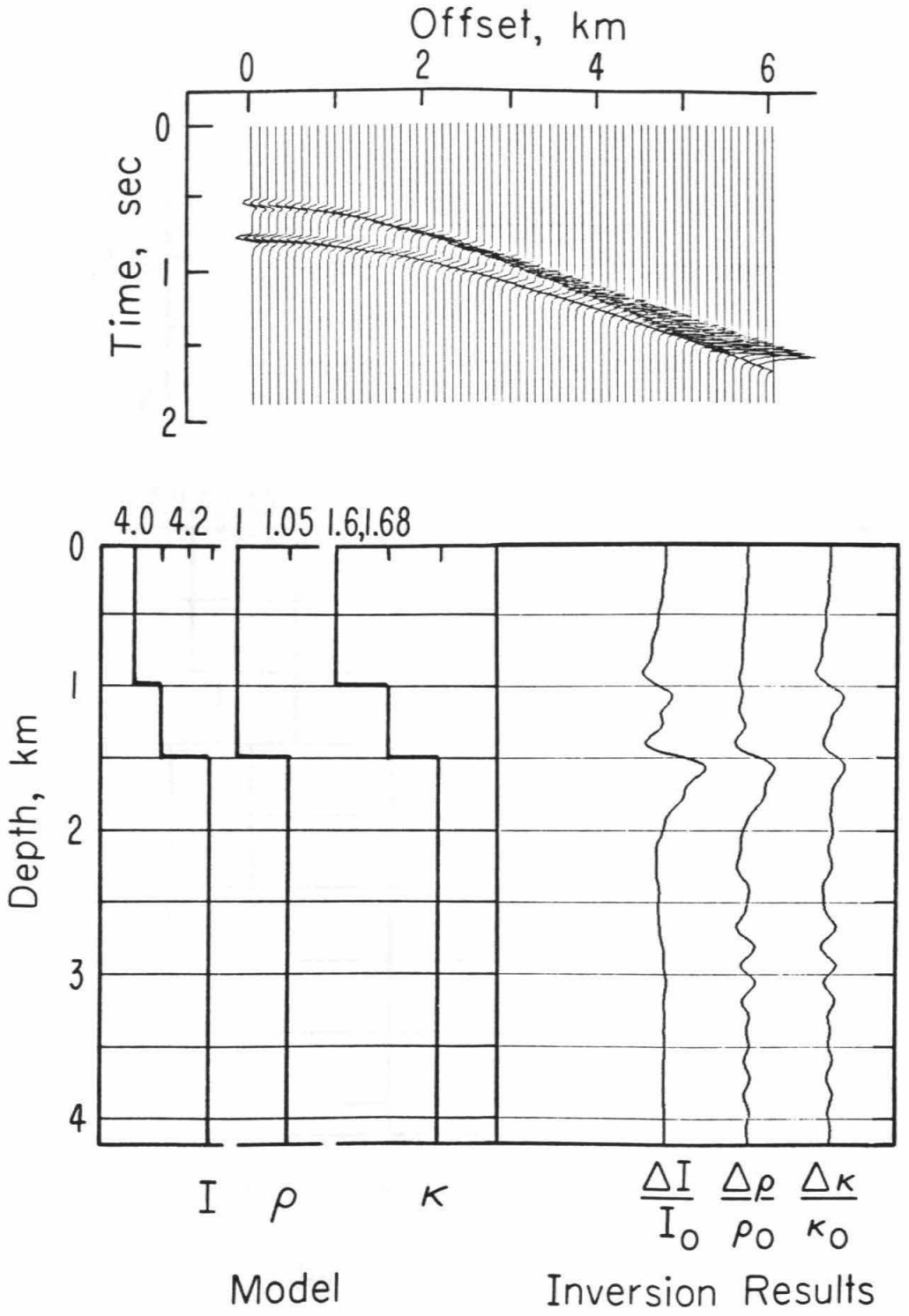

Figure 2.2 - Same as Figure 2.1 for Model 2, Table 2-1.

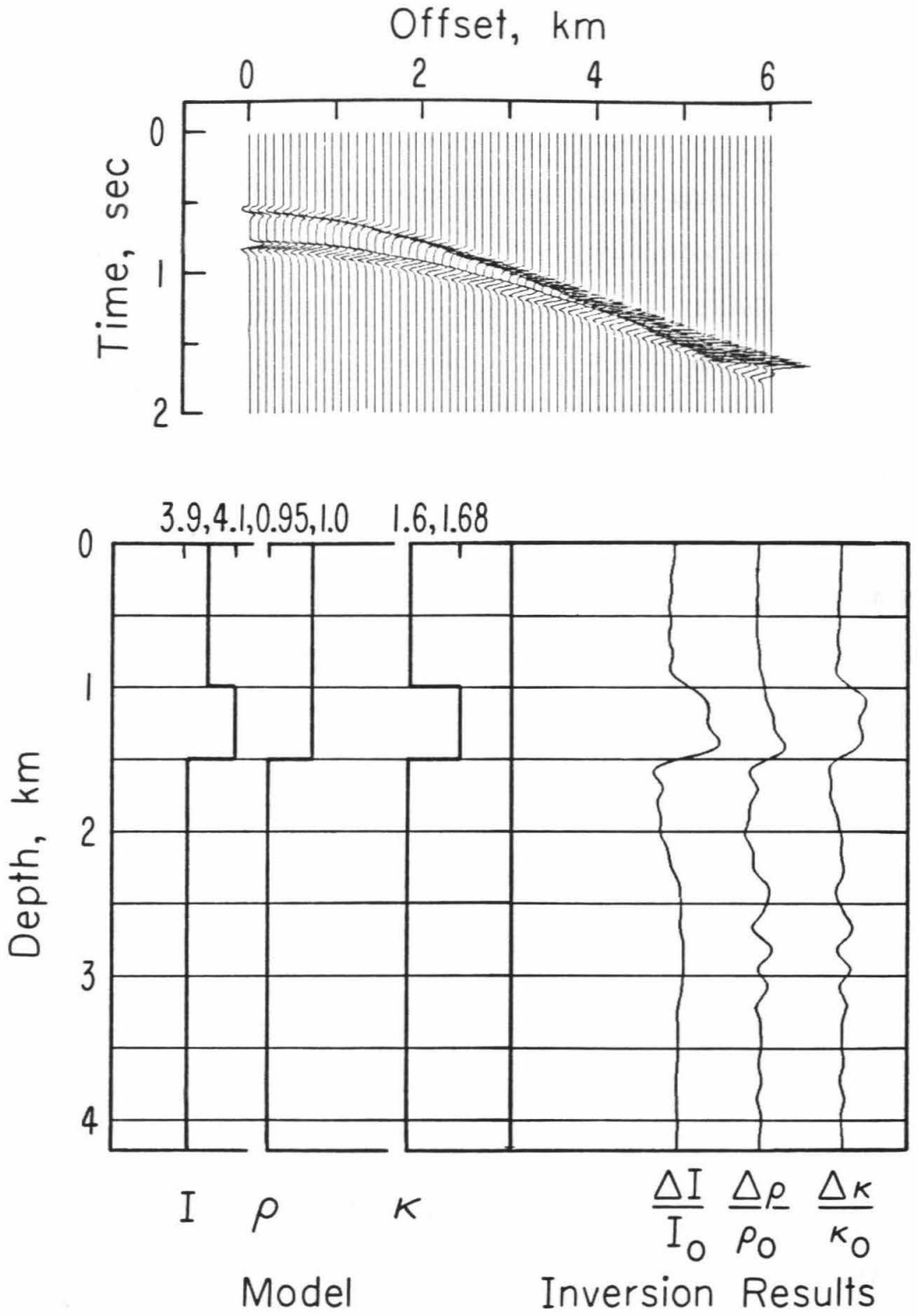

Figure 2.3 - Same as Figure 2.1 for Model 3, Table 2-1.

The source function convolved in the seismograms is limited in frequency so that the variations of the parameters with depth can be resolved only in a certain bandwidth. This limits the depth resolution of the method. In the case of these sharp interface synthetic models, the effect is to make the discontinuity appear as a broad smooth signal. The zero-frequency part is not resolvable by the method, due to the nature of the source. It might be possible to try to reconstruct it using some signal processing methods. For instance, after deconvolving the source, the spectrum could be extended towards the high frequencies using a Burg's algorithm technique as proposed by Oldenburg et al. (1983). This would improve the sharpness of the variation of density and velocity with depth, giving a better space resolution.

Spurious signals are observed at a depth dependent on the maximum offset(between 2.5 and 3 kms in our cases).Their peculiarities are that they are present on both traces (relative bulk modulus and density variations) at the same depth. The artifact on the reconstructed density function is a mirror image of the one on the bulk modulus section. On the impedance function, which is the sum of the density and bulk modulus traces, the artifact disappears. We can show that it is related to the offset cutoff of the data since changing the largest offset modifies the depth and character of the artifact. There is however apparently no very simple relation between the largest offset used and the depth at which the artifact appears.

The impedance profile is well reconstructed. The artifact mentioned in the previous paragraph is absent from the impedance trace. This is expected, as most of the information contained into the near-normal incidence angles pertains to the impedance contrast. This can be appreciated from Figure 1.5 which shows the amplitude of a scattered wave as a function of the angle between incident and scattered

wave for different values of the scatterer. For an angle of zero (normal incidence back-scattering) the impedance contrast dominates.

Each of the Figures 2.1 to 2.3 presents the synthetic seismograms section on the top, computed from the model shown at the lower left. The result of the inversion is shown at the lower right of the figures. The model and the inversion results show the variations of the bulk modulus, the density and the impedance. Different impedance contrasts have been tested. On Figure 2.1, the shallower interface has no density contrast. This is quite well reconstructed on the inversion. The model shown on Figure 2.2 has a second interface with no density contrast and both interfaces have a bulk modulus increase through them. Figure 2.3 shows an example with a decrease of the density at the second interface. The sign of the inverted trace is well reconstructed. For all these examples, the synthetic seismograms were computed exactly, including refraction and loss of amplitude at the transmission through the first interface. The theory used to invert the sections does not take these phenomena into account. In these simple cases with small variations, its usefulness is demonstrated since the two independent variables are reconstructed and the relative amplitude of the two discontinuities as well as their depth is correctly estimated within the bandpass of the source time function.

The depth of the second interface, however, is slightly underestimated due to the discrepancy between the background velocity (4 km/s) and the velocity of the second layer. This problem is expected to be minimal when the background velocity is known within a few percent. In Chapter 3, we will investigate further the problems associated with the use of a wrong background velocity model.

Limitation of the method with depth

To assess the extend of validity of the method with depth, several sections were computed using a single reflecting interface at different depths. The interface was placed at depths varying from 1 km to 4 km. The accuracy of the inversion breaks down with increasing depth. For an interface at 1 or 2 kms, the variables are correctly reconstructed. However, for larger depth, there is a tendency for the inversion to place the energy into the density trace and it breaks down for depths larger than 3 kms. This is simply explained by the progressive decrease with depth of the aperture angle on the scatterers. Figure 2.4 illustrates this reduction of the resolution between two variables as a function of depth.

Laterally varying models

In the case of laterally homogeneous media there is no advantage in using a wavenumber-frequency method. In the case of a one dimensionally varying medium, simply using the amplitude information in the time-offset section would provide us with the same information on the reflection coefficients and thus on the physical characteristics of the scatterers. The implementation of such a method is very straightforward since it does not involve any transformation of the data into frequency and wavenumber spaces. Furthermore, the same guidelines as for a semblance analysis can be used. The amplitudes of the waves along the optimum hyperbola could be inverted directly for density and bulk modulus. If the medium has lateral variations, however, the wavefield can be expressed in a simple way as a function of the two wavenumbers involved (midpoint and offset wavenumber) as shown by Clayton and Stolt (1981).

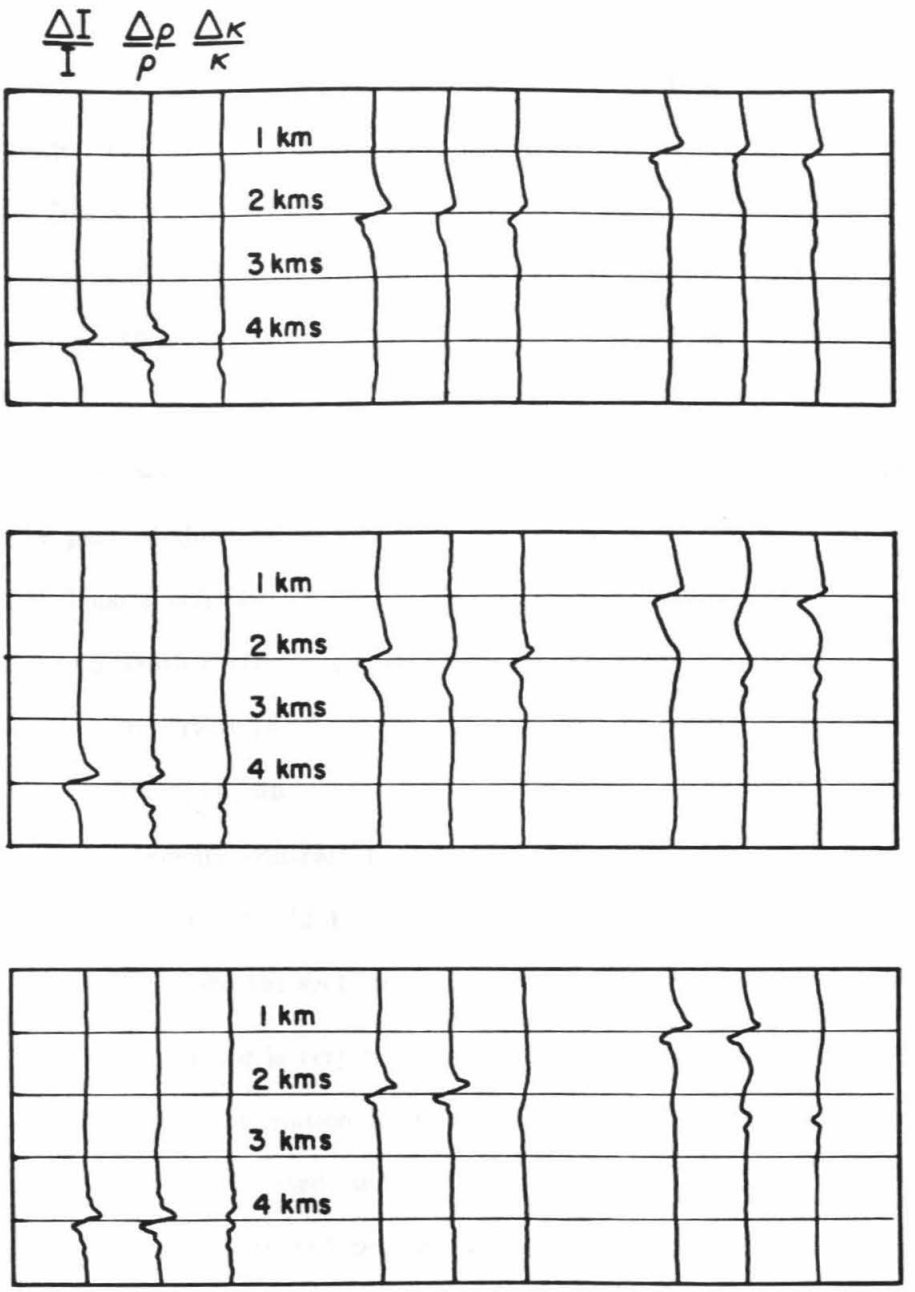

Figure 2.4 - Test of the inversion algorithm for three different depths of the reflector. The three panels from top to bottom are for different characteristics of the reflectors, and the depth of the reflector varies from right to left.

In order to test the method, we computed synthetic data using a finite difference code for two simple models. 192 shot gathers were computed, 128 of which have a full offset coverage from 0 to 6 kms. The direct arrivals are removed from the sections. There is no free surface at the source-receiver level. All four boundaries of the box containing the model have absorbing boundary conditions. A source-time function (sine wave over 0.16 s. period) is convolved with the result of the finite-difference calculations.

Figure 2.5 shows the first model used and the result of the inversion. The model on the lower part of the figure consists in a step-like boundary between two media presenting a density contrast of 5% . After processing using the method described above , the two depth sections at the top of the figure were obtained. The two sections represent respectively the bulk modulus and density relative variations between the midpoints marked m_0 and m_{127}. They are plotted at the same absolute scale. Since there is no velocity contrast between the two media the relative density and bulk modulus variations should be equal across the boundary and the two figures should be identical. Indeed the sections are similar.

The shallower reflector is very well reconstructed in position and amplitude. The amplitude of the relative variation in density is about the same as the one in bulk modulus, which is to be expected, and the signals are in phase. The arc-shaped signal to the left of both reconstructed sections at the same depth as the interface is an artifact of the F-K migration method used.

The deeper reflector is correctly located by the reconstruction; however, the phase is not correct and seems about opposite on the two sections for this reflector. This is probably due to an artifact of the same nature as the one mentioned for one-

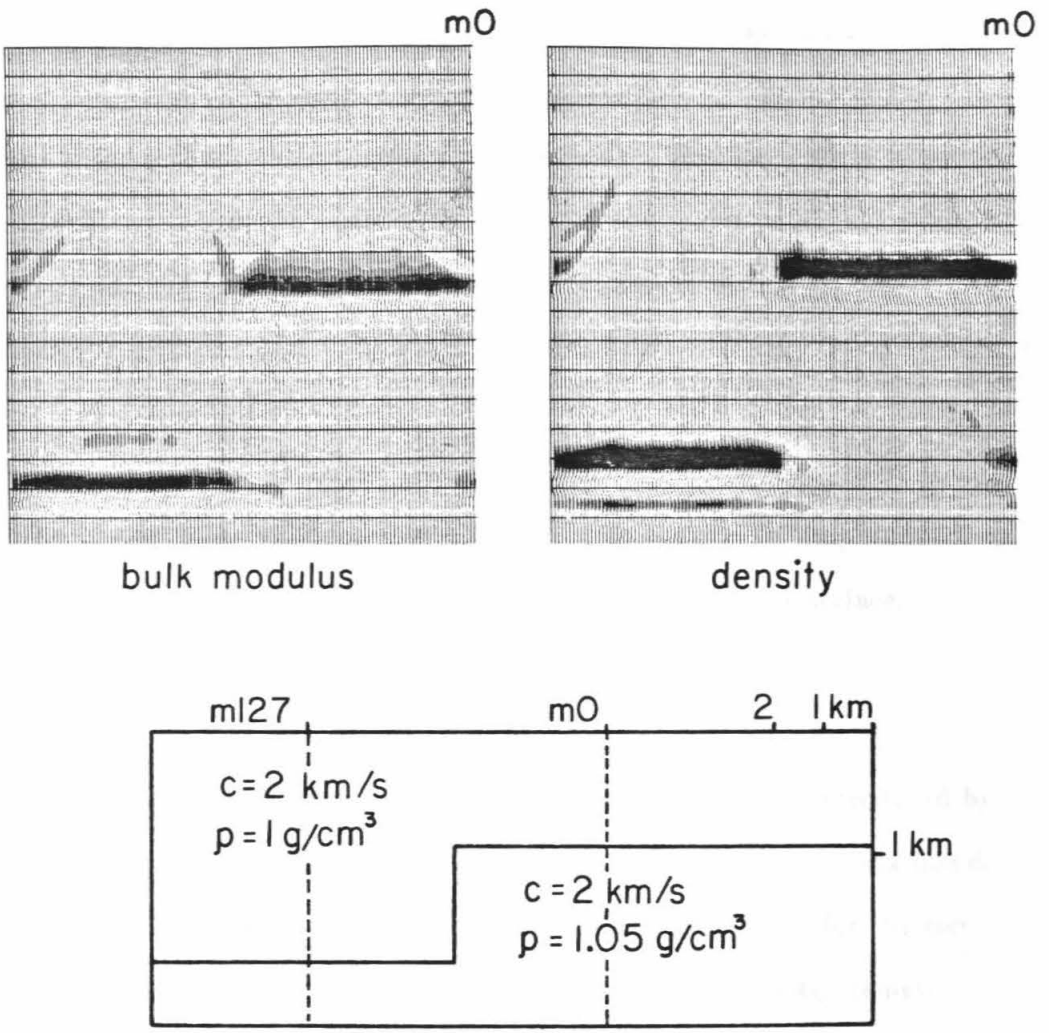

Figure 2.5 - The bottom of the figure shows a model used to compute finite difference synthetic seismograms. There is no velocity variation across the interface for this model. The top of the figure presents the results of the inversion method for the two parameters: density and bulk modulus.

dimensional media.

Note that the sections are reconstructed only within a limited bandpass due to the convolution by the source time function. Hence, low and high frequencies of the actual variations of the density and bulk modulus are lost in the process. Figure 2.6 presents the second model with lateral variations. This time, there is no contrast in density between the two media. The result of the inversion should show the structure only on the bulk modulus section and the density section should be blank. This is nearly true for the first shallower interface which hardly appears on the density section. The deeper interface (bottom of the "ditch") is not as well reconstructed as was the case in the previous model. The interface is correctly located, however the density section shows some residual energy at its depth and the amplitude of the bulk modulus is not as well reconstructed as it is on the shallower interface.

Conclusion

We tested the frequency-wavenumber inversion technique introduced by Clayton and Stolt (1981) on exact synthetic seismogram sections, both varying one dimensionally and two dimensionally. The results were quite encouraging for the reconstruction of the impedance profiles in one dimension. However, the multiparameter inversion is more problematic. It necessitates a large angle coverage of the subsurface to be able to retrieve the two parameters independently, and we observe an artifact probably related to the cutoff in offset in the data.

For two-dimensional models, the technique was tried on two simple models, one with a density contrast, the other with a velocity contrast. The technique proved to be effective in differentiating between these two types of contrasts; however, the

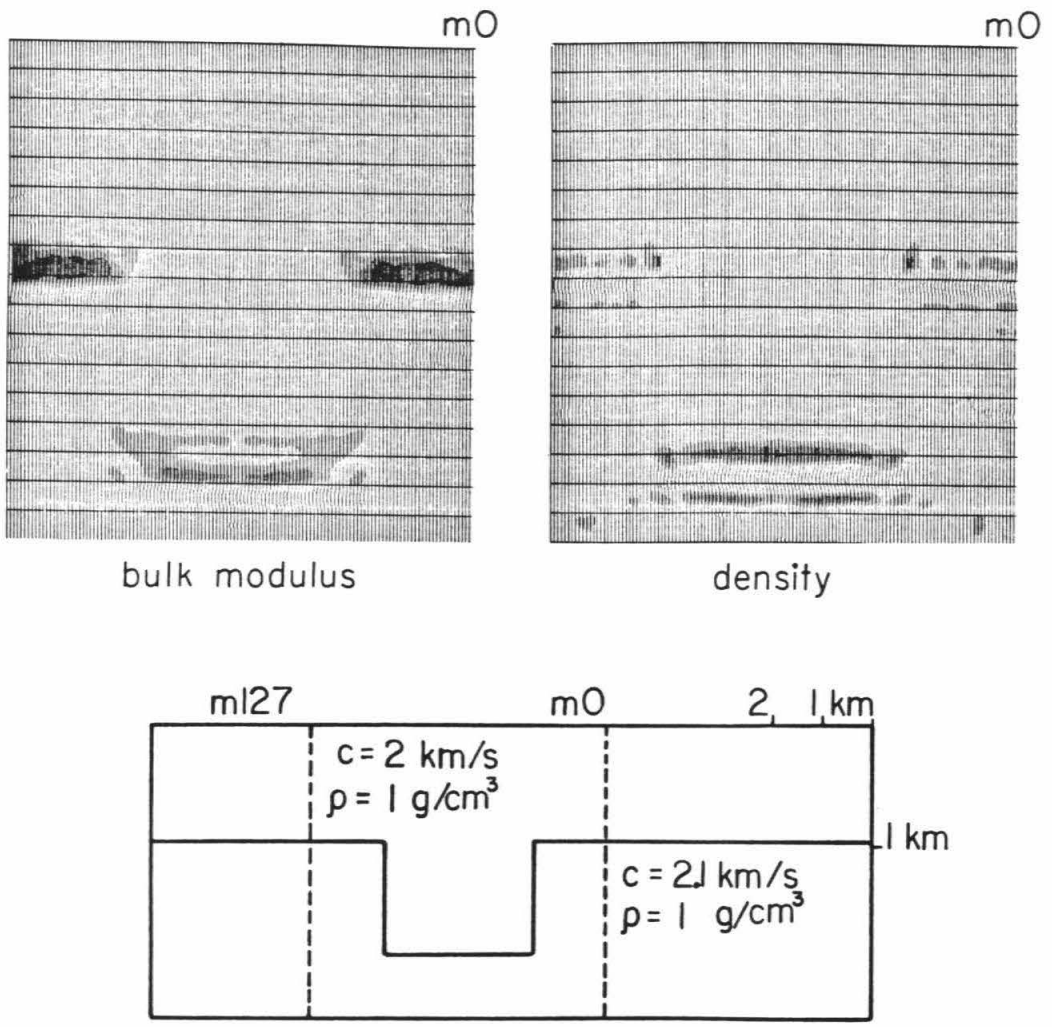

Figure 2.6 - Same as Figure 2.5 for no contrast in density between the two media.

reconstructions presented unexplained phase shifts, and in both cases the lower interfaces were not satisfactorily recovered.

Chapter 3

A Tomographic Inversion of the Acoustic Back-scattered Wavefield

Abstract

The application of the Born approximation on the scattered wavefield followed by a WKBJ and far-field approximation on the propagation Green's function for a slowly varying background medium leads to a simple integral relation between the density and bulk-modulus anomalies superimposed on the background medium and the scattered wavefield. We develop an iterative inversion scheme based on successive backprojections to reconstruct the two acoustic parameters. The scheme is applied on data generated using the direct integral relation and shows that the variations of the parameters can be reconstructed using such a scheme. The procedure is readily applicable to actual data, since every iterative step is essentially a before-stack Kirchhoff migration followed by the application of the direct Born and far-field operator.

Introduction

In the previous chapters, the theory of the Born approximation has been developed. In essence, we related the physical parameters defining the medium : density and bulk modulus to the seismic reflection data. Under the approximation, the relationship between the parameters and the data becomes linear, unlike in the full

theory. The linear inverse theory can then be applied to the problem. However, the large dimensions of the matrices involved in the application of the inverse theory in the case of seismic data is an incentive to try to derive different algorithms, that do not imply the inversion of a very large matrix. A typical problem in seismic reflection is the imaging of a region having dimensions of a few kilometers to a few tens of kilometers in length and a few hundred meters to a few kilometers in depth, depending on the specific aim of the survey. In order to apply the inverse theory, the medium has to be discretized. The smallest period present in the seismograms will determine the discretization step in space, if we want to take full advantage of the data. Usually this gives a discretization step of 20 to 50 meters, and this gives us a dimension of at least 10^4. The dimension of the data space is even larger. If we consider a survey, or a portion of a survey consisting of 100 shots recorded on 24 receivers for a duration of 4 seconds and a discretization of 0.004 seconds, the dimension of the data space is $2.4\ 10^6$. Clearly, with such large dimensions for both model and data spaces, a classical least squares method is impractical.

These considerations lead to using other techniques to search for the solution that is optimum in some sense. A similar problem of large dimensions of data and model space was encountered by workers in geophysical tomography. The general problem in that field consists in estimating a velocity model from the knowledge of travel time residuals of seismic waves through the model, assuming a known travel path. (This last approximation can be likened to our assumption of knowing the background velocity.) Geophysical tomography has been applied to different data sets, including the whole Earth (Clayton and Comer, 1985), the regional crustal and Moho structures of Southern California (Hearn, 1985), the structure of the Mantle under

Southern California (Humphreys et al., 1984) and a local structure in France (Nercessian et al., 1984; Tarantola and Nercessian, 1984). Closer to our application, Tarantola (1984a, 1984b) has introduced the concept of tomography for whole wavefield inversion of seismic data. All these authors use an iterative process based on backprojection to approximate the inverse. The backprojection operation consists in applying the transposed operator, or a modified version of it to the residuals, or data. The result is added to the previous model estimation to obtain an update of that estimation. From the current model, the next set of residuals is calculated, and another iteration can be performed if desired. The iterative process allows large size problems to be handled by relatively small size computers, since they can be treated sequentially, without requiring a very large memory space corresponding to large matrices. Furthermore, no matrix inversion is necessary, with its inherent instabilities.

One drawback for all the methods cited above is that the resolution and variance of the models obtained are difficult to estimate other than empirically, for example, by doing synthetic tests to estimate point spread functions. In the next paragraph, we will introduce several methods of optimization of a function, in this case the quadratic function L_2-norm of the residuals, and will show how to apply algorithms which have been developed in the field of optimization (Fletcher, 1980) to our specific problem.

Optimization of the L_2-norm of the residuals

Let us introduce the notations used throughout this chapter. We defined earlier a Born operator as a linear operator on a model space whose vector is the space-variable function $c = \left[\frac{\Delta\rho(x)}{\rho}, \frac{\Delta\kappa(x)}{\kappa}\right]$, respectively, the relative density and bulk

modulus variations. The operator applied on the model gives the Born approximation wavefield. The direct Born operator is noted G. The objective we pursue is to minimize the L_2-norm of the residual vector defined as $u - Gc$ where c is the model vector and u the data vector. The L_2-norm is a quadratic function of the vector c, and it can be optimized by techniques such as descent methods and quasi-Newton methods among others (e.g., Rao 1977; Fletcher, 1980).

The descent methods establish a line of search for a minimizing point along the direction of the gradient of a function, in our case the L_2-norm of the residuals. This makes sense intuitively, because we know that the function is going to be smaller along the gradient than at the starting point in its neighborhood if the starting point is not a stationary point. The gradient needs to be easily obtainable for these methods to be applied. For our problem, the gradient is the expression : $-G^T(u - Gc)$. To calculate it, it is necessary to compute the forward Born problem at the point where we estimate the gradient and then compute the transposed Born problem over the residual. The algorithm for the search of a minimum is then the following :

- Choose an initial model c_0, usually 0.

Subsequently, for the k^{th} iteration:

- Compute the quantity $s_{k+1} = \alpha_k G^T(u - Gc_k)$. where α_k is a scalar computed to optimize the L_2-norm along the line defined by the gradient.

- Add s_{k+1} to the previous model c_k.

Descent methods present disadvantages. They may have a slow rate of convergence and may converge asymptotically. Newton's method is a second-order method

and requires the knowledge of the Hessian of the function to minimize. The increment s_k in this case is not simply proportional to the gradient, but to the gradient transformed by the inverse of the Hessian. In the case of a quadratic function, as here, Newton's method is the classical least-square method. I already discarded it because of the large dimensions involved. Quasi-Newton methods require only the knowledge of the first derivatives, which are easily computed in our case by backprojection of the residuals. The inverse of the Hessian is approximated by a positive definite matrix which is updated at each iteration. This presents the advantage that there is no matrix inversion since we try to estimate the inverse of the Hessian directly.

One such quasi-Newton method is the Davidon-Fletcher-Powell (DFP) method (Fletcher, 1980; Rao, 1977), that is presented in more detail in the next paragraph.

The Davidon-Fletcher-Powell method

Quasi-Newton methods can be viewed as modifications of descent methods. Using the same notations as were introduced in the last paragraph, the k^{th} iteration of a quasi-Newton method can be defined as follows:

- set $s_k = -H_k g_k$ where $g_k = G^T (u - Gc_k)$ and H_k is a positive definite matrix, defined in the next paragraph.

- update H_k, giving H_{k+1}.

- add $\delta_k = \alpha_k s_k$ to the previous model c_k. α_k is a scalar computed so as to minimize the L_2-norm along the line defined by s_{k+1}.

The matrix H_k is definite positive. In the case of the DFP method, it is updated at each iteration following the relation :

$$H_{k+1}=H_k + \frac{\delta_k \delta_k^T}{\delta_k^T \gamma_k} - \frac{(H_k \gamma_k)(H_k \gamma_k)^T}{\gamma_k^T H_k \gamma_k}$$

where $\gamma_k = g_{k+1} - g_k$ is the difference between the gradients at two consecutive iteration points.

The initial H_0 can be taken, for instance, as the identity matrix or as the diagonal matrix whose elements are the inverse of the diagonal elements of $G^T G$.

From the form of the equation updating the H matrix, we can see that we need only store vectors of model-space dimension (two per iteration) to have a complete representation of H.

The DFP method has important properties, especially when it is used to minimize quadratic functions, which is the case in our problem. For these, it terminates in, at most, m iterations where m is the size of the model space. Furthermore, and most important for our purpose, H approximates the inverse of the Hessian matrix at the point of convergence. In our case, the Hessian matrix is $G^T G$. This provides a convenient way of estimating the variance matrix at the convergence point using the relation :

$$<\Delta c \, \Delta c^T> = \sigma^2 (G^T G)^{-1},$$

where we have supposed that the variance matrix of the data is represented by the identity matrix times σ^2.

The size of the problem involved in seismic reflection applications will not make very many iterations possible, as the dimension of the model space can be very large.

With respect to this difficulty, it is important that the method of optimization has a rapid initial convergence rate, with rapid decrease in the rms for the first few iterations.

Application of the Davidon-Fletcher-Powell to inversion of seismic data

In Chapter 1, we derived the expression for a scattered field in a two-dimensional medium under the Born Approximation and a far-field approximation:

$$D(x_s, x_g, t) = G\,\mathbf{a}(x, y), \tag{3.1}$$

where :

$$\mathbf{a}(x, y) = \begin{bmatrix} a_1(x, y) \\ a_2(x, y) \end{bmatrix}.$$

In an explicit form :

$$D(x_s, x_g, t) = \int_\Omega d\Omega A(x_s, x)\, A(x, x_g) \left[a_1(x) + a_2(x)\cos\theta \right] \dot{S}(t - t_1 - t_2). \tag{3.2}$$

The notations are the same as in Chapter 1. This equation defines the forward Born far-field problem. The scattered wavefield is computed from a knowledge of the distribution of density and bulk modulus. To apply our optimization method, we need to define the corresponding transposed operator. To do so, we need a scalar product over our model and data spaces. This is conventionally done by using the following definition for the scalar product of two vectors **u** and **v** :

$$<\mathbf{u},\mathbf{v}> = \int_\Omega d\Omega\ \mathbf{uv}.$$

The transposed operator of G is then fully defined by :

$$<\mathbf{u}, G\mathbf{v}> = <G^T\mathbf{u}, \mathbf{v}>,$$

where $\mathbf{v}$ belongs to the model space and $\mathbf{u}$ to the data space.

Using this definition of G, and of the scalar product :

$$\int dx_s \int dx_g \int dt \; D(x_s, x_g, t) \int_\Omega d\Omega A(x_s, x) \, A(x, x_g) \left[a_1 + a_2 \cos\theta \right] \dot{S}(t - t_1 - t_2)$$

$$= <D, G\mathbf{a}>.$$

The order of integrations can be rearranged and :

$$\int_\Omega d\Omega \int dx_s \int dx_g \int A(x_s, x) \, A(x, x_g) \left[a_1 + a_2 \cos\theta \right] \dot{S}(t - t_1 - t_2) D(x_s, x_g, t)$$

$$= <G^T D, \mathbf{a}>.$$

Hence, the transposed operator acting on the data set $u(x_s, x_g, t)$ is defined by :

$$\hat{a}_1 = \int dx_s \int dx_g \int dt \; A(x_s, s) A(x, x_g) \dot{S}(t - t_1 - t_2) \, D(x_s, x_g, t). \tag{3.3}$$

$$\hat{a}_2 = \int dx_s \int dx_g \int dt \; A(x_s, s) A(x, x_g) \dot{S}(t - t_1 - t_2) \cos\theta \, D(x_s, x_g, t).$$

In practice, the procedure followed to obtain the transposed data is to crosscorrelate the derivative of the source function with the seismograms with a delay time corresponding to the travel time between source, current point and receiver. The crosscorrelation is then added to the array representing the parameter at the current point of the model space and multiplied by the appropriate coefficient, namely, the amplitude factor of geometrical spreading and the angular factor $\cos\theta$ for a_2. Hence, this procedure is very similar to a before-stack Kirchhoff migration (Jain and Wren, 1980). In fact, the only difference is that we multiply the crosscorrelation with a different coefficient and that the process is iterated on after computing the direct problem and the residuals.

Application to synthetic data

The method given above was tested on synthetically generated data. In the first step, the data were generated using a direct Born formulation. This allows us to concentrate on the performance of the inversion algorithm itself.

The models used for generating the synthetics are very simple. They consist of an array of 30 by 20 cells. Each cell is 0.05 km square. The top of the imaged area (e.g., Figure 3.1) is at a depth of 0.2 km. The data were generated using a sampling interval of 0.004 seconds. The background velocity represents a linear increase with depth $v(z) = 2.5 + 0.343z$. Synthetic seismograms are computed at 16 midpoints and 24 offsets for each midpoint. The midpoints were placed at an interval of two cells (0.1 km) and the increment between successive offsets is 4 cell sizes (0.2 km). This gives us a maximum offset of 4.6 km. The first midpoint is directly above the top left corner of the area to be imaged. The source function used for the examples presented in Figures 3.1 to 3.8 is one cycle of a sine function.

Point scatterers

Synthetics were generated for point scatterers simulated by placing a cell with an anomaly either in density or in bulk modulus at the center of the area to be imaged. In both cases, the amplitude of the anomaly is a relative increase of 0.01 of the variable at the point scatterer. Figures 3.1 to 3.4 show the results of the first and third iterations for synthetic data generated from a density point scatterer. The intensity scale at the bottom was chosen so that the maximum amplitudes on the sections are slightly saturated. The first set of Figures (3.1 and 3.2) shows the direct

output of the inversion program. The two following Figures (3.3 and 3.4) are a smoothed version of them. The sections were smoothed by averaging over a disk with a radius of 2 cells (0.1 km). Figures 3.5 to 3.8 are for a bulk modulus point scatterer and also present the direct results of the first iteration and third iteration backprojections (Figures 3.5 and 3.6) along with smoothed versions (Figures 3.7 and 3.8).

These two examples illustrate some of the characteristics of this kind of inversion. Its artifacts are similar to the artifacts of a Kirchhoff migration, as can be expected. This is best illustrated by the figures showing the first iteration of the inversion for the two different models. There is a streaking of the anomalies in the horizontal direction, which can be thought of as the effect of superimposing the equal travel time arcs. They do not interfere destructively due to the absence of arcs crossing vertically. This is very much improved with successive iterations.

Another feature of this iterative method is the buildup of the amplitude of the anomalies with successive iterations. This is illustrated by the difference in the amplitude scales on the figures between the first and third iteration, reflecting the difference in the maximum amplitudes on the sections. This amplitude buildup is like the one observed by workers in tomographic inversion of travel time data. Several problems were examined relative to this inversion method and are presented below.

To illustrate the ability of such an inversion technique to be useful in differentiating between different rheologies, we computed synthetics generated for a model with four point scatterers. Each of the points has different characteristics. The model is presented in Figure 3.9. Two sets of reconstructions have been made for this model, first, with a maximum offset of 2.3 km and then with a maximum of 4.6 km.

Modulus

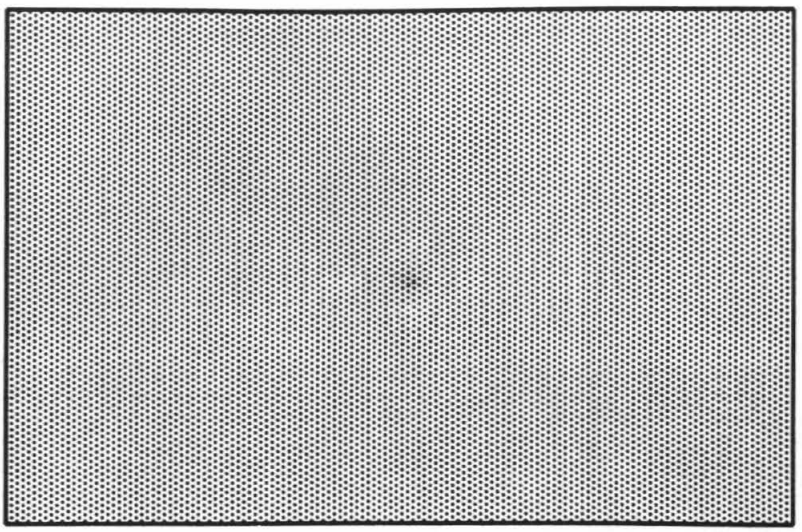

Density

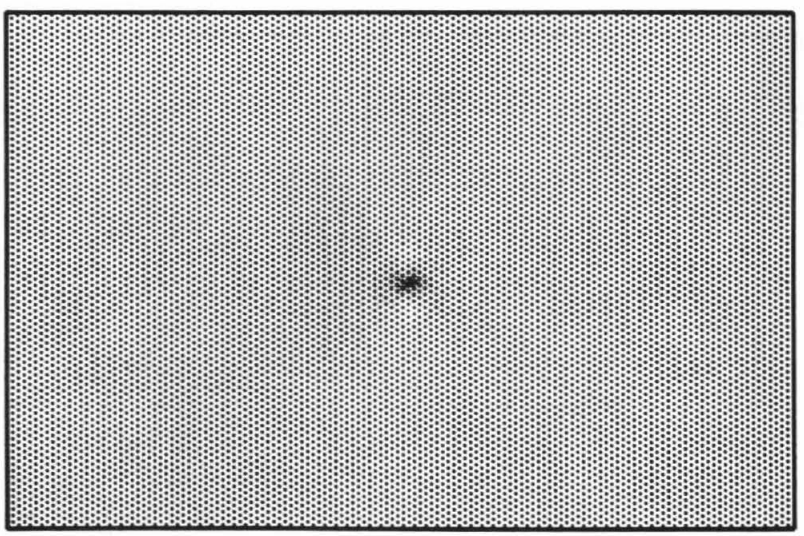

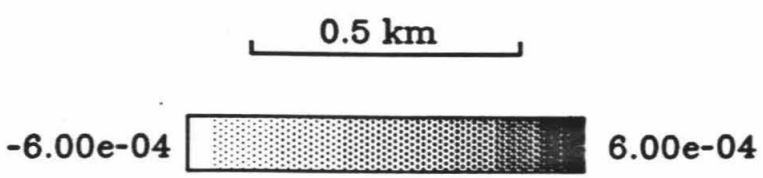

Figure 3.1 - First iteration. Density point scatterer.

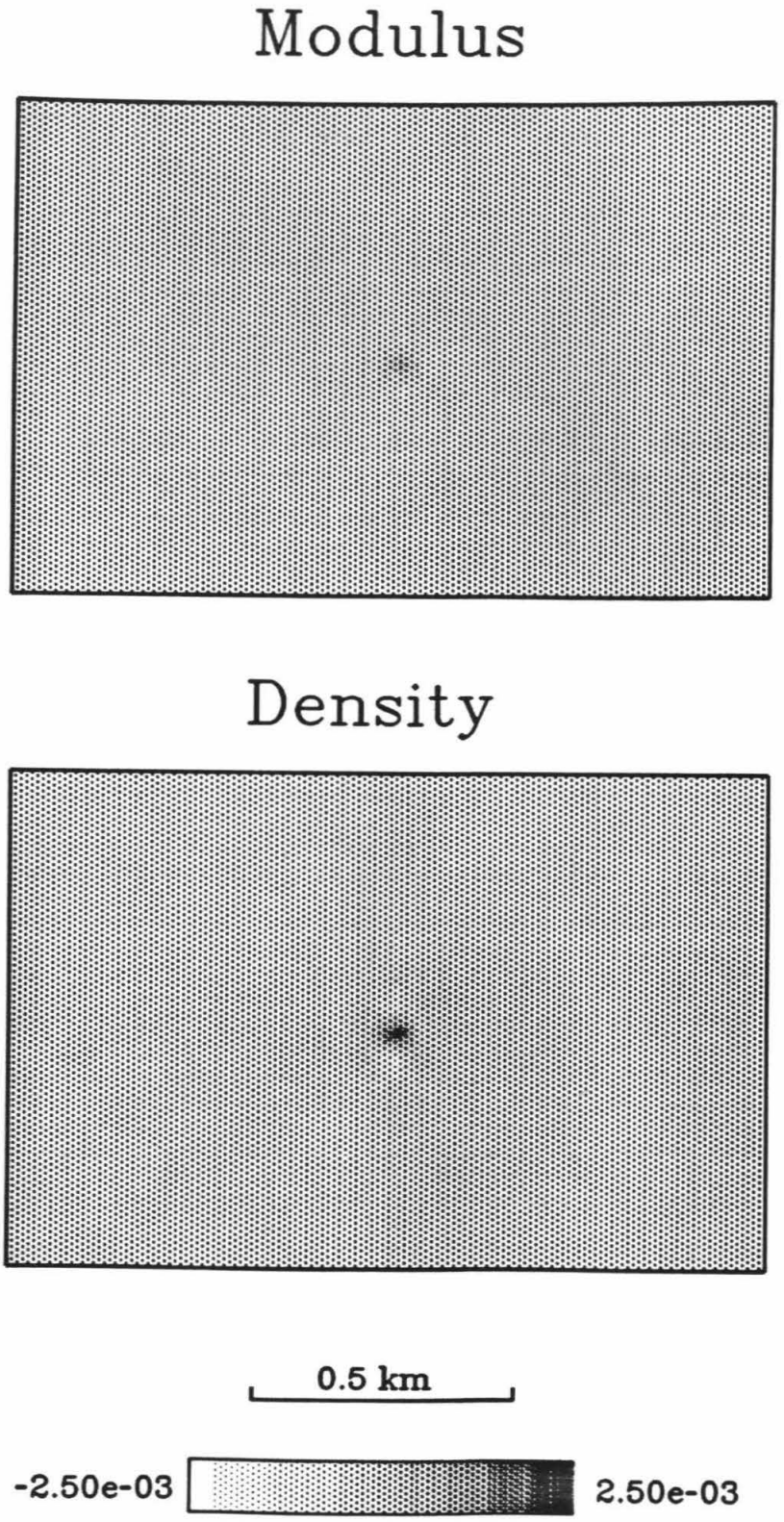

Figure 3.2 - Third iteration. Density point scatterer.

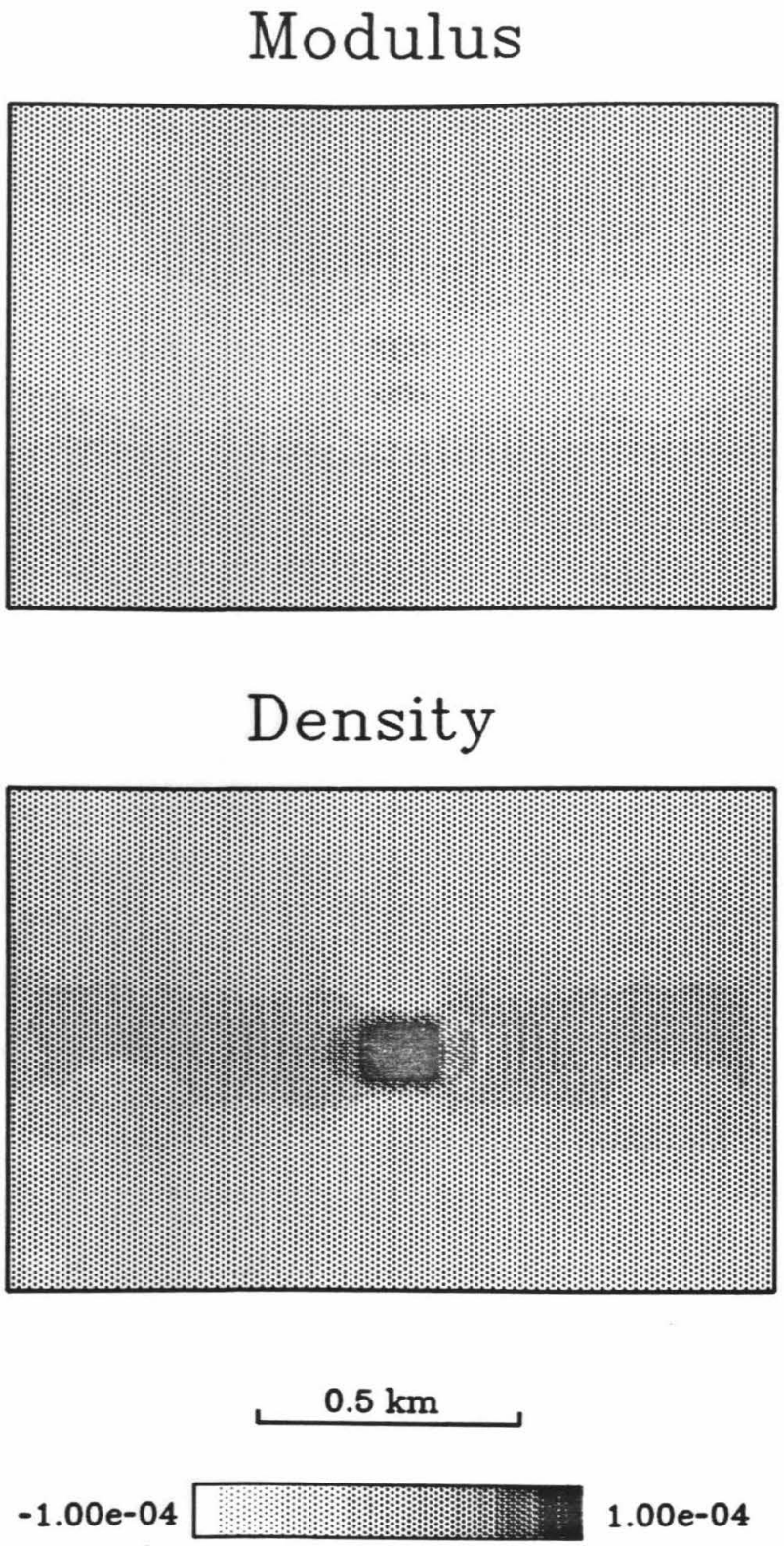

Figure 3.3 - First iteration. Density point scatterer. Smoothed over a disk of radius 2 cells.

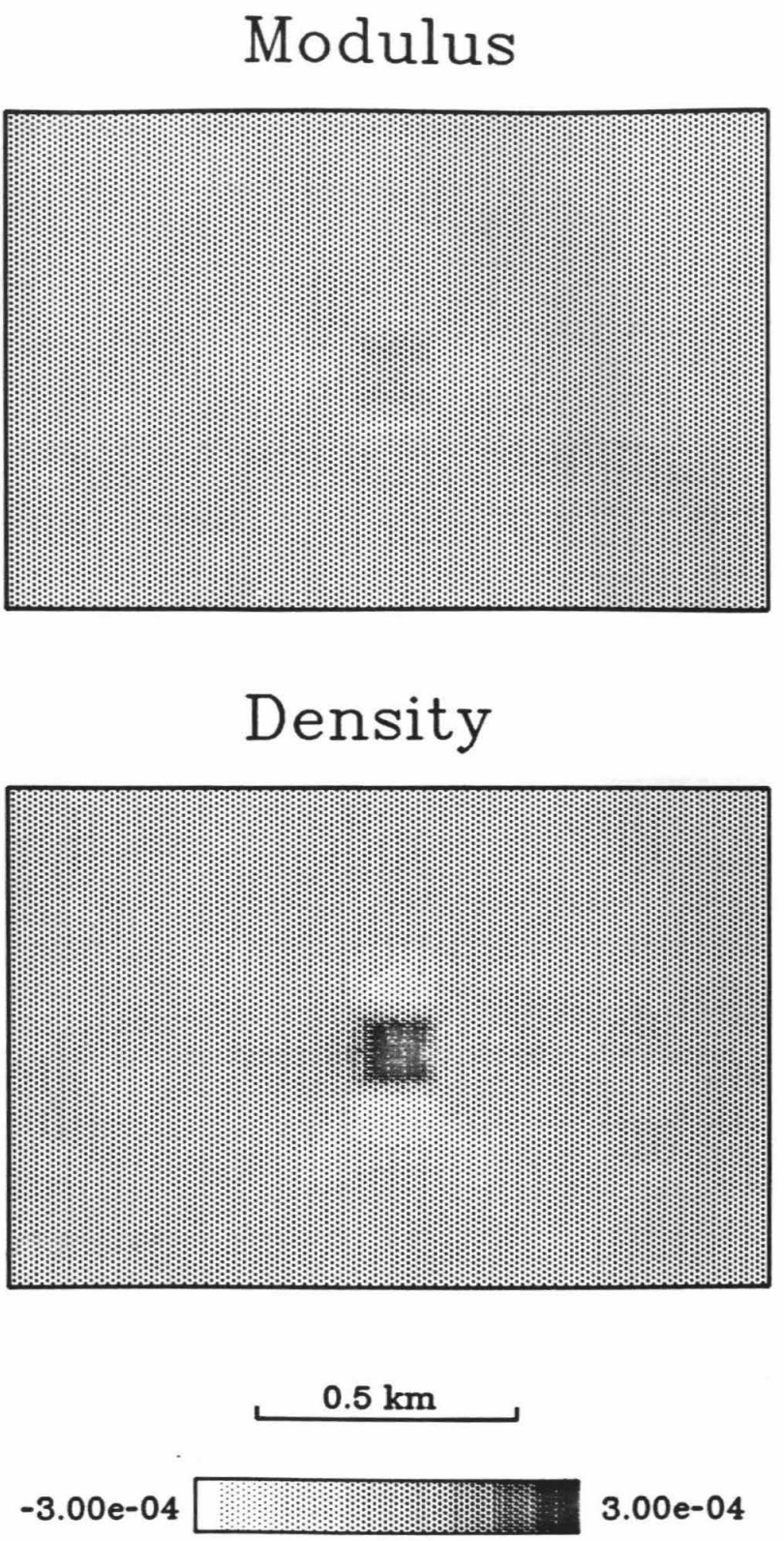

Figure 3.4 - Third iteration. Density point scatterer. Smoothed over a disk of radius 2 cells.

Modulus

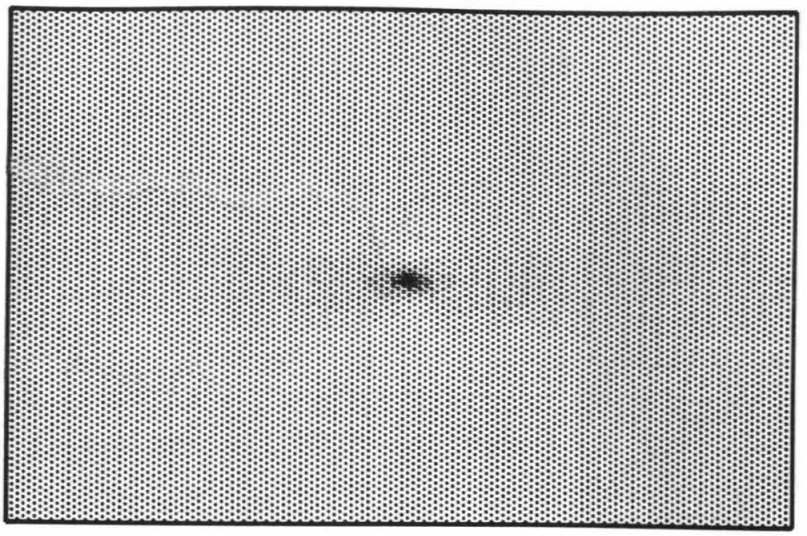

Density

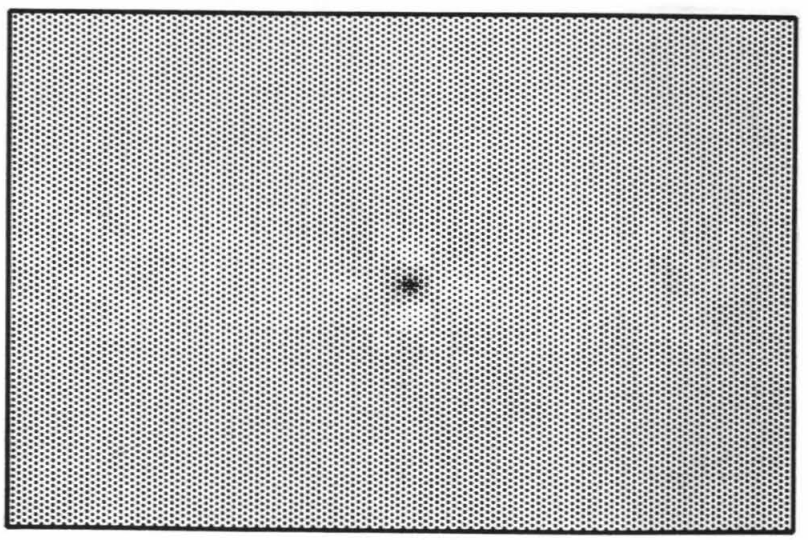

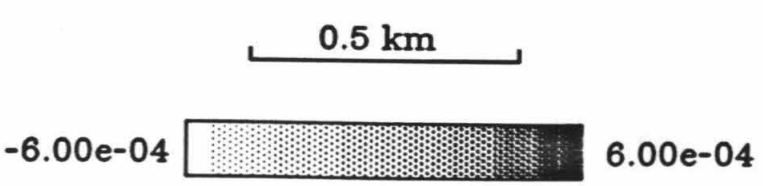

Figure 3.5 - First iteration. Modulus point scatterer.

Modulus

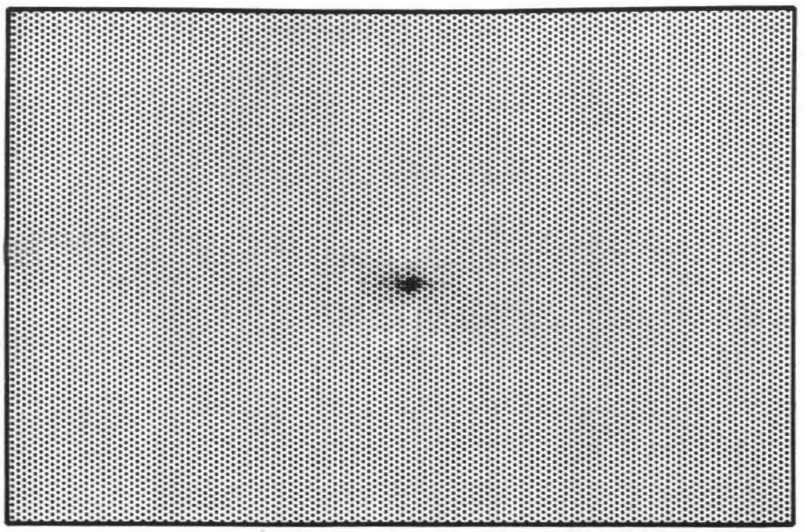

Density

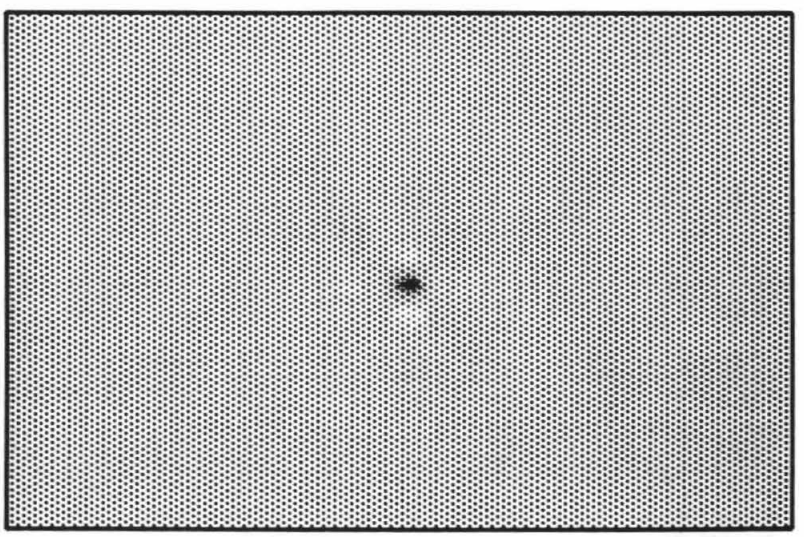

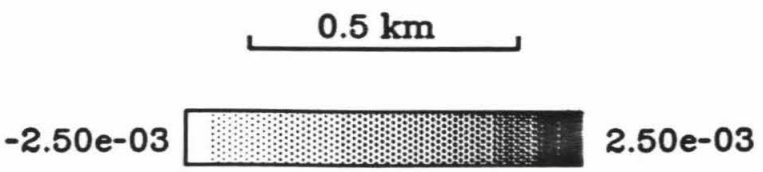

Figure 3.6 - Third iteration. Modulus point scatterer.

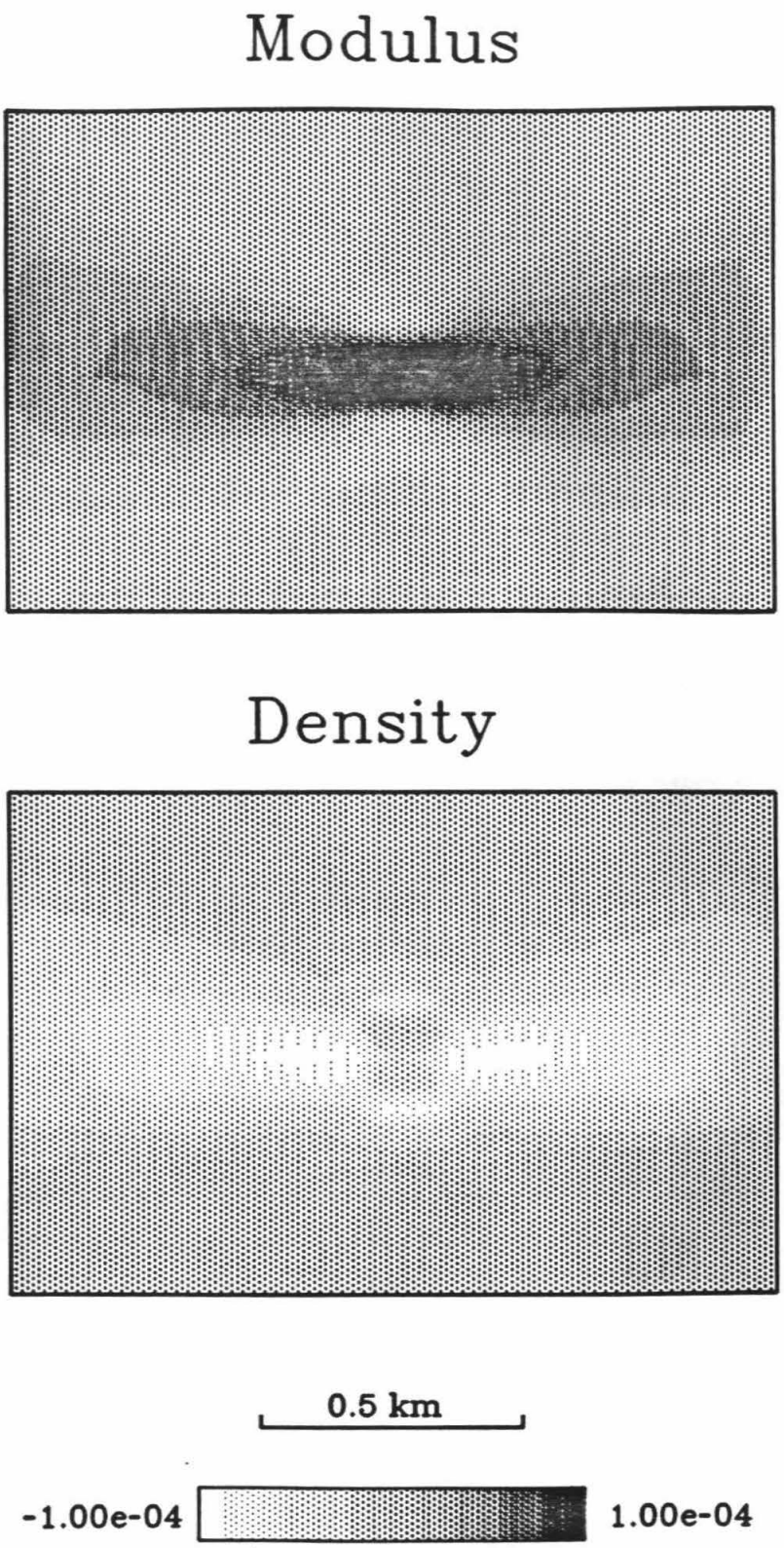

Figure 3.7 - First iteration. Modulus point scatterer. Smoothed over a disk of radius 2 cells.

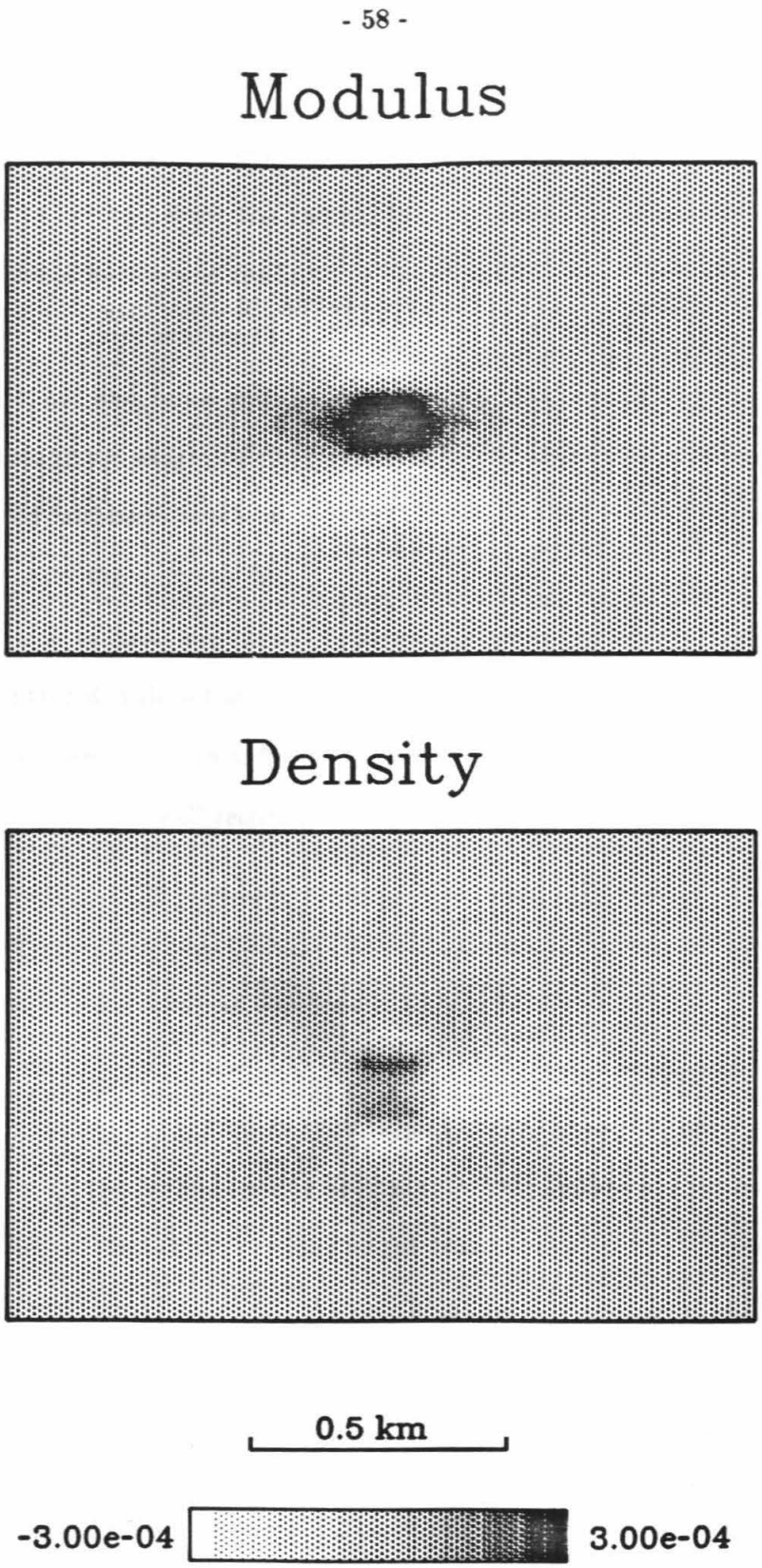

Figure 3.8 - Third iteration. Modulus point scatterer. Smoothed over a disk of radius 2 cells.

Figures 3.10 to 3.13 show the reconstructions for the small maximum offset of 2.3 km, and Figures 3.14 to 3.17 show the reconstructions for a maximum offset of 4.6 km. The bulk modulus model was made up of three scatterers with equal weights. The density section has three scatterers with weights of 0.01, 0.02 and -0.01. Note that in both cases of small and large maximum offsets the anomalies are well reconstructed with their appropriate weighting except for the lower right corner anomaly which is poorly recovered, although better so on the large offset experiment (Figure 3.17). This is explainable since the anomaly has no impedance contrast with the background and therefore will not radiate any direct backscattered energy. The surface data, being mostly backscattered, will not see it, unless the offset coverage becomes such that the scattered waves will be forwardly scattered, at least in part. In all cases, the impedance anomalies are well reconstructed.

Noise analysis

An empirical noise analysis was conducted by adding white noise to a signal generated with a density point scatterer model. The results are very encouraging. The effect of adding white noise even in very large amounts does not affect the backprojected images very much. This is due to the ability of the method to cancel random noise by adding it destructively along equal travel time paths. Figure 3.18 shows representative midpoint gathers for the one point density scatterer, with signal over noise ratios of ∞, 10 and 0.05. Figure 3.19 is the direct result of the first iteration for the signal-over-noise ratio of 10 and Figure 3.20 the result of the third iteration. Filtered versions of these figures are given, respectively, in Figure 3.21 and 3.22. These can be compared to Figures 3.1 to 3.5 which are the noiseless reconstructions. Figures

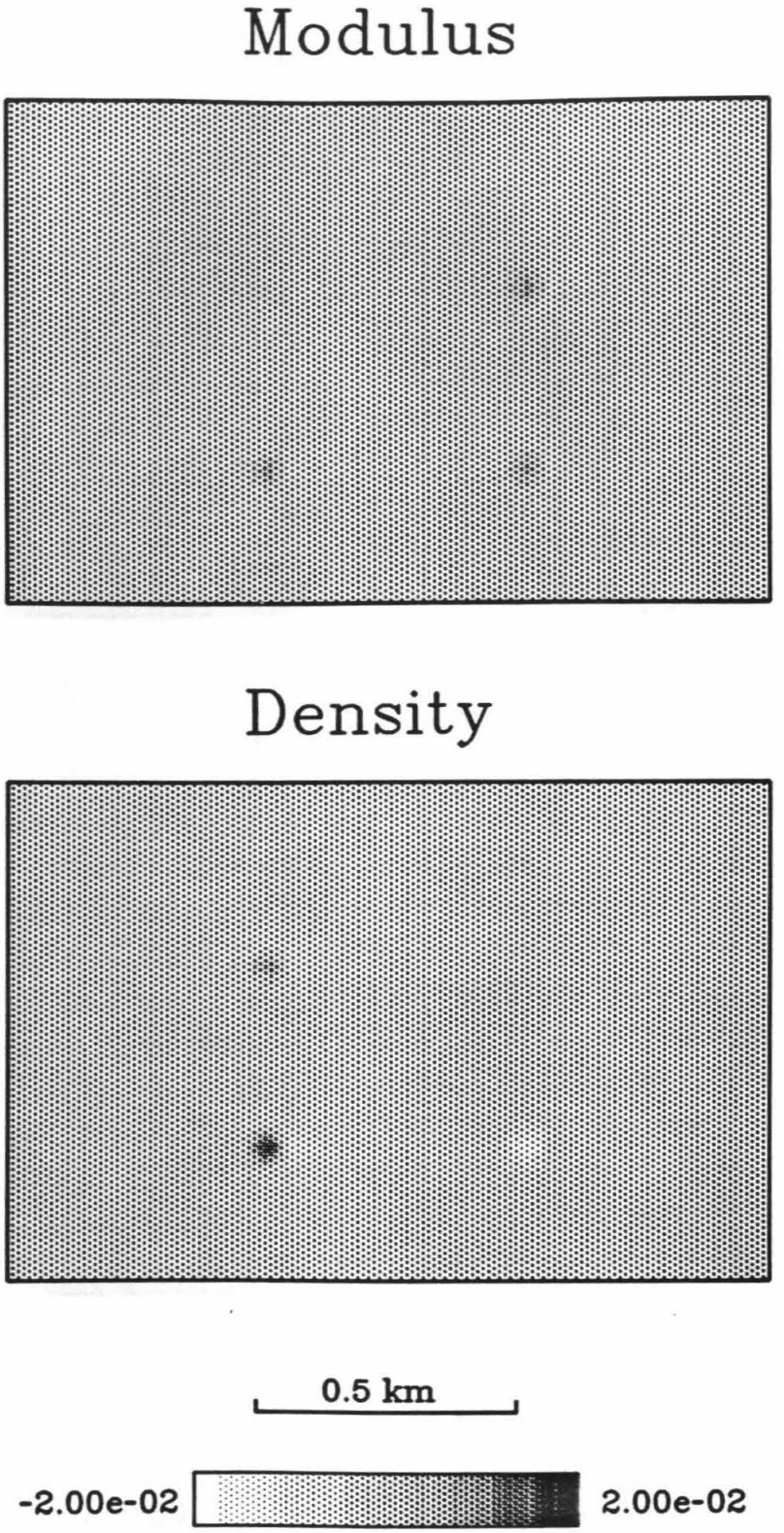

Figure 3.9 - Model for the four points scatterer model. Each of the scatterers has different characteristics.

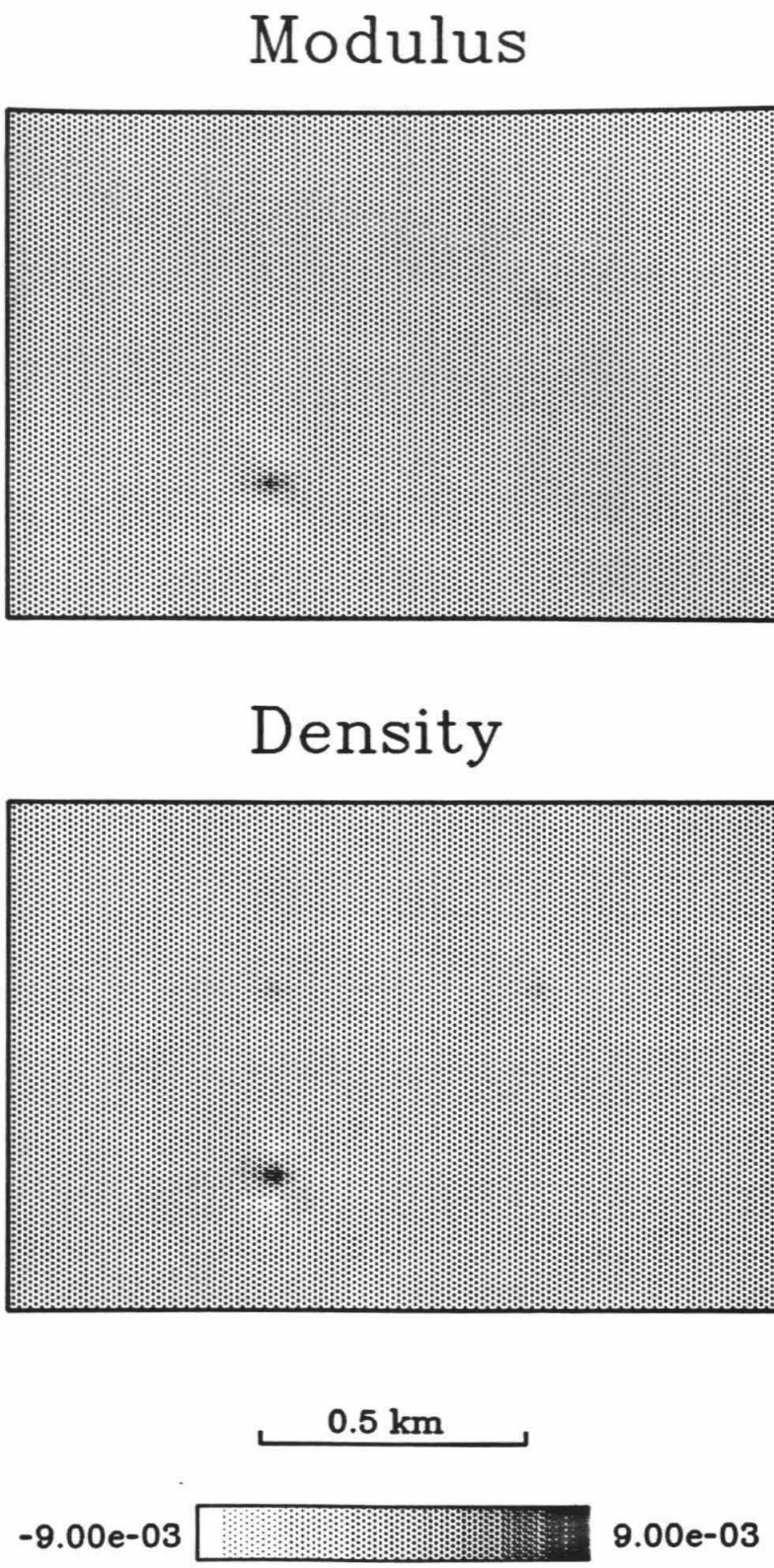

Figure 3.10 - First iteration for a maximum offset of 2.3 km.

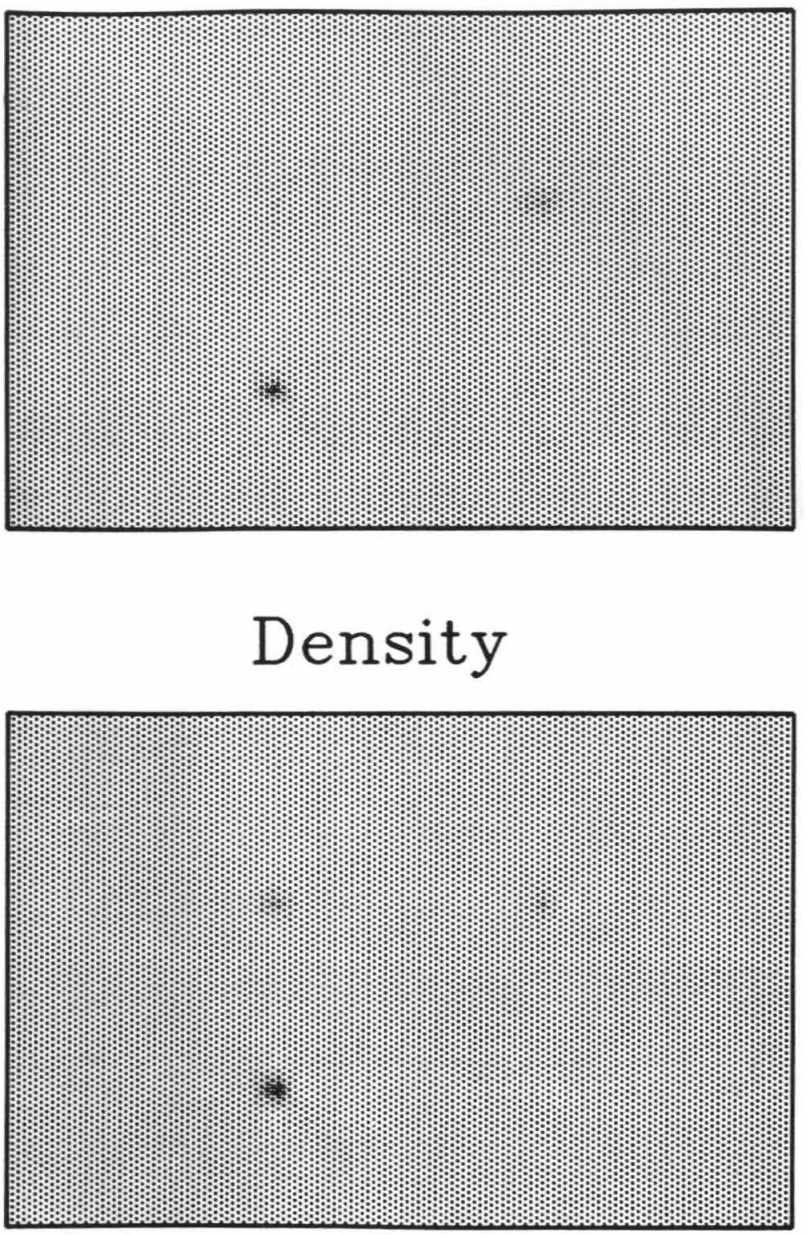

Figure 3.11 - Fifth iteration for a maximum offset of 2.3 km.

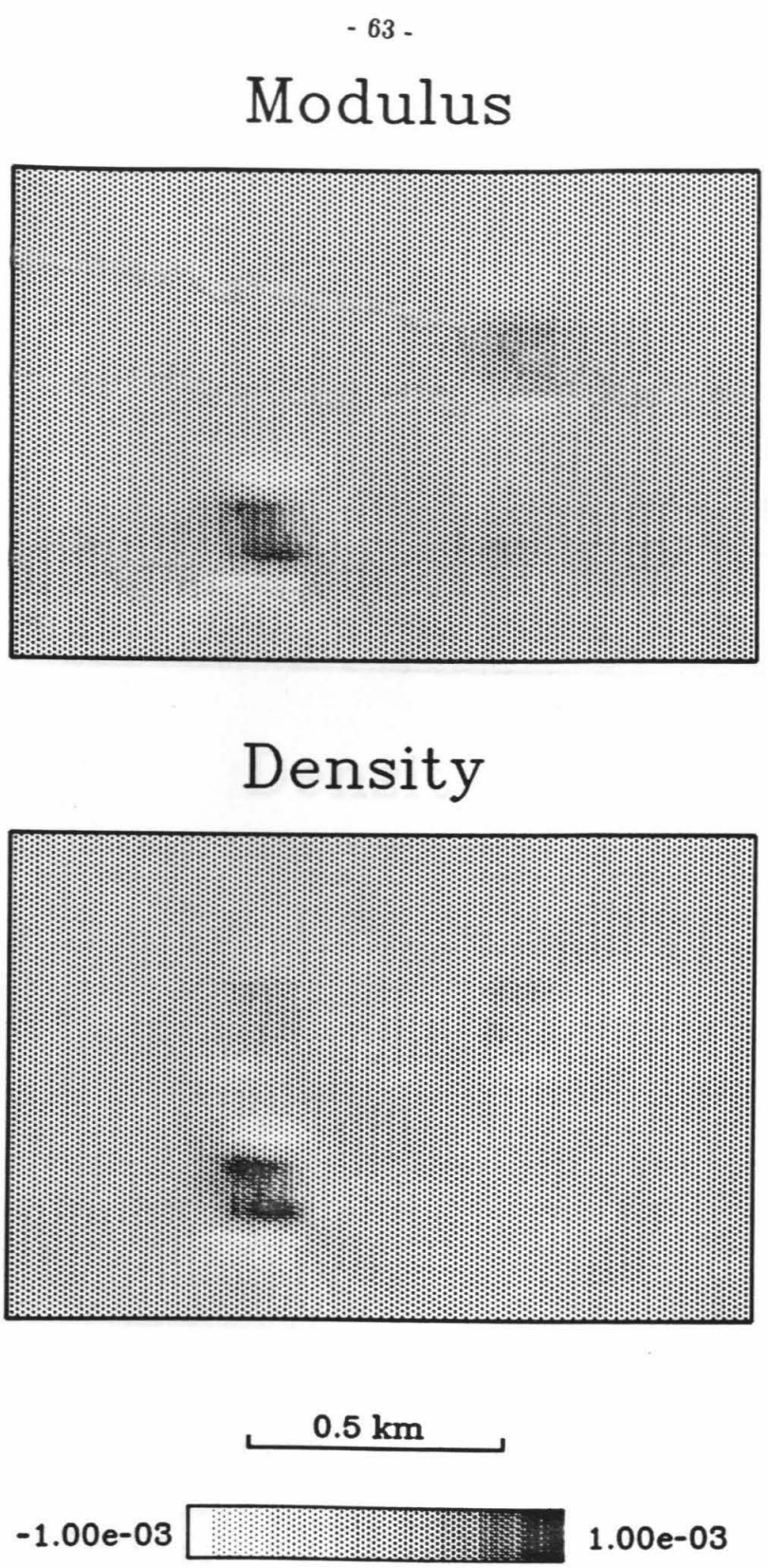

Figure 3.12 - First iteration for a maximum offset of 2.3 km. Smoothed over a disk of radius 2 cells.

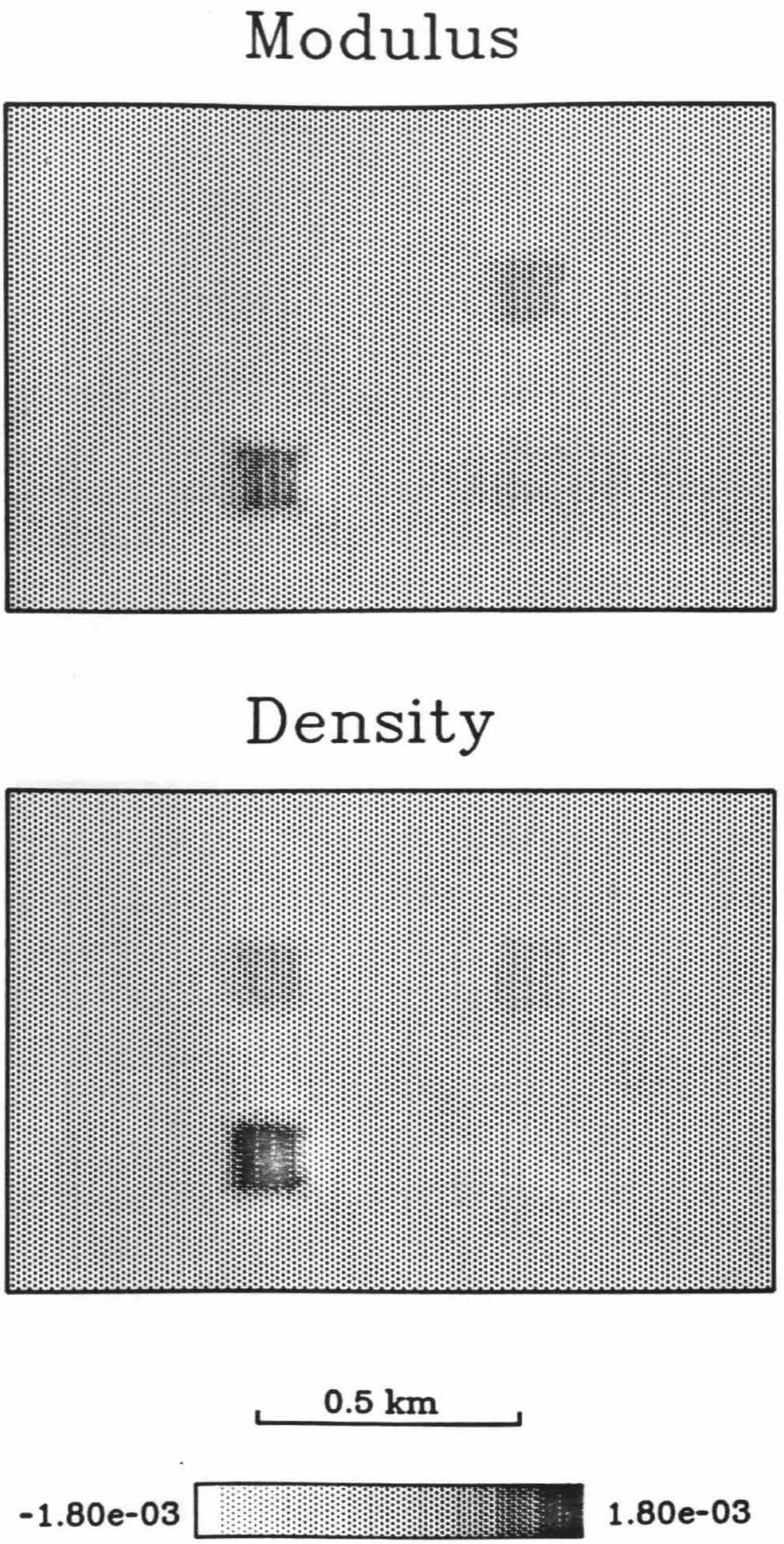

Figure 3.13 - Fifth iteration for a maximum offset of 2.3 km. Smoothed over a disk of radius 2 cells.

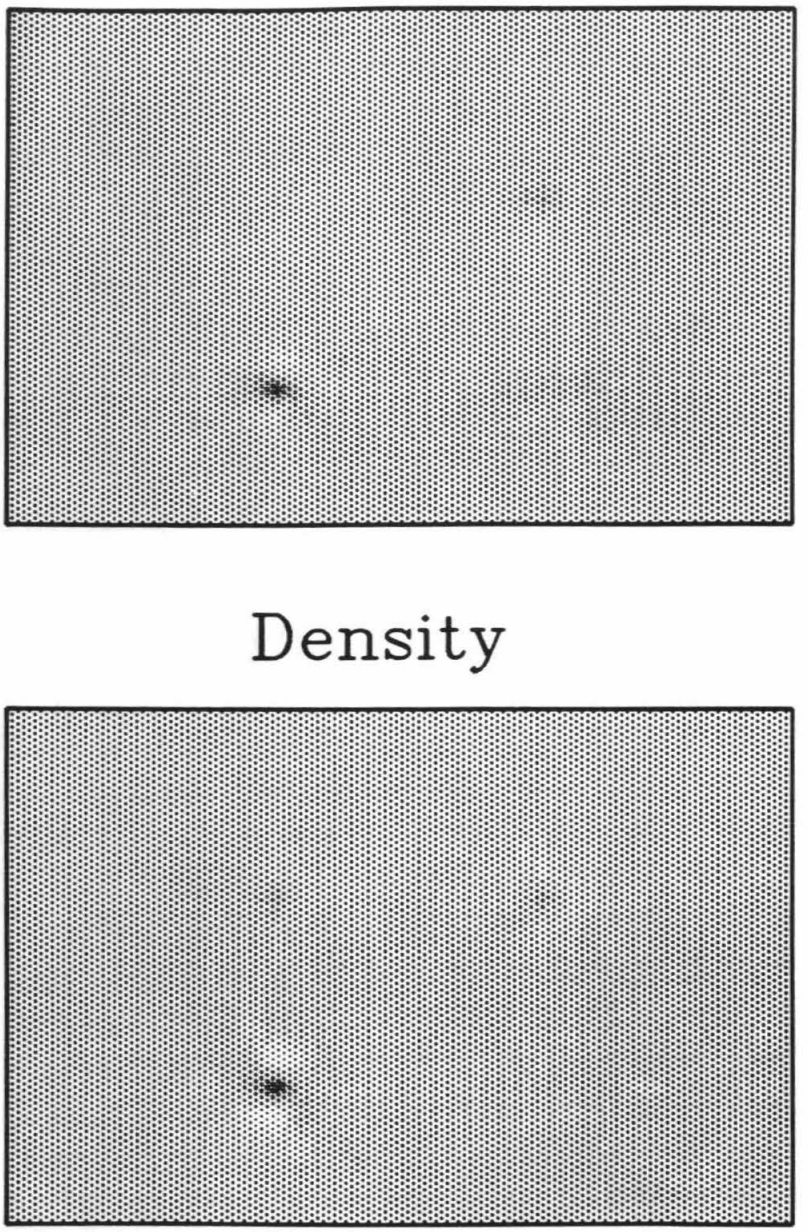

Figure 3.14 - Same as Figure 3.10 for a maximum offset of 4.6 km.

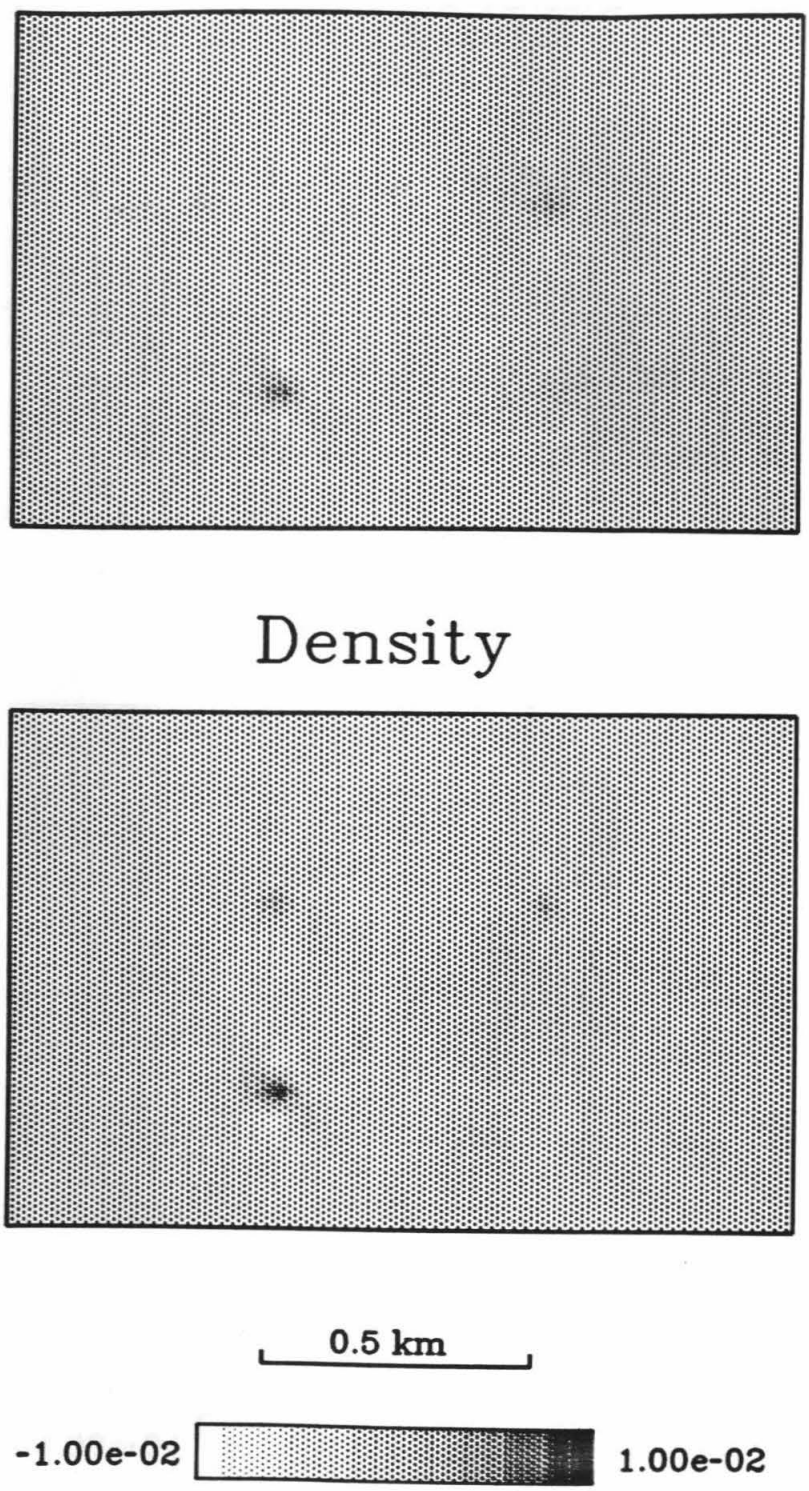

Figure 3.15 - Same as Figure 3.11 for a maximum offset of 4.6 km.

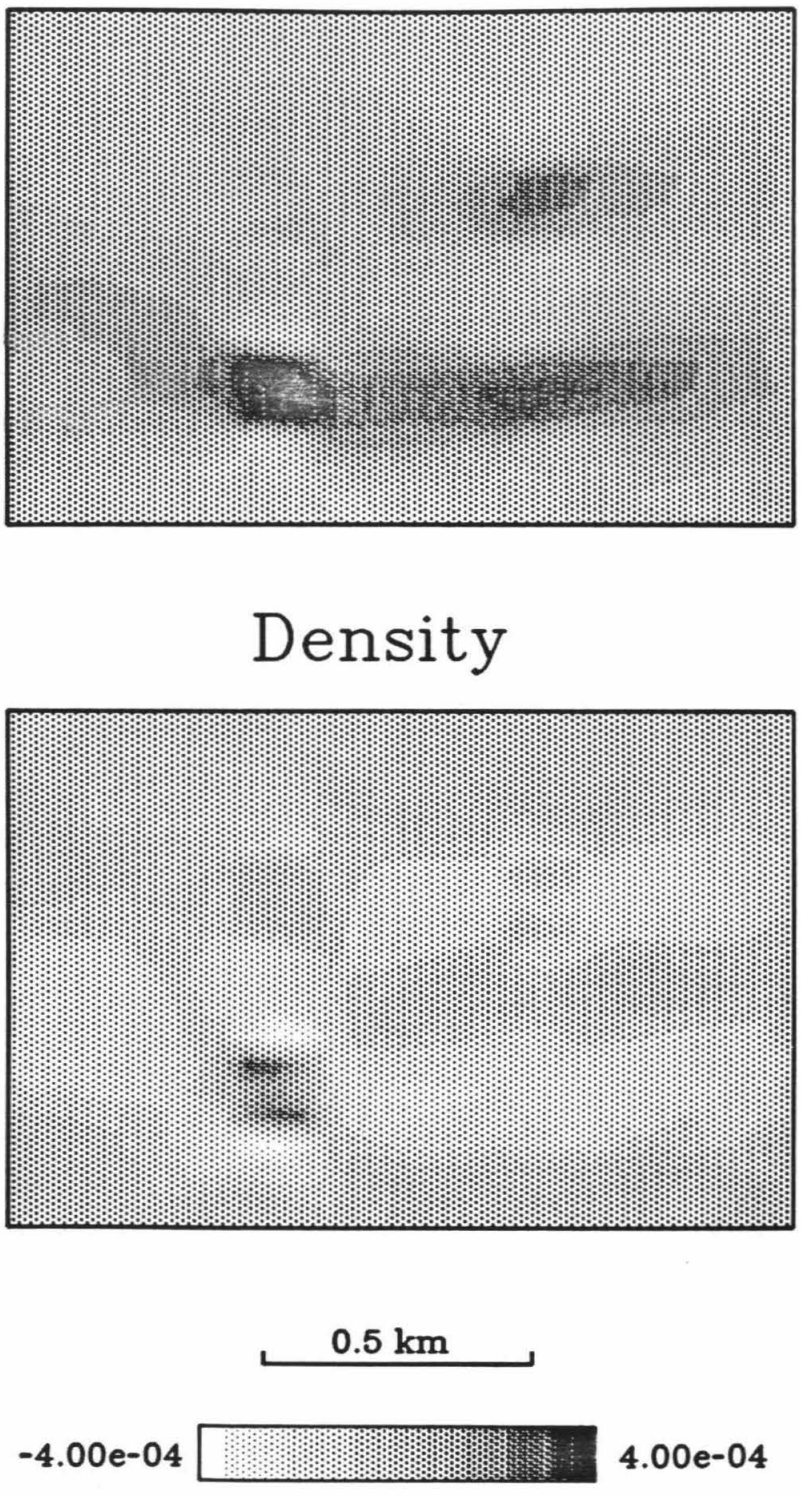

Figure 3.16 - Same as Figure 3.12 for a maximum offset of 4.6 km.

Modulus

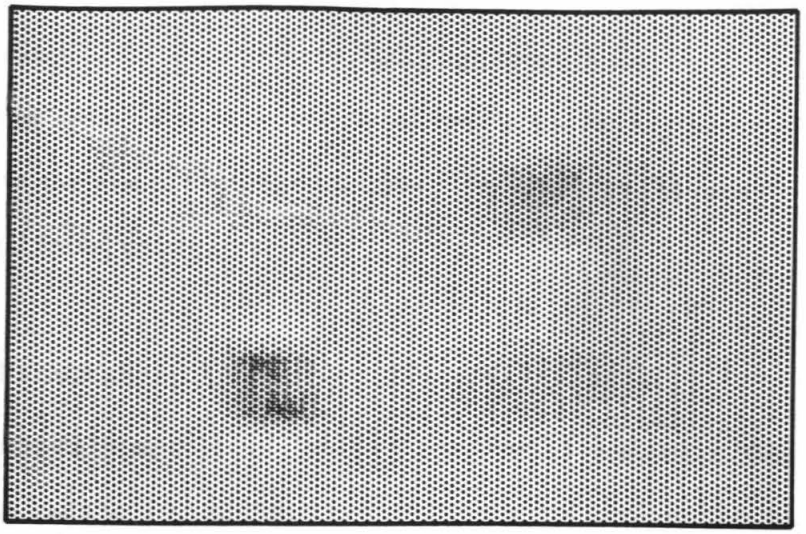

Density

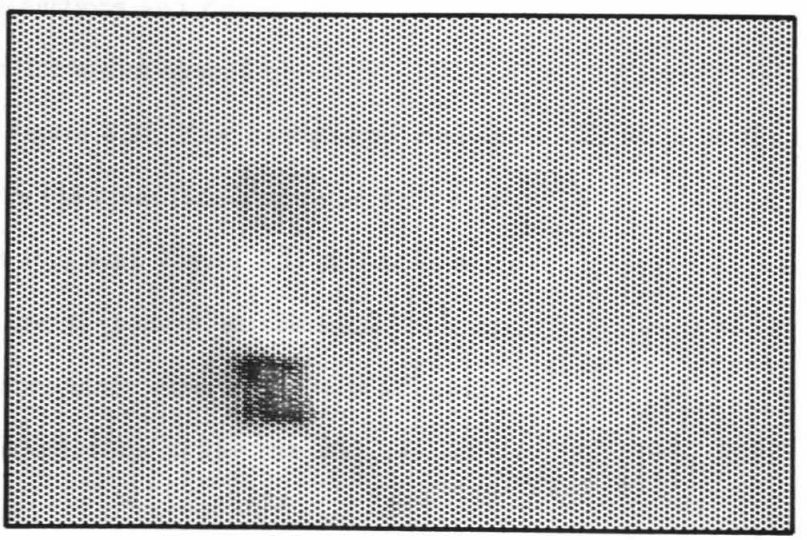

Figure 3.17 - Same as Figure 3.13 for a maximum offsef of 4.6 km.

3.23 to 3.26 show the results of the first and third iterations both unfiltered and filtered. The effect of the noise is more readily apparent in this case but it shows that even in extreme cases, with very low signal over noise ratios, the method is robust with respect to the presence of random noise. This is due to the cancellation of noise along the equal travel time paths.

Disk-shaped anomaly

The examples presented so far have been point scatterers. Since the Born approximation leads to a linear relationship between the medium parameters and the synthetic seismograms, one can think of more complex models as linear superpositions of such point scatterers. Scattered waves then combine and interfere constructively to give rise to reflections and diffractions on objects of diverse shapes. An example of reconstruction for a disk-shaped object presenting a density anomaly of magnitude 1 is shown on Figure 3.27. The background medium is the same as for the previous point scatterers examples (linear increase with depth). The original disk has a diameter of 10 cells (0.5 km). Figure 3.27 shows iterations 1, 3, 5 and 7 of the inversion. The sections are all plotted at the same scale and the buildup in amplitude with iterations is more easily observed on this example. Note also the improvement in the streaking. The reduction in the rms was, respectively, 58%, 69%, 80% and 88% for these iterations.

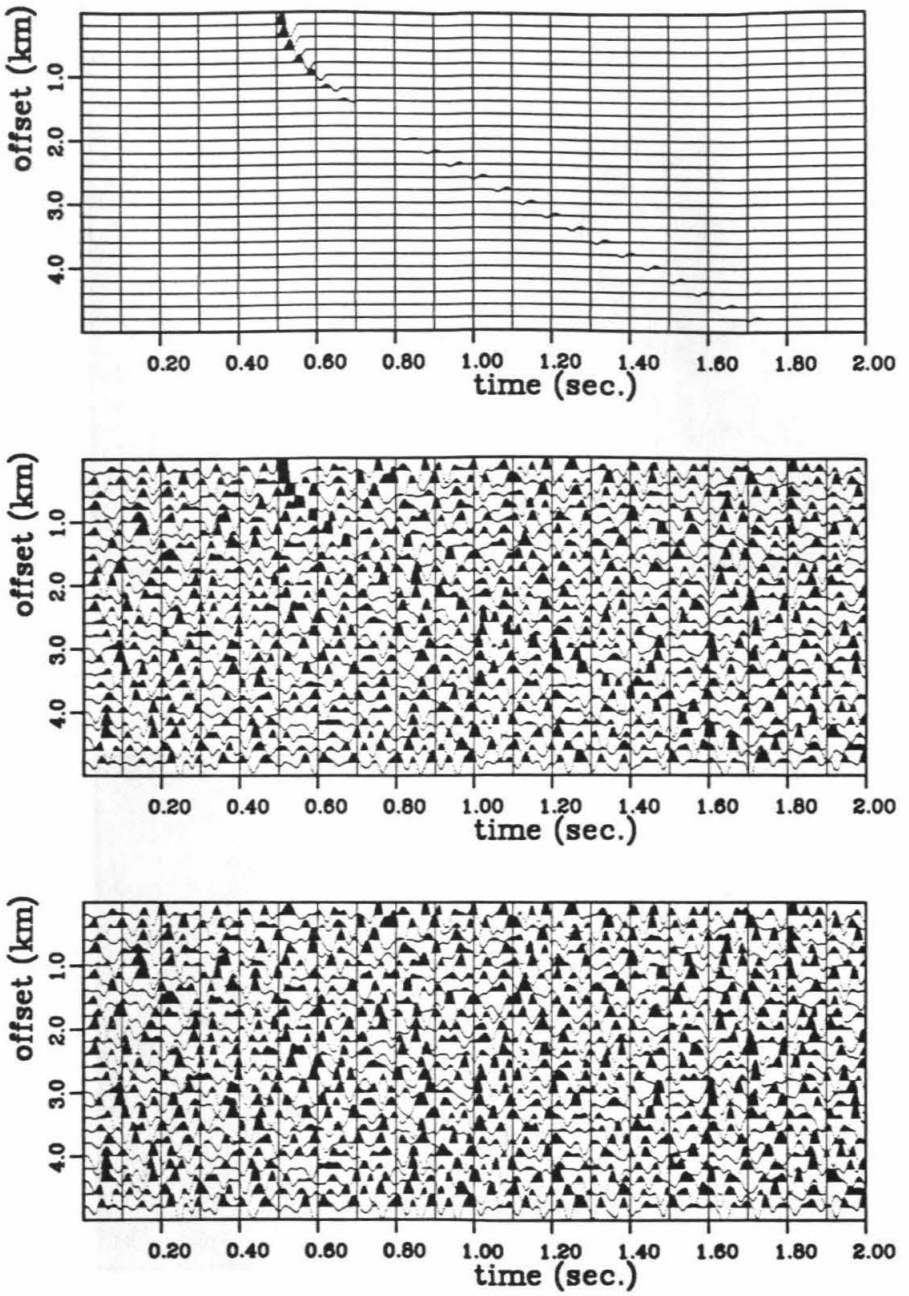

Figure 3.18 - Representative midpoint gather for the density scatterer model. Top is for a signal over noise ratio of ∞, middle of 10 and bottom of 0.05.

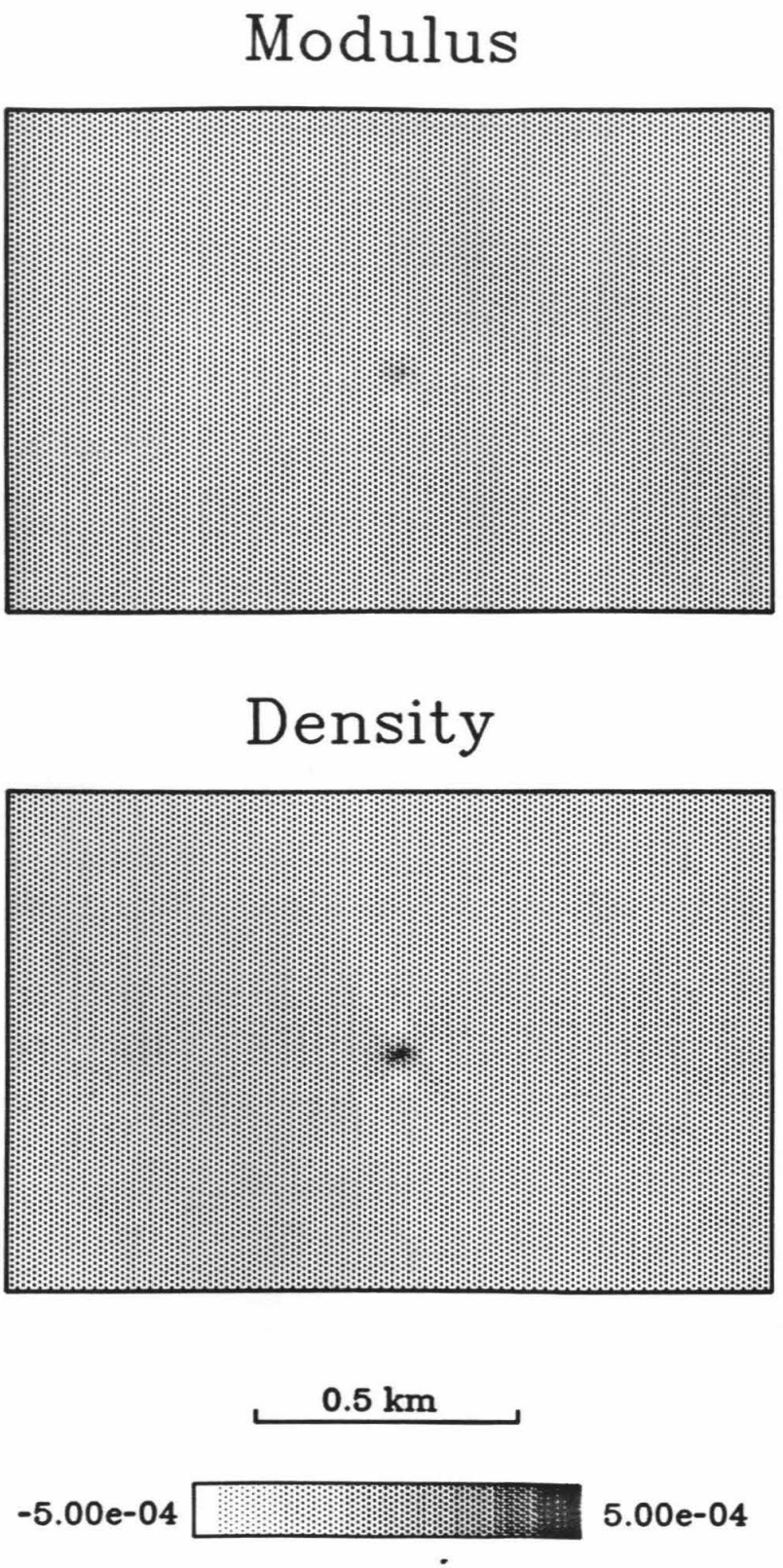

Figure 3.19 - First iteration for a signal over noise ratio of 10.

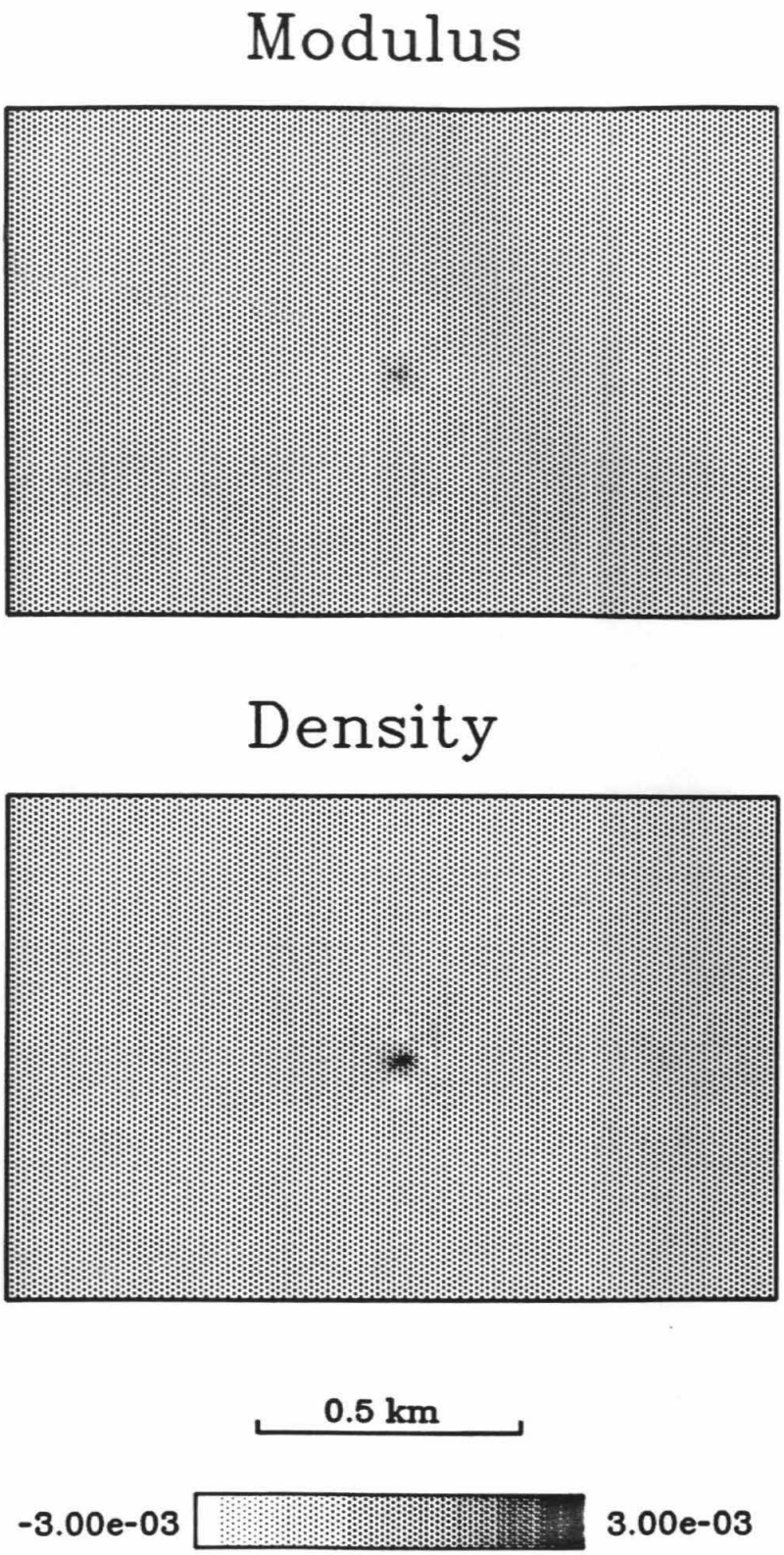

Figure 3.20 - Third iteration for a signal over noise ratio of 10.

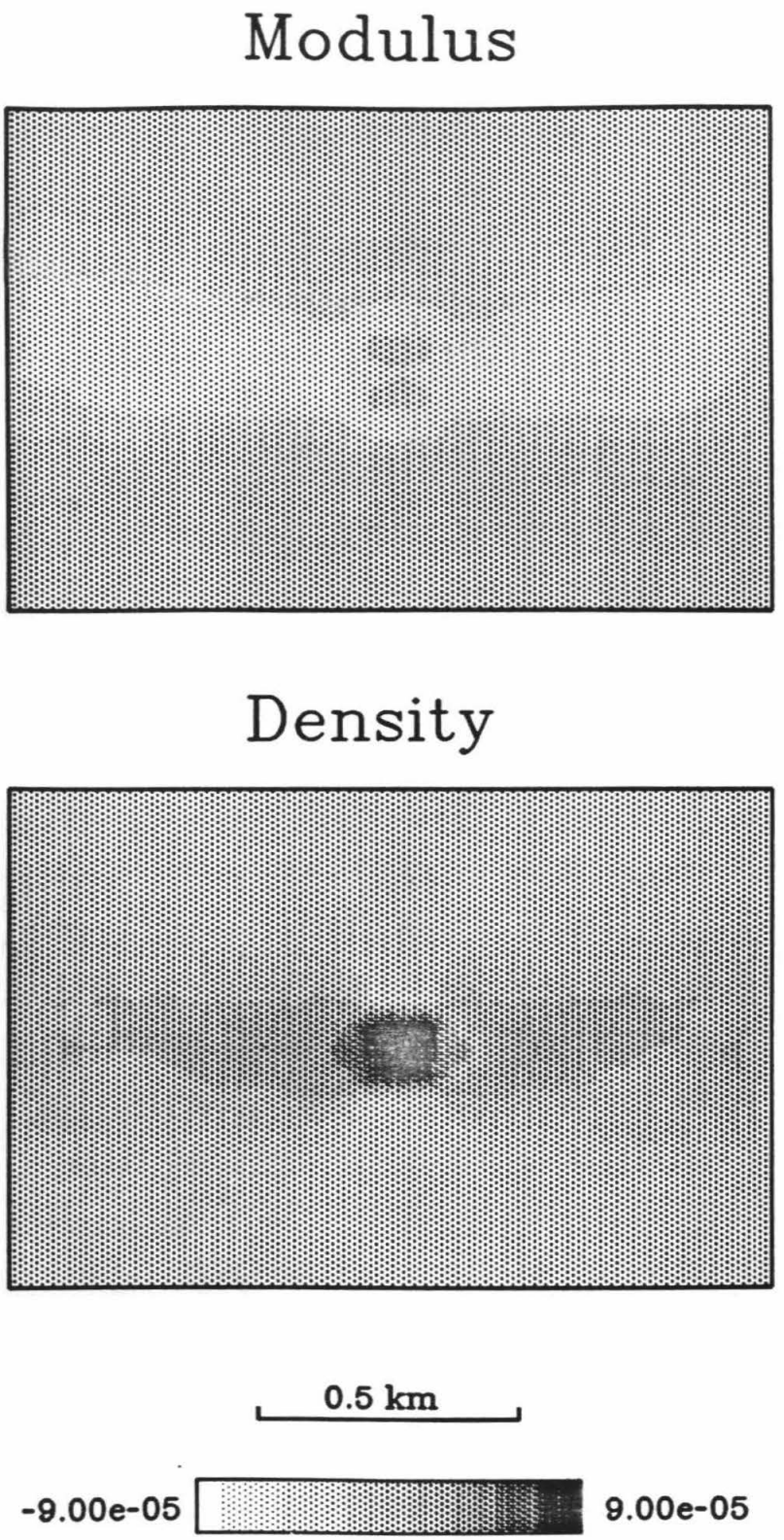

Figure 3.21 - First iteration, smoothed over a disk of radius 2 cells. Signal over noise ratio of 10.

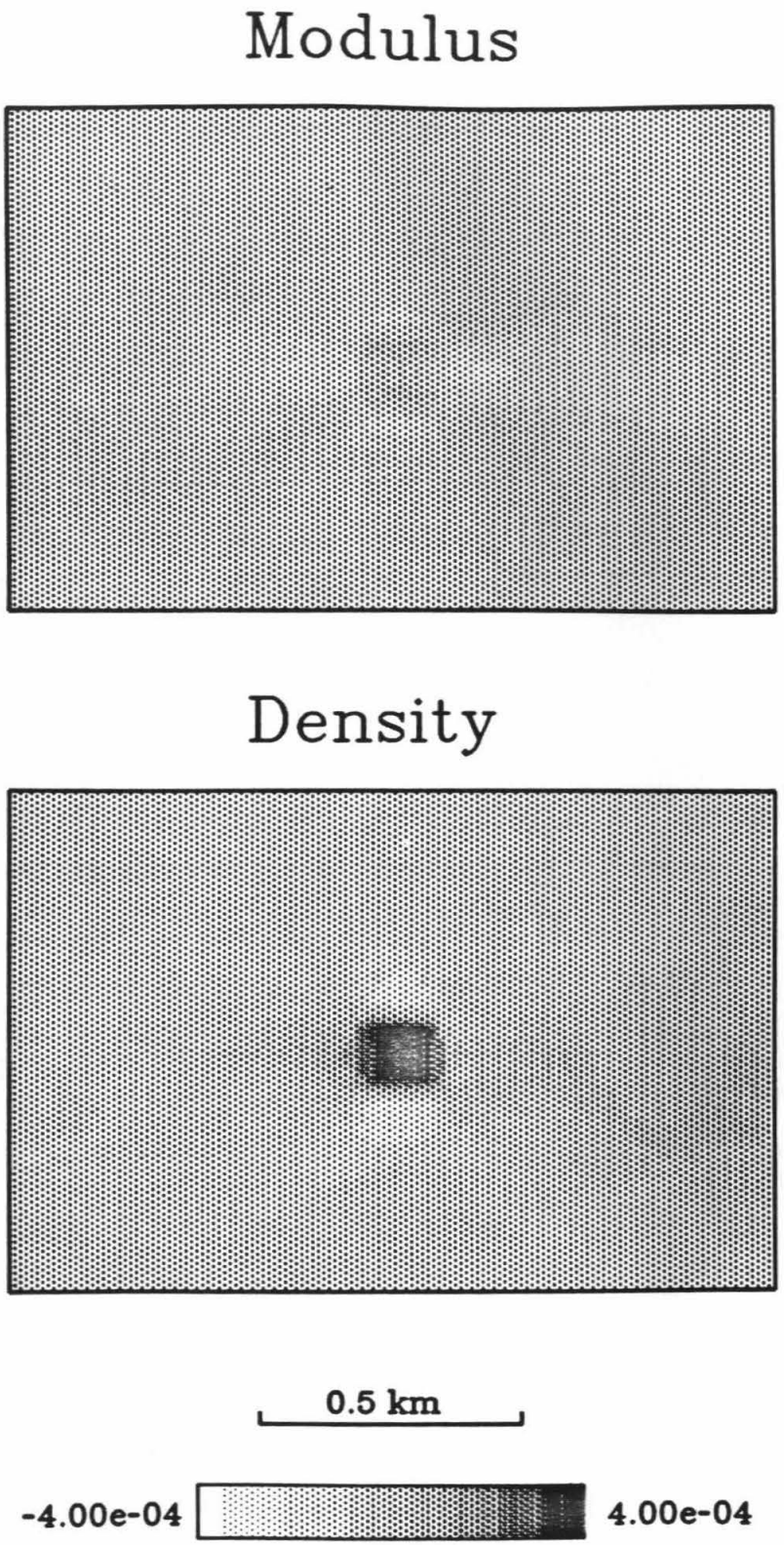

Figure 3.22 - Third iteration, smoothed over a disk of radius 2 cells. Signal over noise ratio of 10.

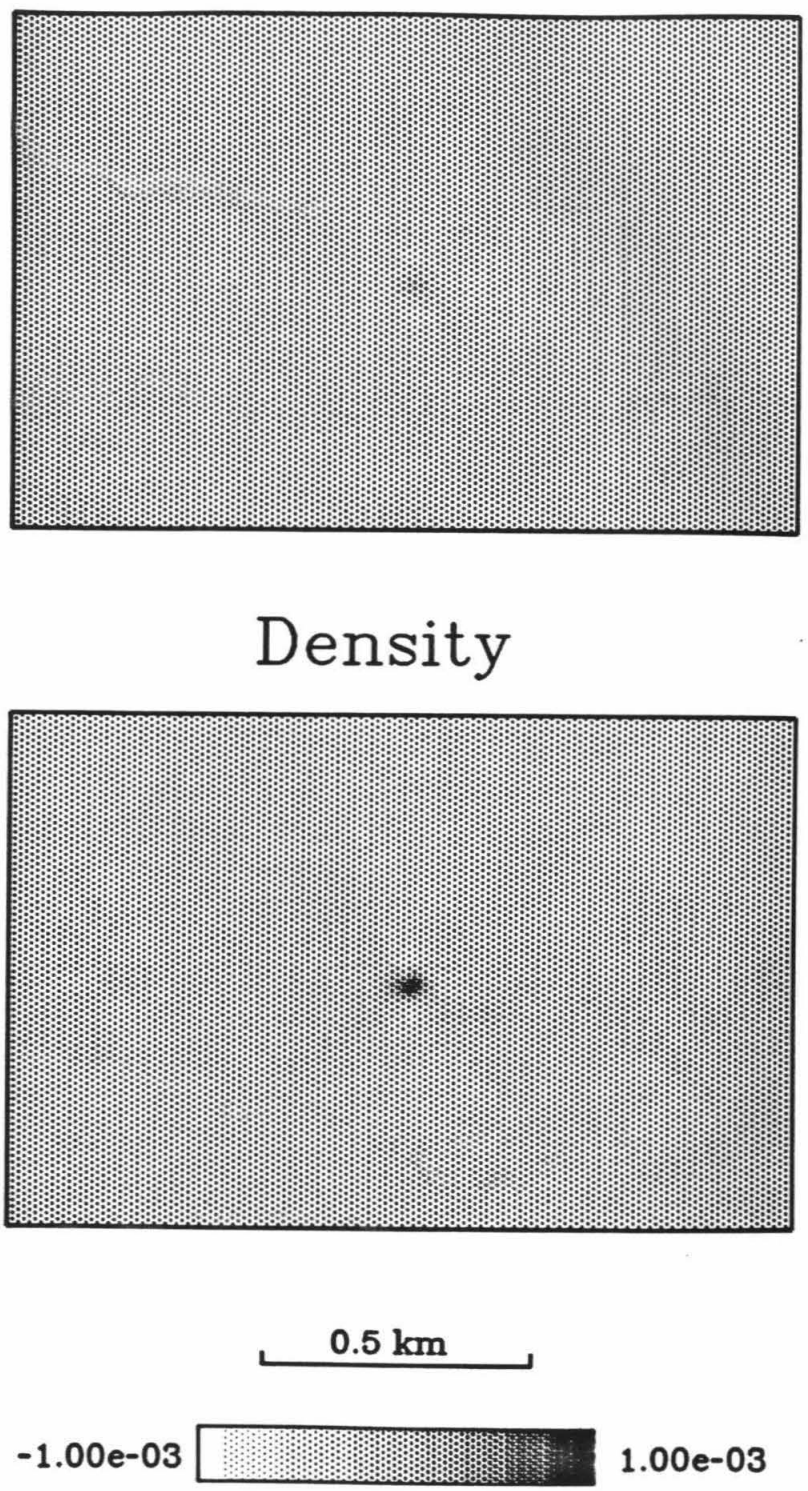

Figure 3.23 - First iteration for a signal over noise ratio of 0.05.

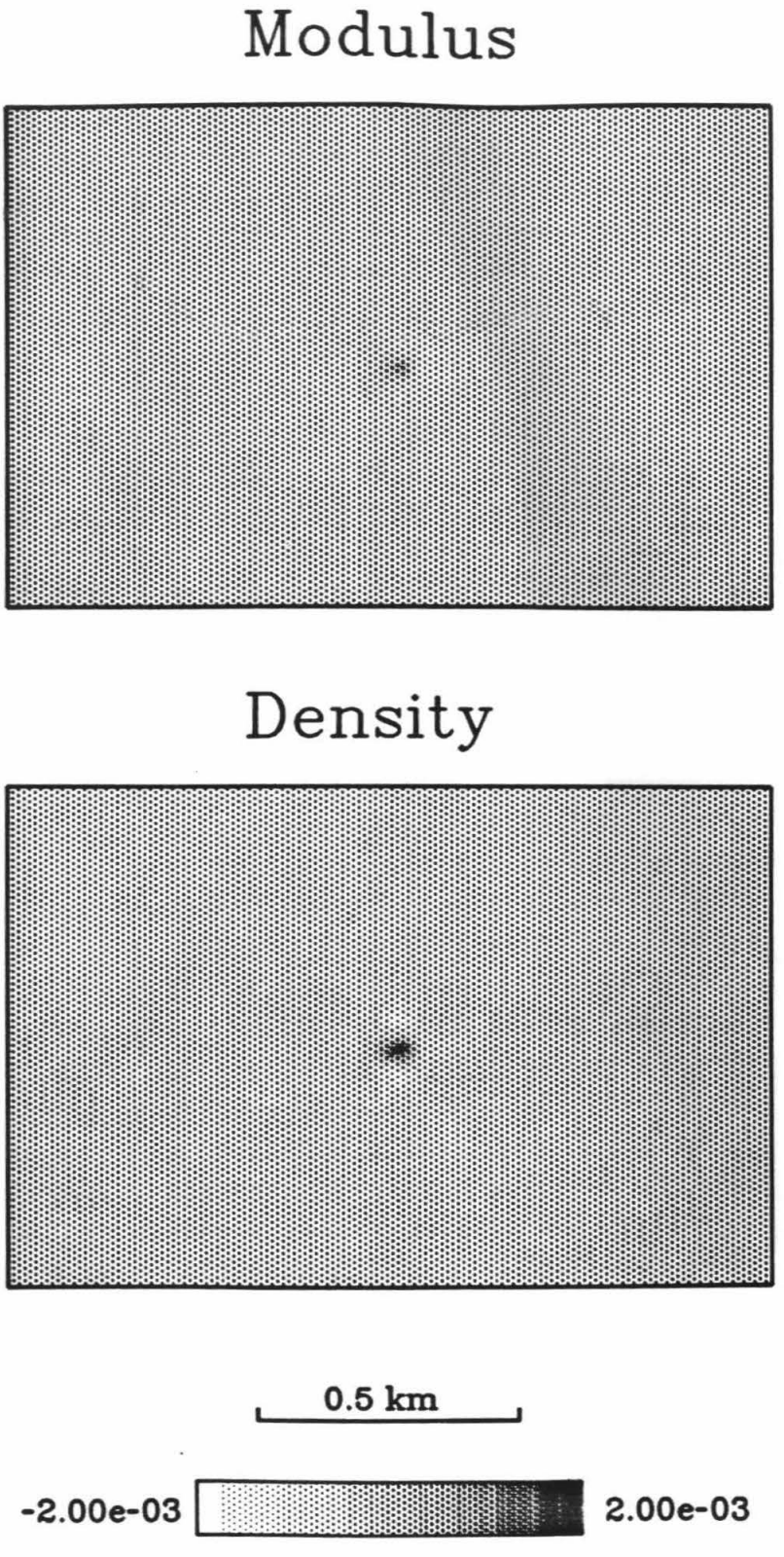

Figure 3.24 - Third iteration for a signal over noise ratio of 0.05.

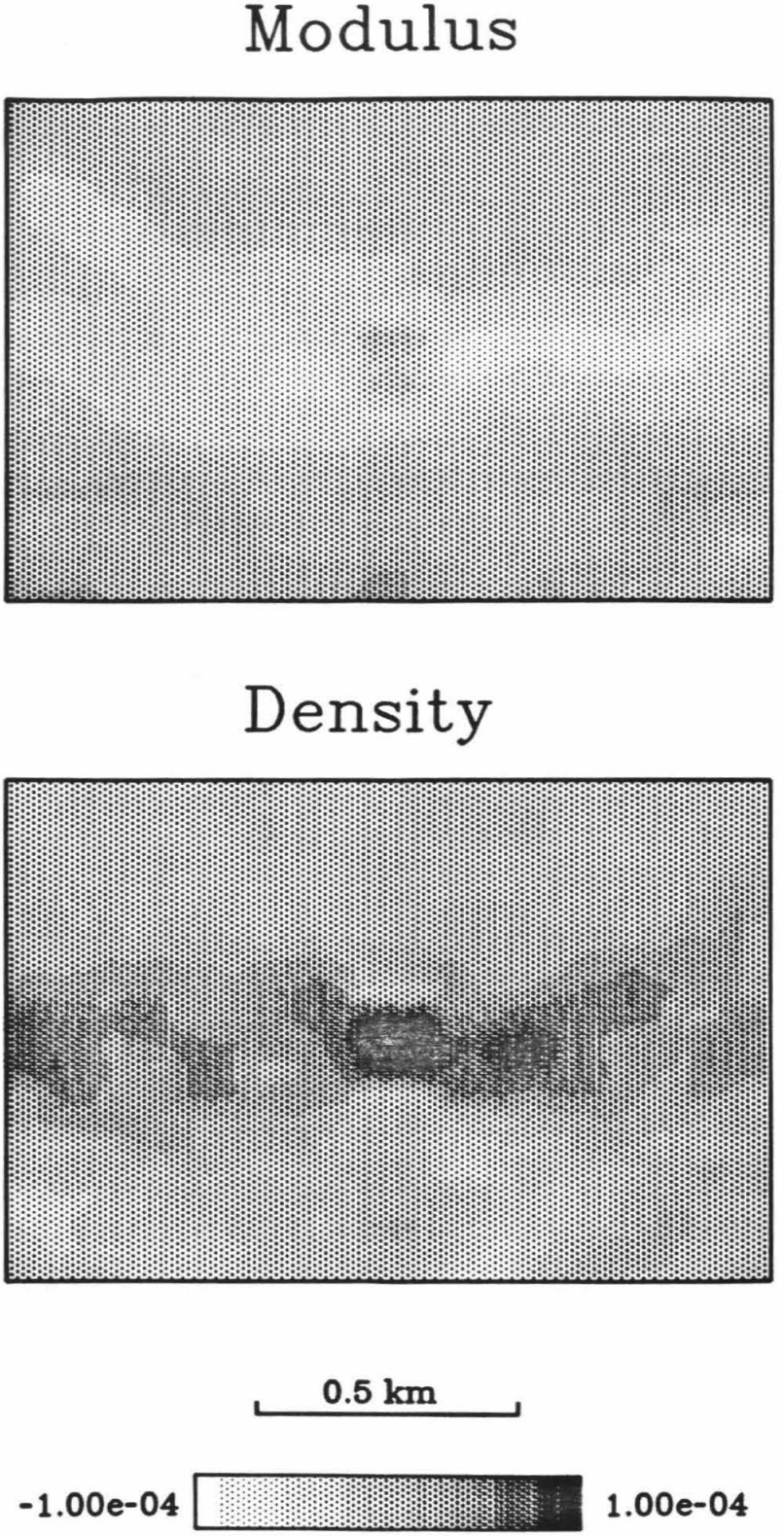

Figure 3.25 - First iteration, smoothed over a disk of radius 2 cells. Signal over noise ratio of 0.05.

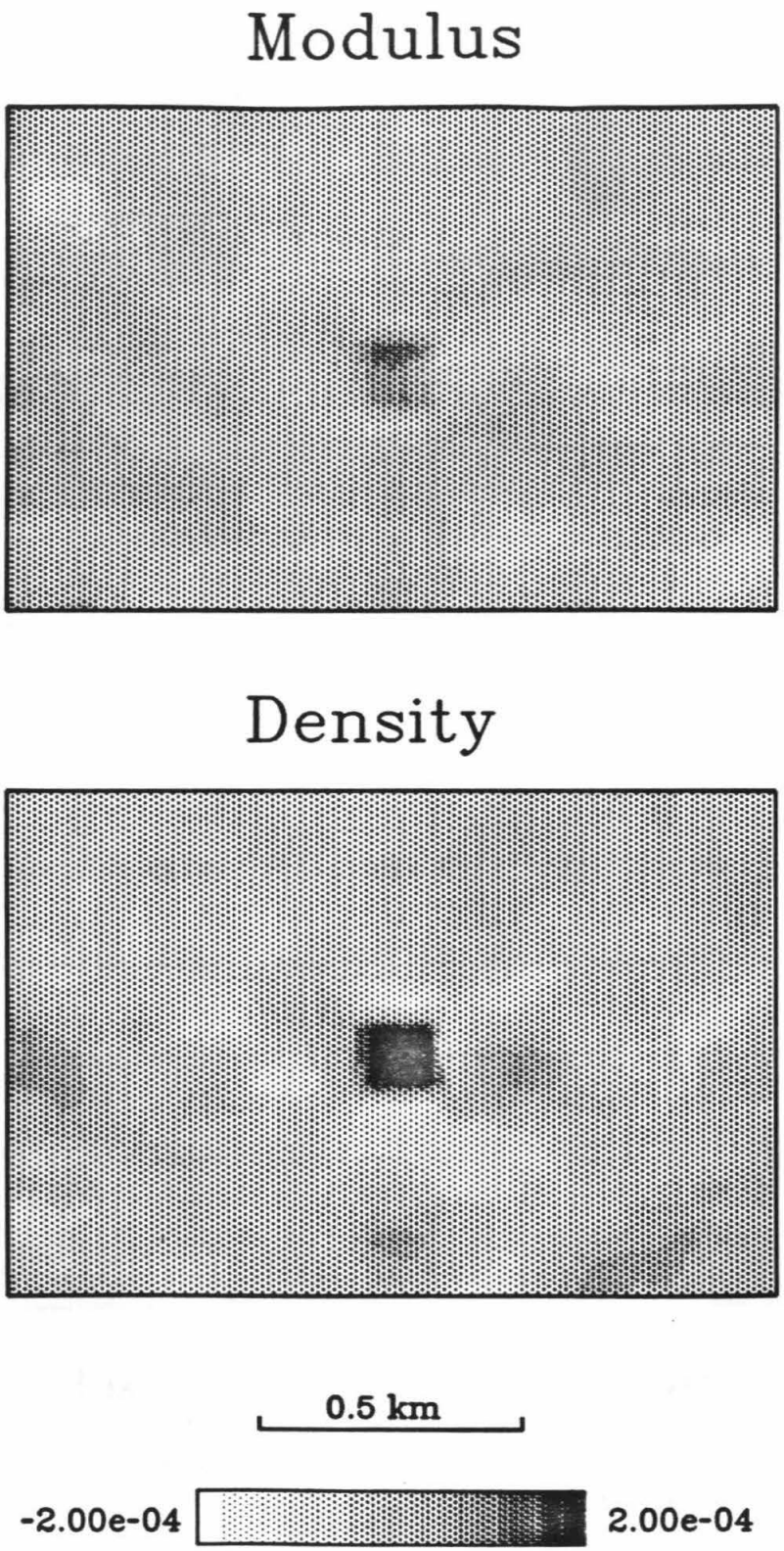

Figure 3.26 - Third iteration, smoothed over a disk of radius 2 cells. Signal over noise ratio of 0.05.

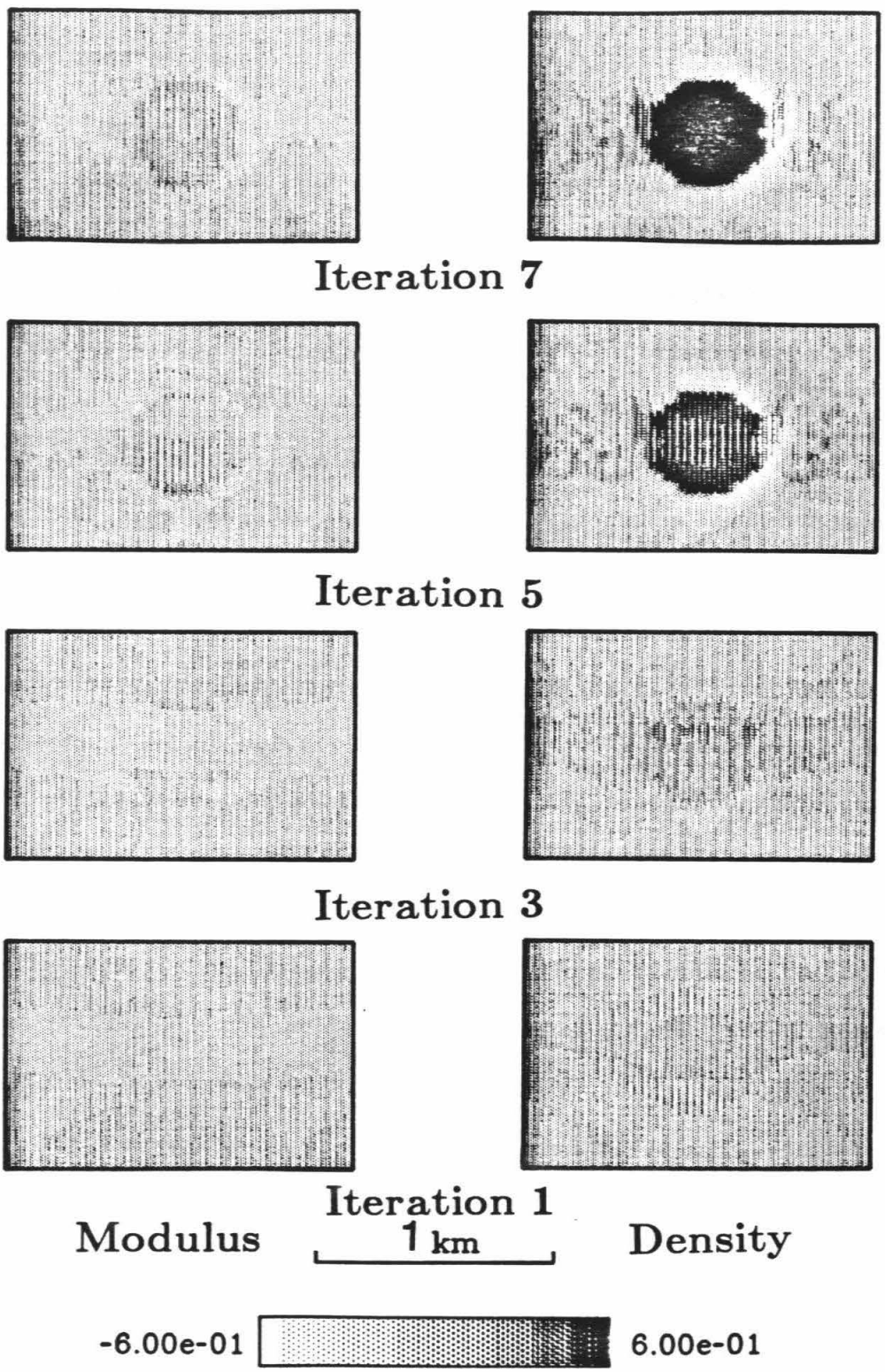

Figure 3.27: Iterations 1, 3, 5 and 7 for a model consisting of a disk-shaped density heterogeneity of amplitude 1.

Conclusion

A method has been presented to invert seismic data for the acoustic parameters of the subsurface. It is based on a Born approximation for the acoustic wavefield and a further far-field approximation. It is applicable when the background acoustic parameters are slowly varying functions of space. The Green's functions can then be computed using a WKBJ approximation. The method is iterative, and each of its steps resembles a before-stack Kirchhoff migration. The difference with a before-stack Kirchhoff migration is that coefficients multiply the backprojected field. These coefficients depend upon the geometrical spreading and the angle between incident and scattered wave. The method was tested on synthetically generated data and it was shown that a good image of the impedance can be obtained even after a few iterations. When the data contain large offsets, a differentiation is possible between two independent acoustic parameters. The method has many similarities with tomographic reconstruction methods. They are based on the same mathematics, both of them using a gradient method to minimize the norm of the residuals. The iterations are based on the application of the transposed linear operator on the residuals and then the direct operator on the model thus derived. An amplitude buildup with successive iterations is observed, as with tomography.

We demonstrated the applicability of this method on actual data, with a noise analysis and examples which involved data sets comparable in size to actual surveys. We neglected in this chapter to analyze several factors influencing the amplitude of seismic data. These are, among others, the radiation pattern of the source, in which the effect of the free surface can be taken into account, the receiver array

attenuation, which is a function of the incident angle on the array of receivers and, perhaps most important, the anelastic attenuation of the medium. The source radiation pattern problem can be easily tackled with the high frequency approximation approach used here. In the next chapter, the radiation pattern due to a point force over a free surface is presented, for elastic waves.

Chapter 4

Inversion of Seismic Data for the Elastic Parameters

Abstract

The Born approximation for the two-dimensional elastic wave equation is introduced. A WKBJ and far-field approximation further lead to an expression for the scattered wavefield as a sum of scattered rays. The displacement field can be written as a sum of rays corresponding to the four basic types of scattered rays (P-P, P-S, S-P, S-S). Similarly to the acoustic case, an inversion algorithm is proposed to invert the seismic data. This method is suitable when the acoustic equation is not adequate to describe the wavefield, namely, at large offsets for surface data, or for large offset VSP data, where converted waves become an important part of the wavefield.

Introduction

In the previous chapters of this thesis, the seismic data have been identified as the result of the interaction of the underlying medium with propagating acoustic waves. The effect of the acoustic parameters of the medium on the amplitudes of the seismic waves was investigated using the first-order Born approximation model. It was shown that the data can be inverted for the acoustic parameters of the subsurface for a seismic reflection geometrical configuration provided that the medium does not include large amplitude heterogeneities. In addition, it was found that the

information sought after, namely, the separation of two parameters from the data (e.g., density and bulk modulus, or velocity and impedance) can be obtained if the angular coverage is sufficiently large (meaning large offsets for the usual reflection line experiment). In the seismic reflection configuration, the backscattered energy consists mostly of compressional waves for a medium that does not present steeply dipping interfaces. The P to S reflection coefficient is small compared to the P to P reflection coefficient for near-normal incidence. Kennet (1979) showed that the converted shear-wave energy is significant at large offsets for surface reflection data. In the offset-VSP geometry, prominent converted waves are observed (Gal'perin, 1974) for wide offsets. They contain additional information about the medium, namely the shear modulus variations of the medium. In this chapter, we develop an extension of the previously investigated backprojection method, in which the effect of the elastic propagation is taken into account, including converted phases. Since the amplitude of the data plays a major role in determining the physical parameters, it is desirable to describe the wavefield as well as possible. In particular, the elastic reflection coefficients derived from the use of the Born approximation on the elastic equation should be used instead of the acoustic coefficients.

Elastic Born approximation

The homogeneous (no source terms) two-dimensional elastic displacement equation for an isotropic medium can be derived from the stress-strain relations:

$$\sigma_{ij} = \lambda \Delta \delta_{ij} + 2\mu \epsilon_{ij}$$

where: σ_{ij} : stress tensor ϵ_{ij} : strain tensor λ and μ: Lamé ' s parameters

and the fundamental equation of motion:

$$\sigma_{ij,j} = \rho\ddot{\mathbf{u}}_i \text{ where } \mathbf{u} \text{ is the displacement vector.}$$

If λ and μ are not constant as a function of the space variables, we obtain the following linear equation for $\mathbf{u}$:

$$L\,\mathbf{u} = \left[\partial_z A\,\partial_z + \partial_z B\,\partial_x + \partial_x B^T\,\partial_z + \partial_x C\,\partial_x + \rho\omega^2 I\right]\mathbf{u} = 0 \qquad (4.1)$$

where

$$A = \begin{pmatrix} \mu & 0 \\ 0 & \lambda+2\mu \end{pmatrix} \qquad B = \begin{pmatrix} 0 & \mu \\ \lambda & 0 \end{pmatrix}$$

$$C = \begin{pmatrix} \lambda+2\mu & 0 \\ 0 & \mu \end{pmatrix} \qquad I = \begin{pmatrix} 1 & 0 \\ 0 & 1 \end{pmatrix}.$$

It is convenient for our purpose to rewrite the operator L in the form (Clayton, 1981):

$$L = \nabla \begin{pmatrix} \gamma & 0 \\ 0 & \mu \end{pmatrix} \nabla^T + 2H \begin{pmatrix} 0 & \mu \\ \mu & 0 \end{pmatrix} H^T - 2H^T \begin{pmatrix} 0 & \mu \\ \mu & 0 \end{pmatrix} H + \rho\omega^2 I \qquad (4.2)$$

where

$$\nabla = \begin{pmatrix} \partial_x & -\partial_z \\ \partial_z & \partial_x \end{pmatrix} \qquad H = \begin{pmatrix} 0 & \partial_z \\ \partial_x & 0 \end{pmatrix}$$

are symbolic operator matrices and $\gamma=\lambda+2\mu$. note that :

$$\nabla^T \nabla = \nabla \nabla^T = (\partial_{xx} + \partial_{zz}) I$$

and

$$H^T \begin{pmatrix} 0 & 1 \\ 1 & 0 \end{pmatrix} H = H \begin{pmatrix} 0 & 1 \\ 1 & 0 \end{pmatrix} H^T = \partial_x \partial_z \begin{pmatrix} 0 & 1 \\ 1 & 0 \end{pmatrix}.$$

In Clayton and Stolt (1981) the Born approximation to the Lippmann-Schwinger equation was introduced and stated to be : $G = G_0 + G_0 V G_0$ where G is the Green's operator for the equation, formally defined as $G = -L^{-1}$ and G_0 is the Green's operator for the wave equation with slowly varying Lamé 's parameters and density and V is the scattering potential ($V = L - L_0$).

In the elastic case, G is a matrix operator instead of a scalar operator as in the acoustic case. The Green's function G_0 for the slowly varying background satisfies the equation :

$$\rho_0 \omega^2 G_0 + \nabla \begin{pmatrix} \gamma_0 & 0 \\ 0 & \mu_0 \end{pmatrix} \nabla^T G_0 + 2 H \begin{pmatrix} 0 & \mu \\ \mu & 0 \end{pmatrix} H^T G_0 - 2 H^T \begin{pmatrix} 0 & \mu \\ \mu & 0 \end{pmatrix} H G_0 = \delta(\mathbf{x} - \mathbf{x_s}) S(\omega).$$

The scattering potential is :

$$V = (\rho - \rho_0)\omega^2 I + \nabla \begin{pmatrix} \gamma - \gamma_0 & 0 \\ 0 & \mu - \mu_0 \end{pmatrix} \nabla^T + 2H \begin{pmatrix} 0 & \mu \\ \mu & 0 \end{pmatrix} H^T - 2H^T \begin{pmatrix} 0 & \mu \\ \mu & 0 \end{pmatrix} H. \qquad (4.3)$$

Defining the dimensionless parameters

$$a_1 = \frac{\rho}{\rho_0} - 1 \qquad a_2 = \frac{\gamma}{\gamma_0} - 1 \qquad a_3 = \frac{\mu}{\mu_0} - 1$$

V can be expressed as :

$$V = \rho_0 \left[a_1 \omega^2 I + \nabla \begin{pmatrix} \alpha^2 a_2 & 0 \\ 0 & \beta^2 a_3 \end{pmatrix} \nabla^T + 2\beta^2 H \begin{pmatrix} 0 & a_3 \\ a_3 & 0 \end{pmatrix} H^T - 2\beta^2 H^T \begin{pmatrix} 0 & a_3 \\ a_3 & 0 \end{pmatrix} H \right] \qquad (4.4)$$

where α and β are the background P and S velocities :

$$\alpha = \sqrt{\frac{\gamma_0}{\rho_0}} \qquad \beta = \sqrt{\frac{\mu_0}{\rho_0}}.$$

Introducing a point source and a time function $S(\omega)$, the observed reflected waves can be related to the scattering potential by :

$$D(x_g, x_s, \omega) = G_0 V G_0 F S(\omega) \tag{4.5}$$

where F is a two-component vector including the radiation pattern of the source being used in the experiment. We later discuss this term in our application on VSP data, for a surface point load.

Background elastic Green's functions and the WKBJ approximation

For some background media, the expressions for the background Green's functions can be computed analytically. This is the case for a slowly varying medium. The Green's function G_0 for the slowly varying background satisfies the equation :

$$\rho_0 \omega^2 G_{0+} \nabla \begin{pmatrix} \gamma_0 & 0 \\ 0 & \mu_0 \end{pmatrix} \nabla^T G_0 + 2 H \begin{pmatrix} 0 & \mu \\ \mu & 0 \end{pmatrix} H^T G_0 - 2 H^T \begin{pmatrix} 0 & \mu \\ \mu & 0 \end{pmatrix} H G_0$$

$$= \delta(\mathbf{x}-\mathbf{x}_s) S(\omega). \tag{4.6}$$

The last two terms of the R.H.S of the equation can be shown to be negligible in the case of a slowly variable medium :

If $G_0 = (u, v)$ where u is the radial component of displacement and v the vertical component of displacement, then :

$$H^T \begin{pmatrix} 0 & \mu \\ \mu & 0 \end{pmatrix} = \begin{pmatrix} (\mu v_z)_z \\ (\mu u_z)_z \end{pmatrix}$$

and :

$$H \begin{pmatrix} \mu & 0 \\ 0 & \mu \end{pmatrix} = \begin{pmatrix} (\mu v_x)_z \\ (\mu u_z)_x \end{pmatrix}.$$

The difference between these two terms involves only the spatial derivatives of μ and hence can be neglected for our slowly varying medium. The Green's function has thus to satisfy the equation :

$$\rho_0 \omega^2 G_0 + \nabla \begin{pmatrix} \gamma_0 & 0 \\ 0 & \mu_0 \end{pmatrix} \nabla^T \; G_0 = \delta(\mathbf{x}-\mathbf{x}_s) S(\omega). \tag{4.7}$$

The potentials of the displacement vector provide a working similarity with the way the acoustic theory was developed. They satisfy the wave equation for the background medium and propagate much the same way as the acoustic potential.

In two dimensions, the elastic potentials are defined by the following relations :

$$u = \phi_x + \psi_z. \qquad v = -\phi_z + \psi_x.$$

They can be shown to satisfy the following wave equations if the partial derivatives of μ with respect to the space variables are neglected :

$$\phi_{xx} + \phi_{zz} + \frac{\omega^2}{\alpha^2}\phi = 0$$

$$\psi_{xx} + \psi_{zz} + \frac{\omega^2}{\beta^2}\phi = 0$$

where α and β are the P-wave and S-wave velocities, respectively. Throughout this chapter, we consider that they are slowly varying functions of the depth z only. The WKBJ theory can be applied to get the solution of these two differential equations (e.g., Aki and Richards, 1980). The WKBJ P-wave potential for a source at 0, z_0 and a receiver at x ,z is given by the expression :

$$\phi_0(k_x, z; 0, z_0; \omega) = \frac{1}{2\pi\rho_0\alpha^2} e^{i\int_{z_0}^{z_P} du\, q(u)} \frac{\cos\left(\int_{z_P}^{z} du q(u)\right)}{2i\left[q(z)q(z_0)\right]^{1/2}} \tag{4.8}$$

where the function $q(z)$ is defined by :

$$q(z) = \left\{\frac{\omega^2}{\alpha^2} - k_x^2\right\}^{1/2}.$$

A turning point z_P is defined by $q(z_P) = 0$.

The SV potential is :

$$\psi_0(k_x, z; 0, z_0; \omega) = \frac{1}{2\pi\rho_0\beta^2} e^{i\int_{z_0}^{z_P} du\, r(u)} \frac{\cos\left(\int_{z_P}^{z} du r(u)\right)}{2i\left[r(z)r(z_0)\right]^{1/2}} \tag{4.9}$$

where $r(z)$ is :

$$r(z) = \left\{\frac{\omega^2}{\beta^2} - k_x^2\right\}^{1/2}.$$

The turning point for S waves is defined in a similar way as for the P waves : $r(z_P) = 0$.

Far-field approximation expression for the elastic WKBJ-Born displacements

Similarly to the acoustic theory developed in Chapter 3 , we now investigate the further approximation that can be introduced for far-field data. The elastic displacement has been expressed in the form :

$$D(x_s, x_g, \omega) = \int_\Omega d\Omega \int dk_g \int dk_s \, e^{ik_g(x_g - x)} \, G_0(k_g, z, \omega)$$

$$V(x, z) e^{ik_s(x - x_s)} \, G_0(k_s, z, \omega) F \; S(\omega). \tag{4.10}$$

The Green's function G_0 for the displacements is obtained from the Green's functions for the potentials ϕ_0 and ψ_0, $G_0 = \nabla . H_0$ where :

$$\nabla = \begin{pmatrix} \partial_x & \partial_z \\ -\partial_z & \partial_x \end{pmatrix} \quad \text{and} \quad H_0 = \begin{pmatrix} \phi_0 \\ \psi_0 \end{pmatrix};$$

ϕ_0 and ψ_0 are the WKBJ potentials. Their expression has been given in the previous paragraph. The scattering potential is a differential operator acting on the Green's functions for the displacements G_0. The derivatives of the potentials with respect to the space variables are :

$$\frac{\partial}{\partial x} \phi_0(x, z; 0, 0; \omega) = ik_s \int dk_s \, e^{ik_s x} \, \phi_0(k_s, z, \omega),$$

and when the spatial derivative terms of velocity are neglected :

$$\frac{\partial}{\partial z} \phi_0(x, z; 0, 0; \omega) = iq_s(z) \int dk_s \, e^{ik_s x} \, \phi_0(k_s, z, \omega).$$

For most experimental configurations for seismic data (surface source and receiver in seismic reflection, and surface source in VSP) the source is at the surface of a half-space. This introduces some complications in the wavefield due mostly to the critical pS wave converted at the surface of the half-space. The P-wave radiation pattern is not very modified; however, the S-wave radiation pattern reflects the importance of the presence of the shear head-wave. This modification of the radiation pattern is included in the source term F. The source term can be evaluated for different types of sources (e.g., in our application, we are going to evaluate it for a vertical surface line

load). Using the relation between displacements and potentials in plane strain, the wavefield can be expressed as :

$$D(x_g, x_s, \omega) = \int_\Omega d\Omega \int dk_g \, e^{ik_g(x_g - x)} \begin{pmatrix} ik_g & \partial_z \\ -\partial_z & ik_g \end{pmatrix} \begin{pmatrix} \frac{-\phi\alpha^2}{\omega^2} & 0 \\ 0 & \frac{-\psi\beta^2}{\omega^2} \end{pmatrix} \begin{pmatrix} \partial_x & -\partial_z \\ \partial_z & \partial_x \end{pmatrix}$$

$$V(x, z) \int dk_s \, e^{ik_s(x - x_s)} \begin{pmatrix} ik_s & \partial_z \\ -\partial_z & ik_s \end{pmatrix} \begin{pmatrix} \phi & 0 \\ 0 & \psi \end{pmatrix} \mathrm{F} \; S(\omega). \tag{4.11}$$

Ignoring the spatial derivative terms of the background medium parameters, and integrating by parts, supposing that the integrals in k_s and k_g vanish at the limits of the domain Ω, we obtain the following expression:

$$D(x_g, x_s, \omega) = \int_\Omega d\Omega \int dk_g \int dk_s \, e^{ik_g(x_g - x)} \begin{pmatrix} ik_g & iq_g \\ -iq_g & ik_g \end{pmatrix} \begin{pmatrix} \frac{-\phi\alpha^2}{\omega^2} & 0 \\ 0 & \frac{-\psi\beta^2}{\omega^2} \end{pmatrix} \begin{pmatrix} ik_g & -iq_g \\ iq_g & ik_g \end{pmatrix}$$

$$V(k_s, q_s; k_g, q_g) \; e^{ik_g(x - x_s)} \begin{pmatrix} ik_s & iq_s \\ -iq_s & ik_s \end{pmatrix} \begin{pmatrix} \phi & 0 \\ 0 & \psi \end{pmatrix} \mathrm{F} \; S(\omega). \tag{4.12}$$

F is the source term for potentials. It is discussed in a later section in the case of a vertical force over a half-space. The expressions for the scattering potential $V(k_s, q_s; k_g, q_g)$ as a function of the horizontal and vertical wavenumbers for the source and receivers are obtained in Appendix C.

At this point, we make a further approximation on the wavefield following the same guidelines as in the acoustic problem (see Appendix B). It is a far-field approximation and corresponds to considering the wavefield as a superposition of rays. The integrals over the source wavenumber k_s and the receiver wavenumber k_g are

approximated by their asymptotic expressions for large ka where k is the wavenumber and a a characteristic distance. We should comment at this point on the effect of the Born approximation on the phenomenon of critical refraction. In the full wave theories, branch cuts in the complex p plane are associated with the presence of head waves. In the case of the Born approximation, however, these branch cuts do not contribute to the integrals, since the stationary points of the integrals (or equivalently saddle points through which the integration contours are passing) are away from them and they represent the major contribution for the integral. We will show this in the following paragraph.

The branch points are associated with the zeroes of ν_s , ν_g , η_s , η_g . The scattering coefficients derived for the four types of scattered waves are given in Appendix C. For each ray, the branch points of the integral corresponding to the ray are for $p = \pm \frac{1}{v(z)}$ and $p = \pm \frac{1}{v(0)}$ where $v(z)$ is the P or S velocity depending on the ray. The scattering potential does not introduce any more branch cut, since for each scattering coefficient the only square roots in the expression are the horizontal slowness for the incident and scattered rays. Therefore, there won't be any critical point phenomenon. If we consider a background medium such that there always exists a ray joining the source and the scatterer and the scatterer and the receiver for both P and S waves, there will be a saddle point with the major contribution to the integral, away from the branch cut. This is illustrated by Figure 4.1. The saddle point is on the real p axis, at the value p_0 corresponding to the slowness of the ray.

As shown in Appendix C the scattering potential is made up of four terms. Each term corresponds to a pair of incident and scattered wave : P-P, P-S, S-P and S-S. Consequently, the expression for the wavefield is the sum of the four terms.

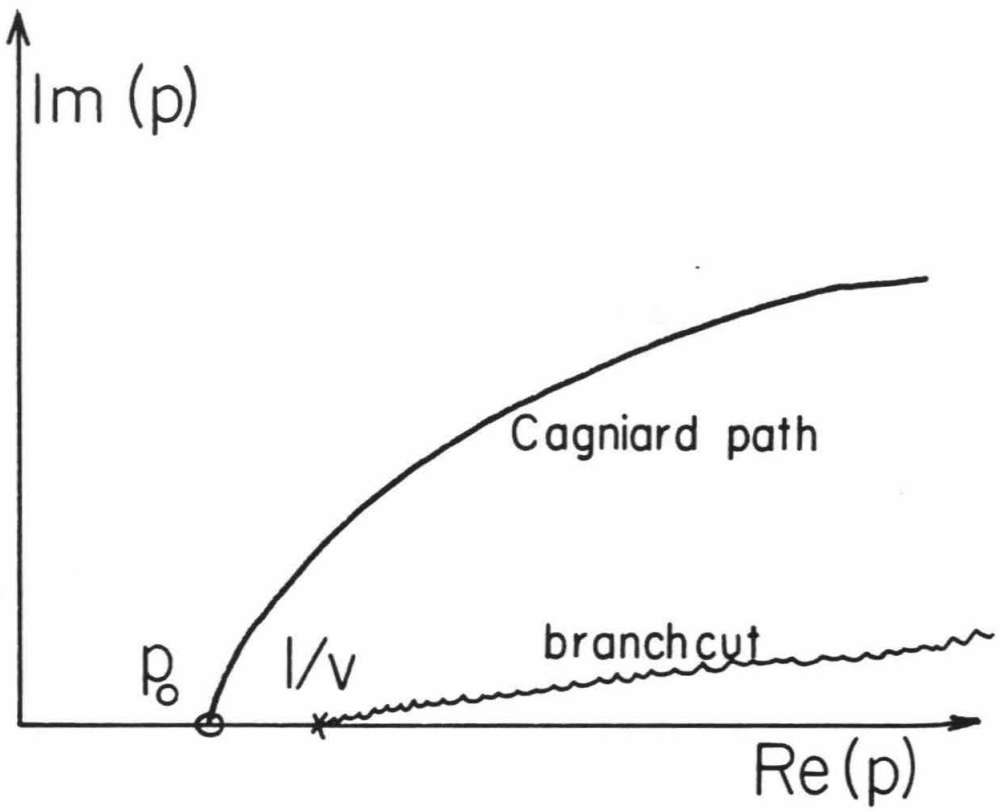

Figure 4.1: Schematic illustration showing the position of the saddle-point p_0, the branch point $\frac{1}{v}$ and the Cagniard path in the complex p plane.

The first part of the wavefield to be studied is the P to P scattered field :

$$D^{PP}(x_g, x_s, \omega) =$$

$$\int_\Omega d\Omega \; e^{i\omega(t_1^P + t_2^P)} \Sigma(x_g, x) \; A^P(x_s, x) A^P(x, x_g) R_{PP}(\theta) \frac{\omega^2}{\alpha^3} \; \mathrm{F}^P(x_s, x) \; S(\omega).$$

The P to S scattered field :

$$D^{PS}(x_g, x_s, \omega) =$$

$$\int_\Omega d\Omega \; e^{i\omega(t_1^P + t_2^S)} \Sigma(x_g, x) \; A^P(x_s, x) A^S(x, x_g) R_{PS}(\theta) \frac{\omega^2}{\alpha\beta^2} \; \mathrm{F}^P(x_s, x) \; S(\omega).$$

The S to P scattered field :

$$D^{SP}(x_g, x_s, \omega) =$$

$$\int_\Omega d\Omega \; e^{i\omega(t_1^S + t_2^P)} \Sigma(x_g, x) \; A^S(x_s, x) A^P(x, x_g) R_{SP}(\theta) \frac{\omega^2}{\alpha^2\beta} \; \mathrm{F}^S(x_s, x) \; S(\omega).$$

The S to S scattered field :

$$D^{SS}(x_g, x_s, \omega) =$$

$$\int_\Omega d\Omega \; e^{i\omega(t_1^S + t_2^S)} \Sigma(x_g, x) \; A^S(x_s, x) A^S(x, x_g) R_{SS}(\theta) \frac{\omega^2}{\beta^3} \; \mathrm{F}^S(x_s, x) \; S(\omega).$$

The Σ factors stem from the first matrices in the integrand of Equation (4.12). They simply correspond to the projection of the potentials on the surface. They are rotation matrices for the angle of incidence on the surface and therefore depend on the positions of the scatterer and geophone. They can also be thought of as the operator transforming potentials into displacements.

t_1^P, t_2^P, t_1^S, t_2^S are the travel times of P and S waves joining the source and the scatterer for subscript 1 and the scatterer and the receiver for subscript 2.

The A factors are amplitude factors related to the geometrical spreading of the rays. Their expressions have been evaluated in Appendix B :

$$A(x, x_s) = \left(\frac{| \nabla p |}{\cos\theta_o} \right)^{1/2}$$

where p is the slowness field for the background velocity, and $| \nabla p |$ notes the magnitude of the gradient of the slowness at the scatterer, and $\cos\theta_o$ is the take-off angle at the source. The scattering coefficients R_{PP}, R_{PS}, R_{SP}, R_{SS} are computed in Appendix C. They depend on the angle of aperture between the incident ray and the scattered ray :

$$R_{PP} = a_1 \cos\theta - a_2 + 2\frac{\beta^2}{\alpha^2} a_3 \sin^2\theta \tag{4.17}$$

$$R_{PS} = a_1 \sin\theta \qquad -\frac{\beta}{\alpha} a_3 \sin 2\theta \tag{4.18}$$

$$R_{SP} = -a_1 \sin\theta \qquad +\frac{\beta}{\alpha} a_3 \sin 2\theta \tag{4.19}$$

$$R_{SS} = a_1 \cos\theta \qquad + a_3 \cos 2\theta. \tag{4.20}$$

Wu and Aki (1985) gave expressions for the amplitude of Rayleigh scattering on small size inclusions in an elastic medium. Their expressions for the scattered potentials agree with our scattering coefficient terms. Everything then happens as if each point in the medium acted as a single scatterer. The total elastic scattered field is the sum of all these scattering points. The wave propagation between the source and the scatterers and between the scatterers and receivers can be described by rays joining the source, scatterers and receivers. The rays propagate in the background medium, ignoring interactions with the other scatterers. A comparison of our scattering

coefficients with the scattering coefficients obtained by Wu and Aki (1985) is made in Appendix D.

Figures 4.2 to 4.4 show comparisons between synthetics computed using an elastic finite difference scheme and the Born approximation synthetics for different values of a point scatterer.

The geometry for the comparison is shown in Figure 4.2. The waves generated are forwardly scattered. The figures illustrate the different patterns generated by different values of the anomaly at the point scatterer. The source is purely compressional and thus only P-P and P-S waves are generated in this configuration.

For an anomaly in P-wave velocity only (or in $\gamma = \lambda + 2\mu$), the scattered wavefield is purely compressional. For density and shear modulus anomalies, the shear waves dominate.

Source radiation pattern: example of a load at a free surface

The problem of a point load at the surface of a half-space is the well-known Lamb problem, and has been investigated by numerous authors (Knopoff and Gilbert, 1959; Miklowitz, 1978). Figure 4.5 illustrates the different types of waves occurring for this problem. The wave pattern due to a vertical line load at the free surface of a half-space is composed of a P wave and an S wave in the region of the half-space such that take-off angles lie in the range $0 < \theta < \beta_{cr}$ where β_{cr} is the critical angle for S waves refracted at the free surface $\sin\beta_{cr} = \frac{\beta}{\alpha}$. Outside this region, for take-off angles such as $\beta_{cr} < \theta < \frac{\pi}{2}$, the wavefield is more complex, involving a P wave, a conical wave pS which is an S head wave and a singular S wave with a two-sided

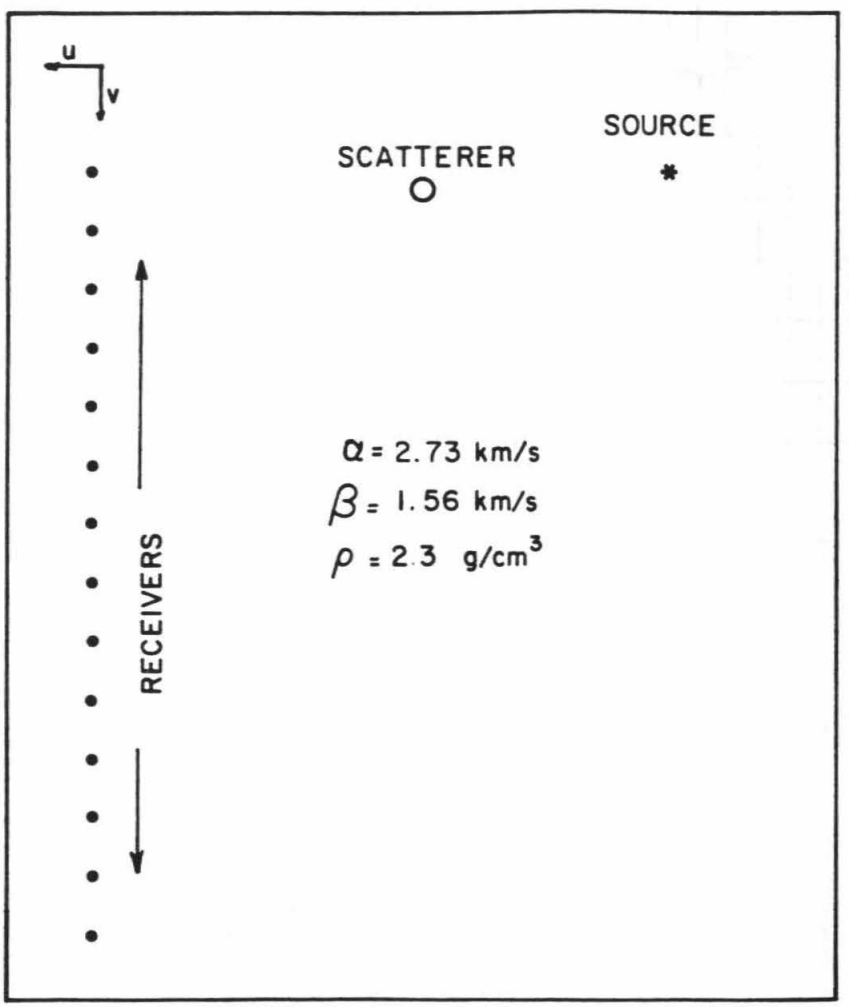

Figure 4.2: Geometry for a one-point scatterer comparison between the Born approximation and a finite difference calculation. α is the P-wave velocity, β the S wave velocity and ρ the density of the background medium. The scatterer differed from these values by 1 percent in each case presented in Figures 4.3, 4.4 and 4.5.

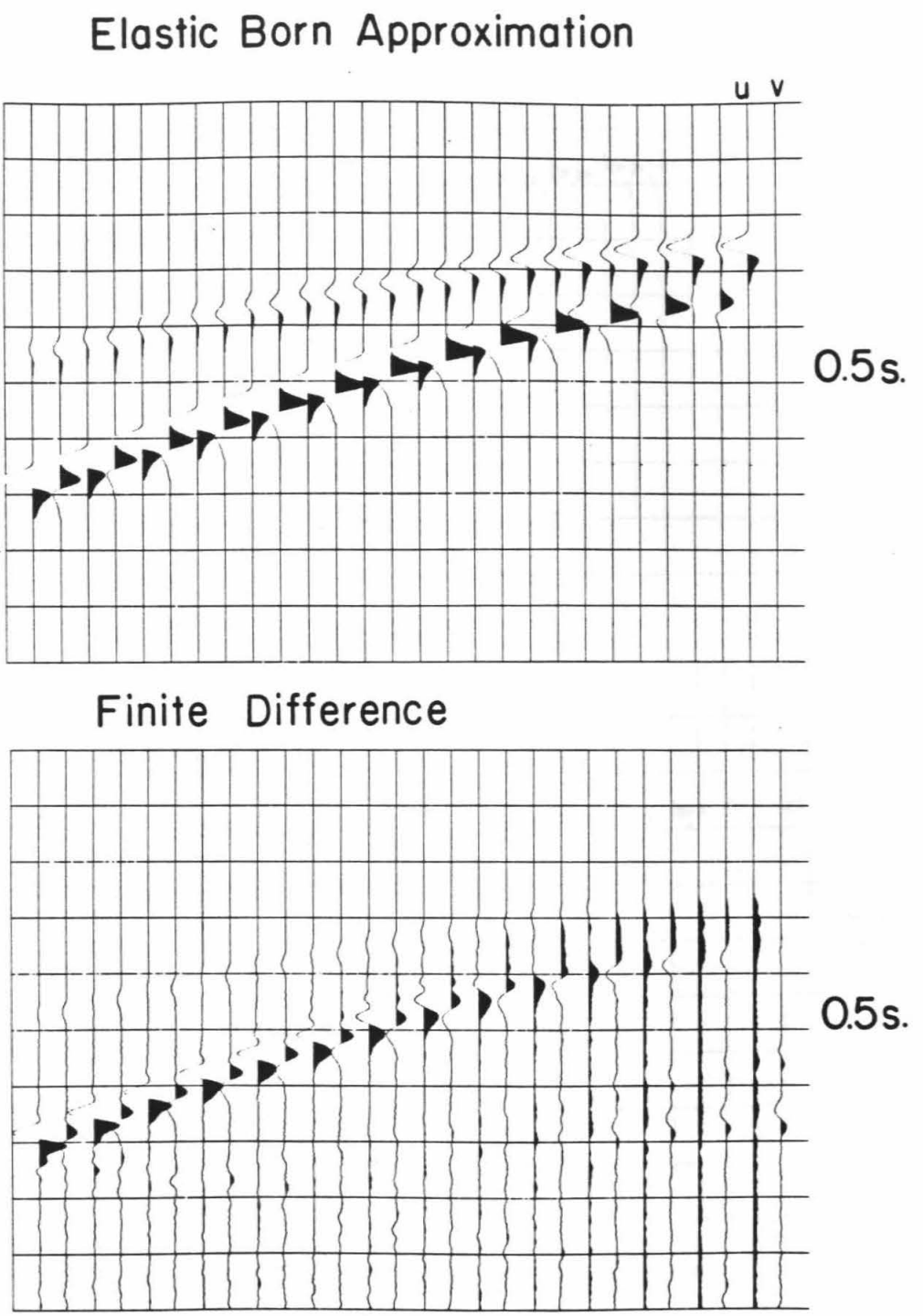

Figure 4.3: Comparison between the Born approximation displacements and a finite difference calculation for a density, ρ scatterer. u is the radial displacement and v the vertical displacement. The geometry is shown on Figure 4.2.

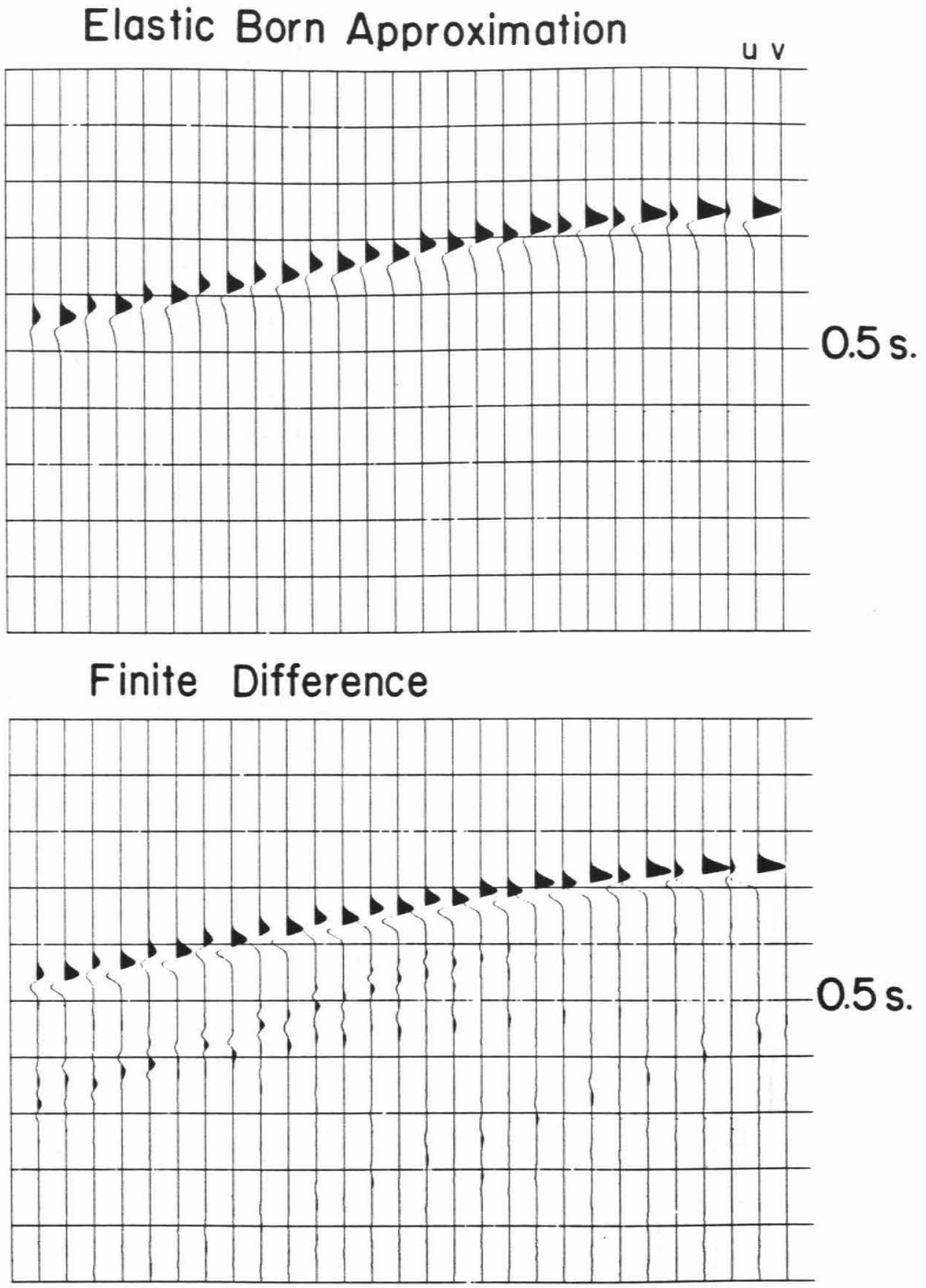

Figure 4.4: Same as Figure 4.3 for a $\gamma = \lambda + 2\mu$ scatterer.

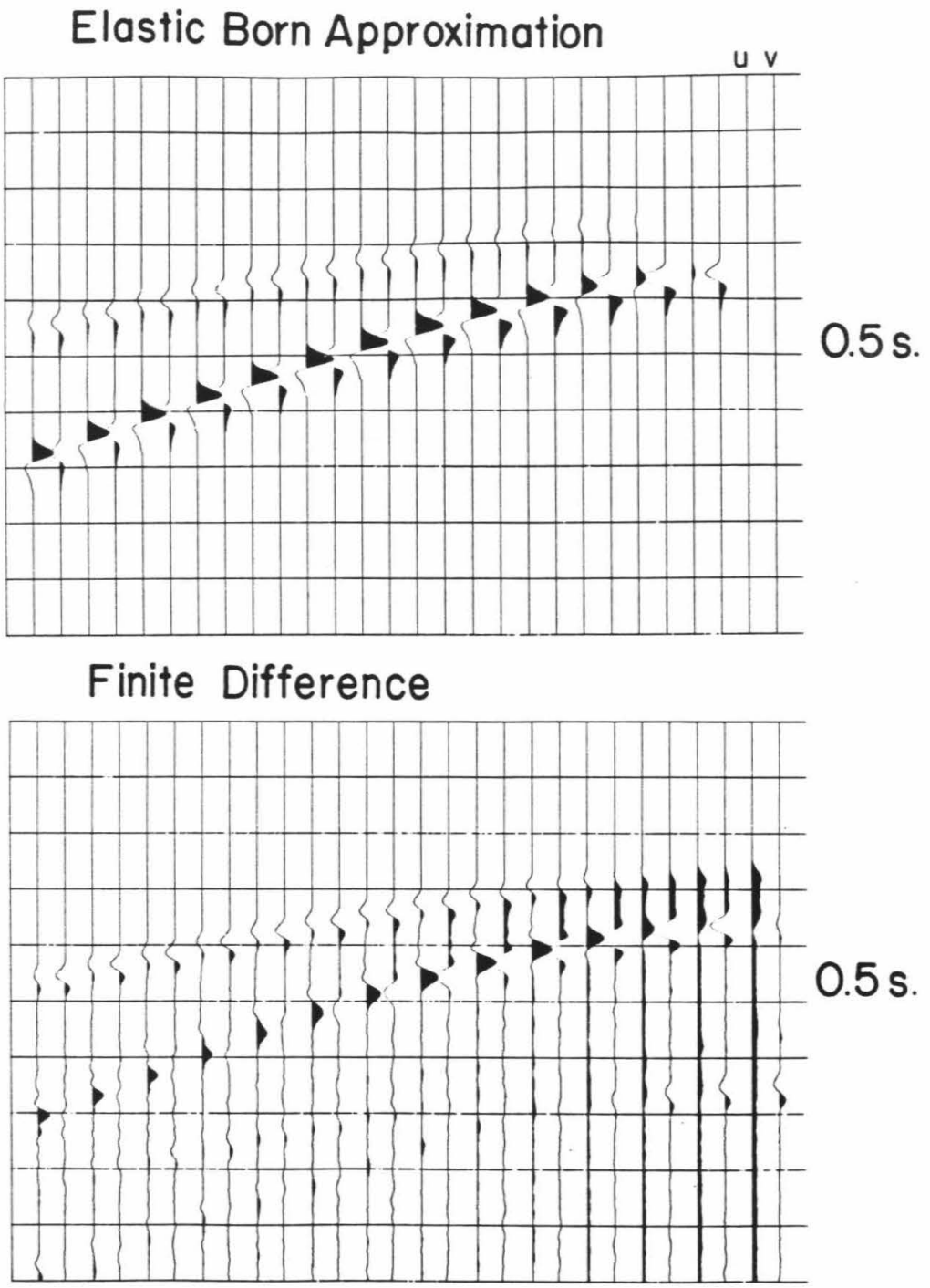

Figure 4.5: Same as Figure 4.3 for a shear modulus μ scatterer.

wavefront. Knopoff and Gilbert (1959) computed the radiation pattern for the first motion components of vertical displacement for all four types of waves mentioned. The first motion approximation is a high-frequency approximation and can be used at distances larger than a few wavelengths. Figure 4.6 illustrates the radiation patterns of the P wave and the regular S wave in polar diagrams. The pattern for the S wave beyond critical angle is in effect the magnitude of the singularity of the two-sided pulse at the time of arrival (see Knopoff and Gilbert, 1959 for further discussion). The expressions for the radiation patterns are given below :

For the P wave :

$$\phi_P(\theta) = \frac{\cos\theta\left[\frac{\alpha^2}{\beta^2} - 2\sin^2\theta\right]}{\left[\frac{\alpha^2}{\beta^2} - 2\sin^2\theta\right]^2 + 4\sin^2\theta\cos\theta\left[\frac{\alpha^2}{\beta^2} - \sin^2\theta\right]^{1/2}}.$$

For the regular S wave ($0 < \theta < \beta_{cr}$) :

$$\phi_S(\theta) = \frac{\cos\theta\sin\theta\left[\frac{\alpha^2}{\beta^2} - sin^2\theta\right]^{1/2}}{\left[1-2\sin^2\theta\right]^2 + 4\sin^2\theta\cos\theta\left[\frac{\beta^2}{\alpha^2} - \sin^2\theta\right]^{1/2}}.$$

For the irregular S wave ($\theta > \beta_{cr}$) :

$$\phi_S(\theta) = \sin\theta\cos\theta\left[\sin^2\theta - \frac{\beta^2}{\alpha^2}\right] \frac{4\sin^2\theta\cos\theta\left[\sin^2\theta - \frac{\beta^2}{\alpha^2}\right]^{1/2} - 2\left[1-2\sin^2\theta\right]}{\left(4\sin^2\theta\cos\theta\left[\sin^2\theta - \frac{\beta^2}{\alpha^2}\right]^{1/2}\right)^2 + \left[1-2\sin^2\theta\right]^4}.$$

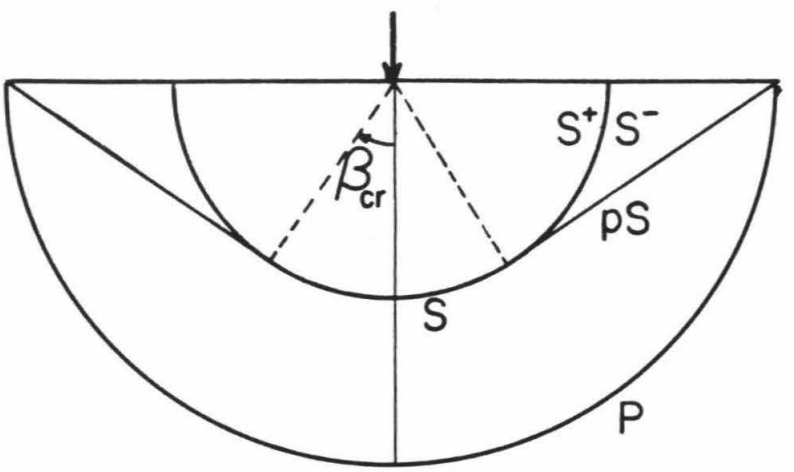

Wave pattern for a surface load

Figure 4.6: Waves generated by a vertical point force at the surface of a half-space. β_{cr} is the critical angle for the P to S reflection at the free surface.

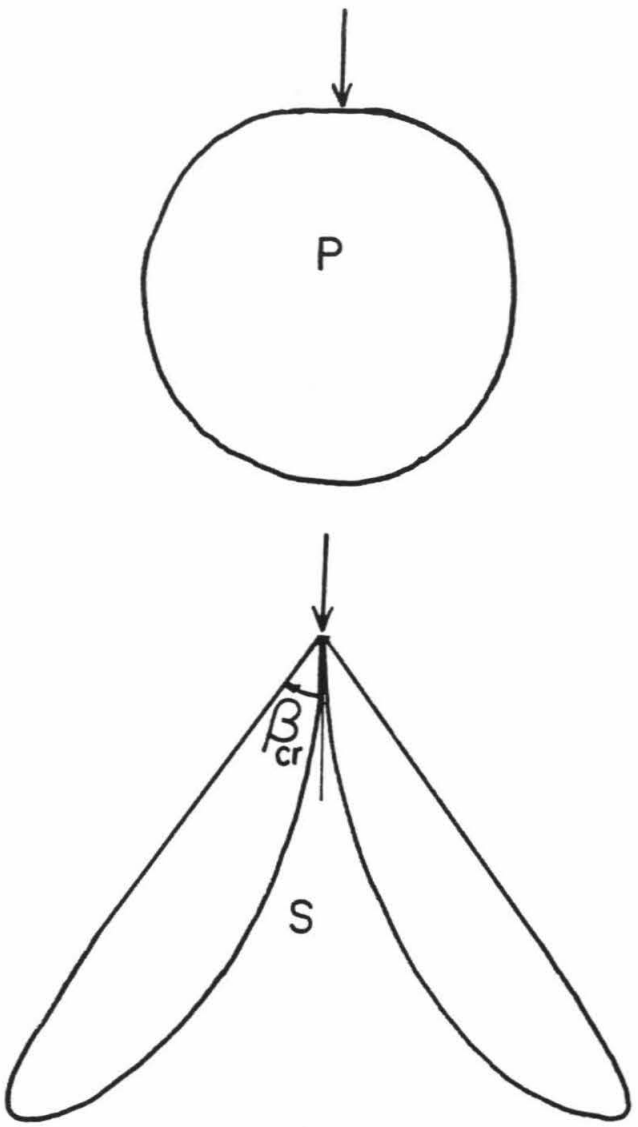

Figure 4.7: Radiation pattern for the P wave and regular S wave for a vertical point force at the surface of a half-space. β_{cr} is the critical angle for the P to S reflected wave at the free surface.

Inverse problem for the elastic wavefield

The same procedure that was used to invert the acoustic wavefield in the previous chapter can now be applied to the full elastic problem. The direct problem has been defined in the previous paragraph, where the expression for the two components of displacement (radial and vertical) were computed in the far-field using the linear relation:

$$\begin{bmatrix} u \\ v \end{bmatrix}(x_s, x_g, t) = \int_{\Omega} d\Omega \; M \begin{bmatrix} a_1 \\ a_2 \\ a_3 \end{bmatrix}(x, z). \tag{4.21}$$

M is the matrix representing the linear operator relating the medium parameters to the displacement vector.

Based on this linear relation between the medium parameters and the displacement vector, we can devise an inversion procedure similar to the one used for the acoustic problem. The general method is a Davidon-Fletcher-Powell method involving the transposed linear operator of the elastic Born approximation. This transposed operator can be written symbolically as:

$$\begin{bmatrix} a_1 \\ a_2 \\ a_3 \end{bmatrix}(x, z) = \int_{data} M^T \begin{bmatrix} u \\ v \end{bmatrix}(x_s, x_g, t)$$

where the sum over data corresponds to a summation using all the seismograms we dispose of.

In practice, each section (a_1, a_2, a_3) is computed by summing the crosscorrelation of the source function and the seismogram with the time delay corresponding to the travel time of the adequate set of incident and scattered ray (P-P, P-S, S-P, S-S) and

multiplying by the coefficients valid for these rays (including the geometrical amplitude decay, the angular scattering coefficient, the conversion from potential to displacement and the source radiation pattern.)

Conclusion

We expressed the scattered elastic field as a superposition of rays scattered from each point in the medium considered as an isolated elastic scatterer. The simplified picture was obtained after using three approximations on the scattered wavefield. The first approximation is the Born approximation that allows us to describe the scattered wavefield as the interaction of a background Green's function with a scattering potential, giving rise to a scattered wave approximated by $G_0 + G_0 V G_0$, where G_0 is the background medium Green's function and V is the scattering potential. The second approximation is a WKBJ approximation. It describes the propagation in the background medium under the assumption that the medium parameters are slowly varying. The third approximation is a far-field approximation on the propagation Green's function G_0. This leads to a ray-asymptotic description of the propagation part G_0. The elastic scattered field is then simply a superposition of scattered rays of different types (P-P, P-S, S-S, S-P) resulting from the interaction of direct P and S waves propagating in a background medium with each point of the medium considered as an isolated scatterer. The general approach that we take to invert the data described using such a model is the same as the one used in the acoustic case in Chapter 3. In the case of elastic waves, however, the backprojections involve the four types of scattered waves.

Chapter 5

Application of Iterative Backprojections to a Vertical Seismic Profile Data Set

Abstract

A three-offset VSP data set recorded in two wells is processed in order to invert for the local P-wave impedance structure, using a backprojection method. The data are reduced to a set of six sections representing the upgoing part of the vertical component of displacement. The method proved useful in resolving the lateral extent of a reservoir layer recognized on the well logs. With more numerous offsets, and the use of the converted waves, it is expected that this kind of method would also allow a determination of the nature of the reflectors.

Introduction

A set of three components offset-VSP data was obtained from ARCO Oil and Gas company. The data are from their test site at Holt Sands, Texas. There is good control over the amplitudes (essential for an inversion study). The setup of the experiment in boreholes allows for a large signal-over-noise ratio. The control over the average background velocity and density model is very good since we disposed of sonic and density logs. The source is an impactor at the surface and is well controlled

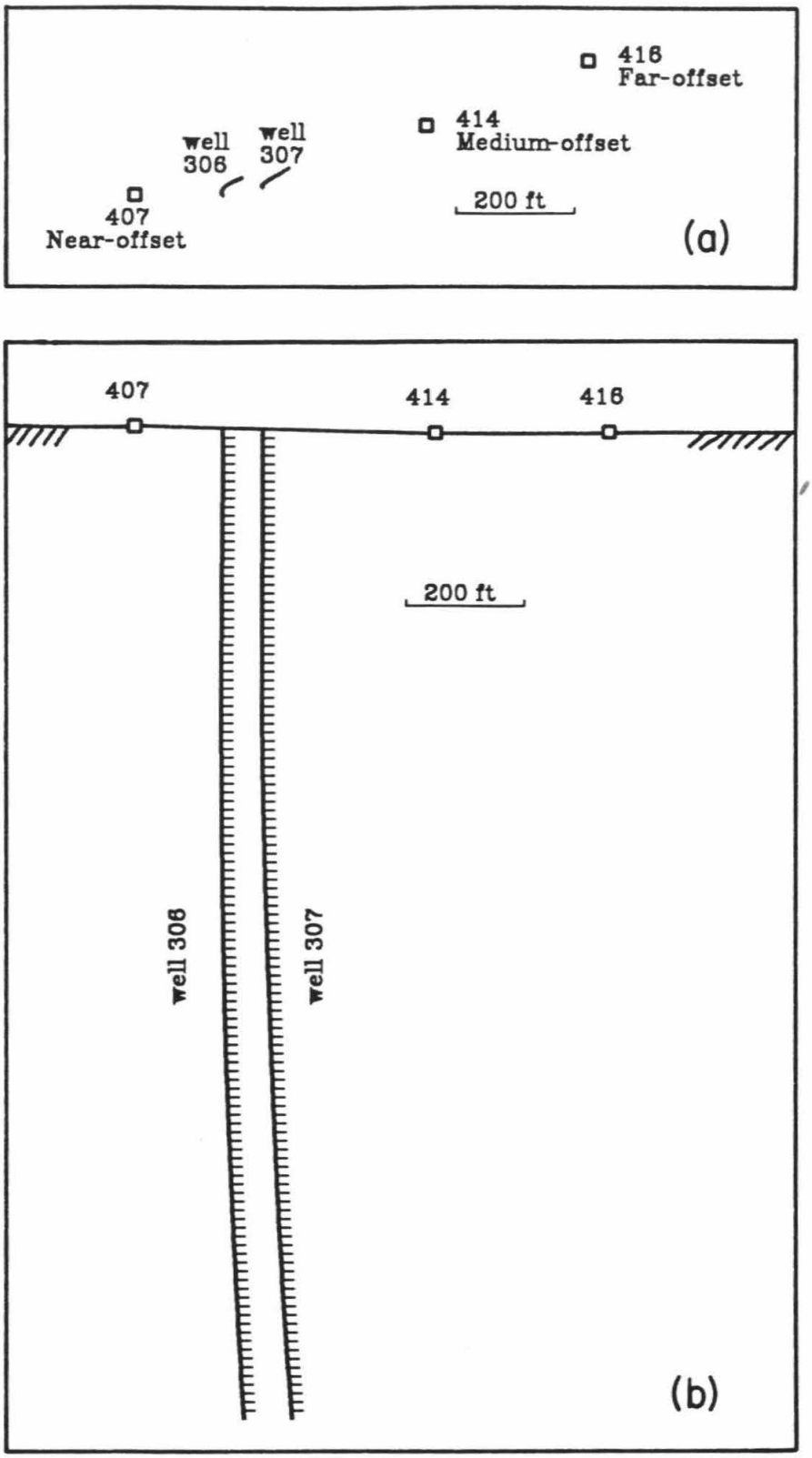

Figure 5.1: Location of the three shot points (407, 414, 416) and the two wells (306, 307) used in the VSP experiment. (a) is a map view . (b) is a section.

by a monitor instrument. The source and receiver are both essentially punctual so that no amplitude distortions are introduced by source or receiver arrays. The experiment was conducted in parallel in two wells for three different surface offsets. Figure 5.1 shows a cross section and a map of the experimental setup, with the well positions and shot positions.

The experiment was conducted by pulling up the instrument from the larger depth of approximately 1700 feet in both wells simultaneously. At each depth and for each offset, five impacts were shot. The digitization interval was 0.0005 seconds and the depth interval 15 feet.

Data reduction and backprojections

Preprocessing of the data consisted in removing the 60 Hz noise and its harmonics (120, 180, 240 and 300 Hz) using a notch filter. Each trace was then aligned in absolute time using the vertical component from a monitor instrument which was kept at the same position during the length of the experiment. The seismograms were stacked five by five giving a single trace at each depth. A seismogram was eliminated from the stack if its power was beyond 20 percent of the median value of the power for the five traces corresponding to one depth.

Since the source locations were different for the three offsets, and furthermore within individual offset, the position was slightly changed (a few feet, negligible compared to the dominant wavelength of about 150 ft); the waveforms changed for the different shot positions. To take this into account, the data were shape-filtered. This was done by spectral division of the data trace by the monitor trace in the case of the vertical components of the near-offset data. Figure 5.2 shows the section for well 307

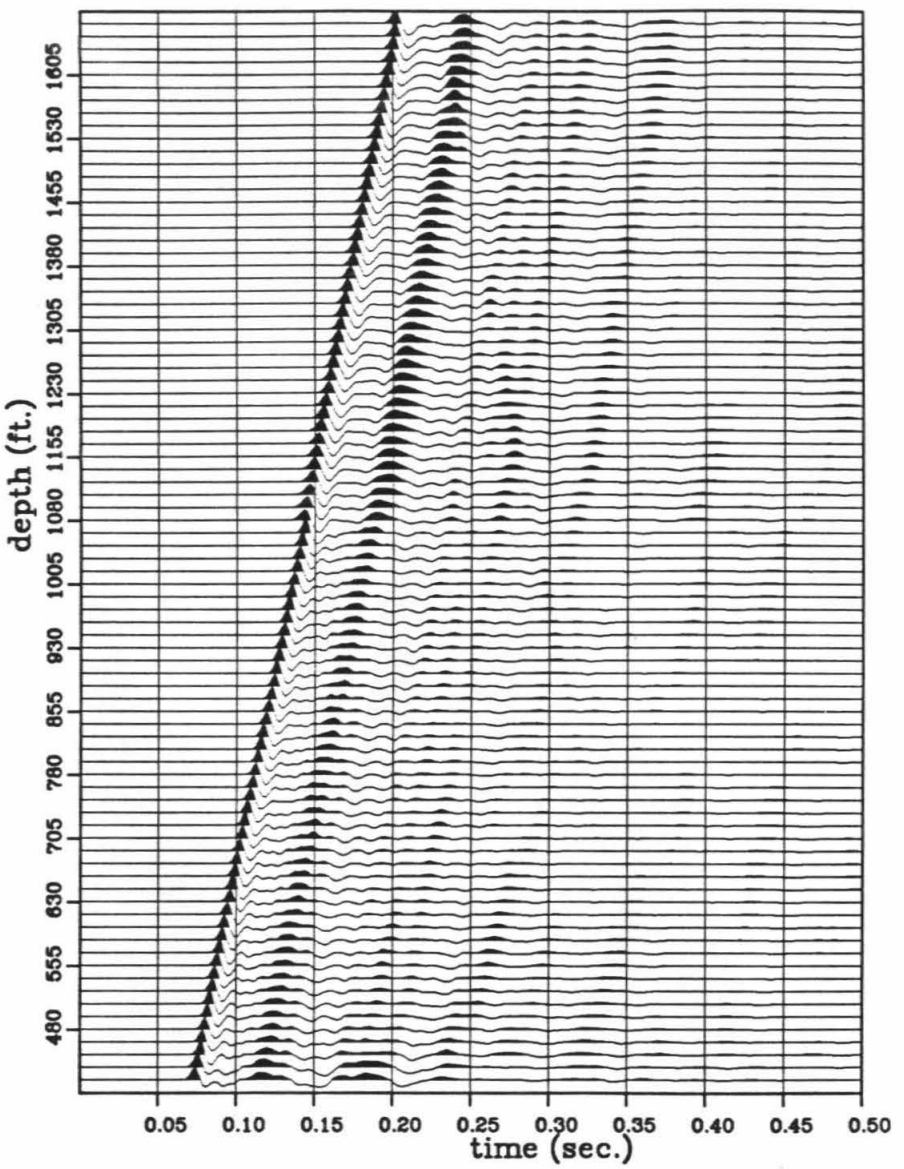

Figure 5.2: Section for well 307, near-offset after filtering of 60 Hz noise, and stacking. Trace equalized.

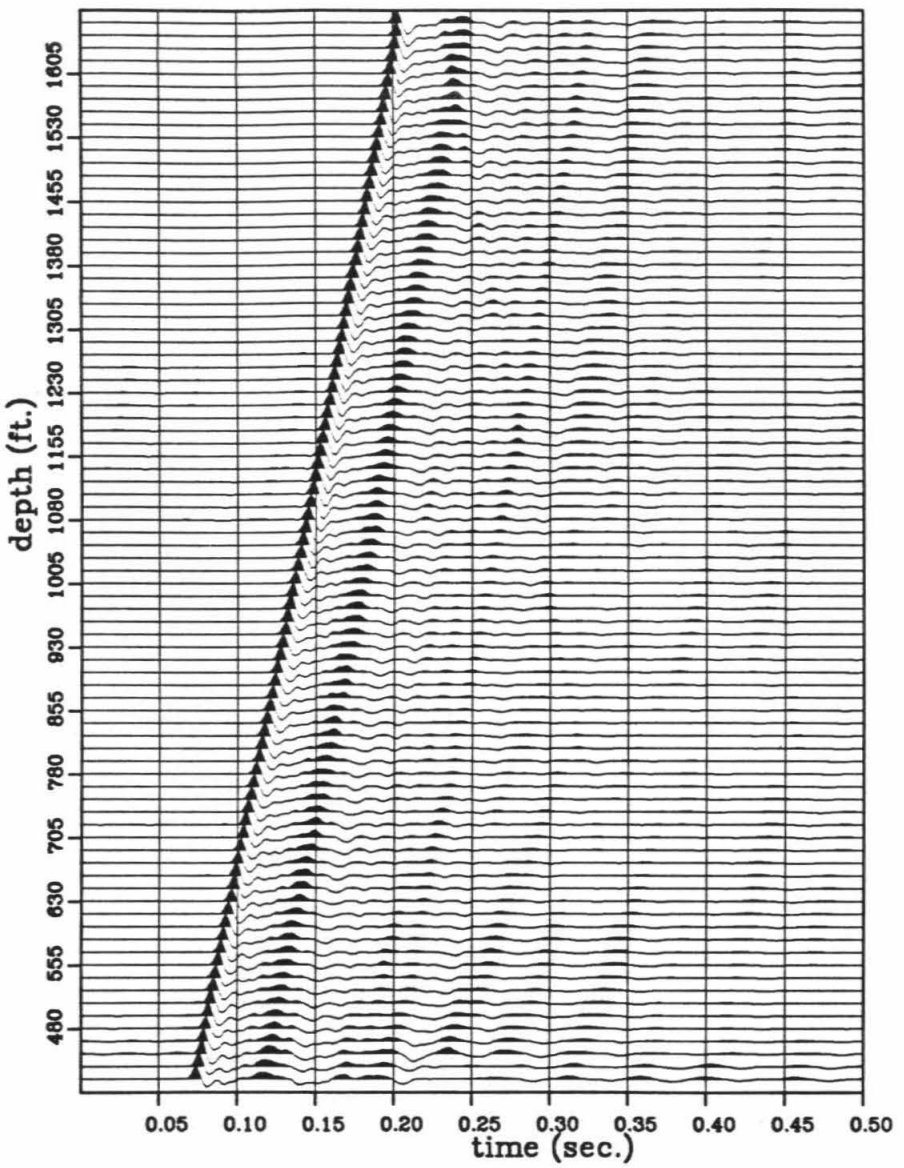

Figure 5.3: Section for well 307, near-offset after shapefiltering. Compare with section on Figure 5.2 before filtering. Trace equalized.

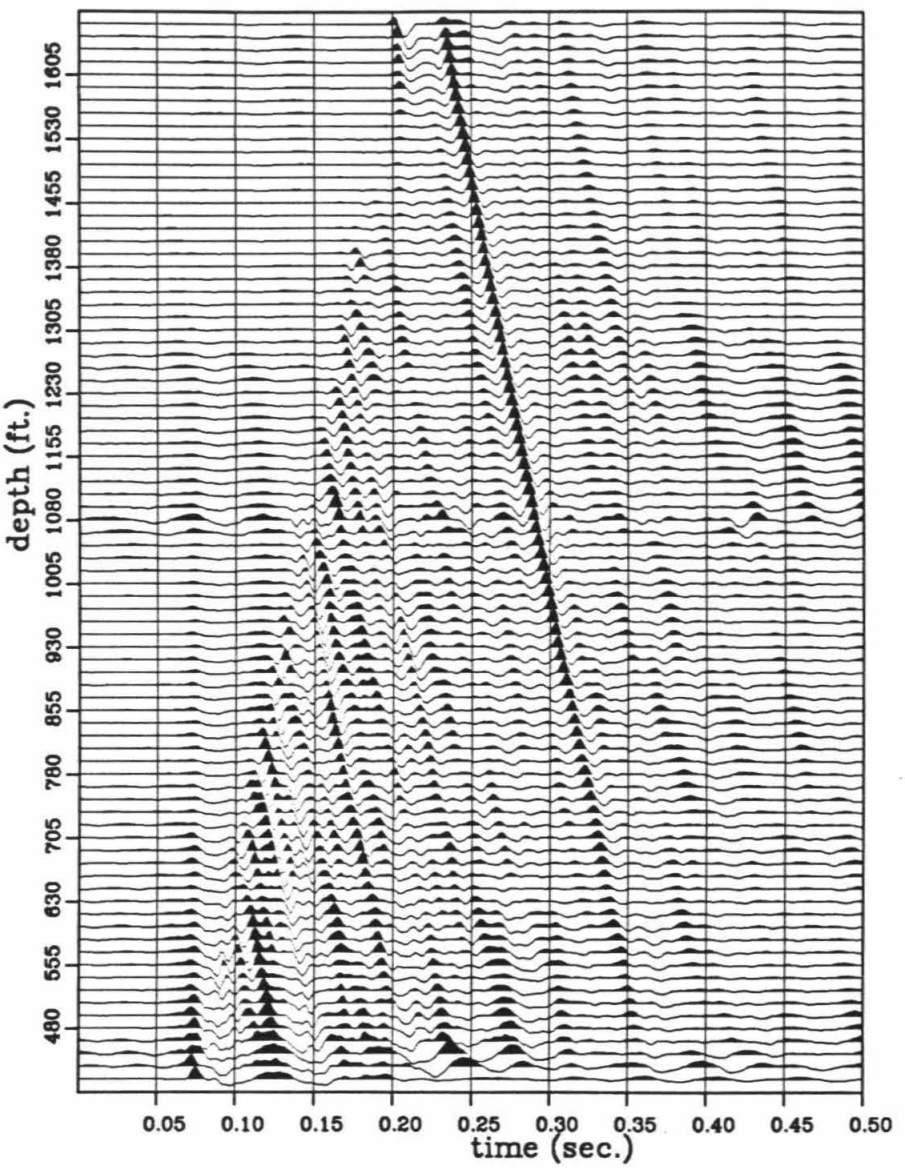

Figure 5.4: Section for well 307, near-offset after F-K filtering. The filter eliminated the downgoing waves. Note the presence of an artifact (equal time line) at the top of the section between 0.05 and 0.10 s.

(near-offset source) after notch filtering and stacking. Figure 5.3 shows the same section after shape filtering. This procedure allows us to take care of any eventual fluctuation in the absolute amplitude of the source strength and variation in waveform. For the medium-offset and far-offset data, the amplitude of the monitor was used to scale the data; however, the waveform was not used since it was very different from the data waveform. Instead, the waveform used in the spectral division for the shaper filter was obtained by stacking the data waveform to get an average wavelet. The reference waveform was obtained from the near-offset monitor vertical component so as to simulate a uniform wavelet for all the experiments. Since we want to use the scattered part of the data, we have to isolate it from the direct wavefield. This is difficult to do for the forward-scattered part of the scattered field, since it involves subtracting an estimate of the direct waves from the total field, and this is very model dependent. However, the backscattered part of the wavefield can be removed by filtering the upgoing wave from the data. This filtering is done in the F-K domain. Two of the quadrants of the F-K transform are zeroed out (corresponding to $\frac{\omega}{k}>0$.). This is illustrated by Figure 5.4 showing the section at well 307 for the near-offset after upgoing wave filtering. This can be compared to Figure 5.3 showing the whole recorded wavefield, including downgoing and upgoing waves. There is an artifact introduced by this filtering in the form of the constant time line for the shallowest depth (bottom of section on the figure). This is due to the cut-off in depth which makes the direct arrival look as a point including negative and positive components of time dip. Figures 5.5, 5.6, 5.7, 5.8, 5.9 and 5.10 present the final sections of vertical components of the upgoing waves for the three offsets. The near-offset sections show mainly reflected P waves, according to their moveout. The medium-offset

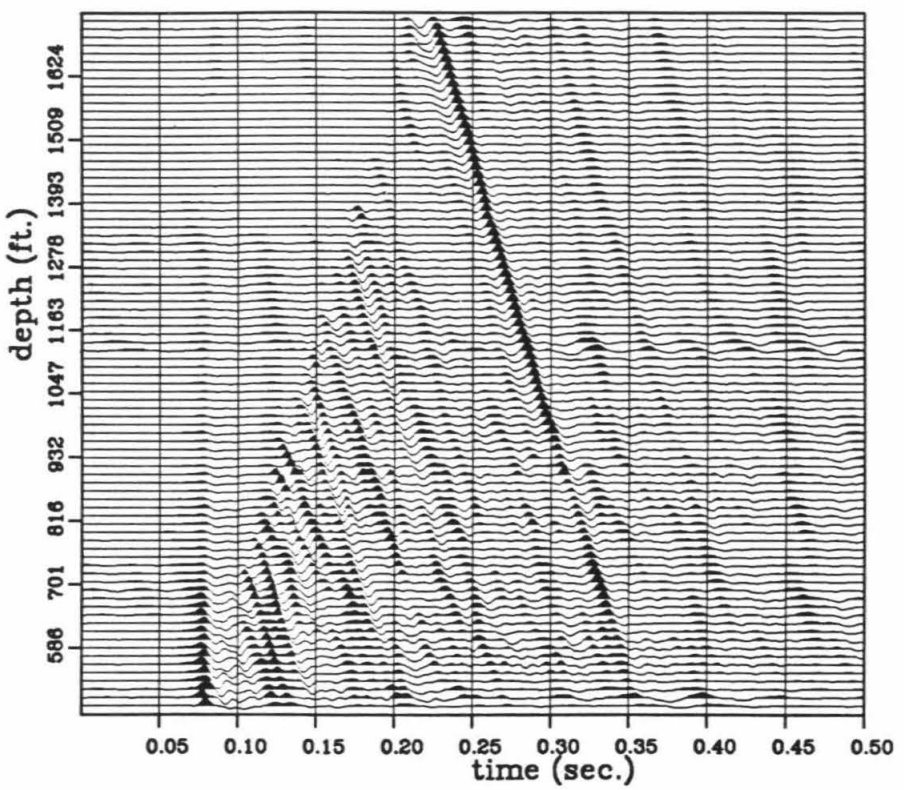

Figure 5.5: Near-offset section of vertical components for well 306 after notch filtering, shape filtering and upgoing wave separation. Each trace is scaled individually.

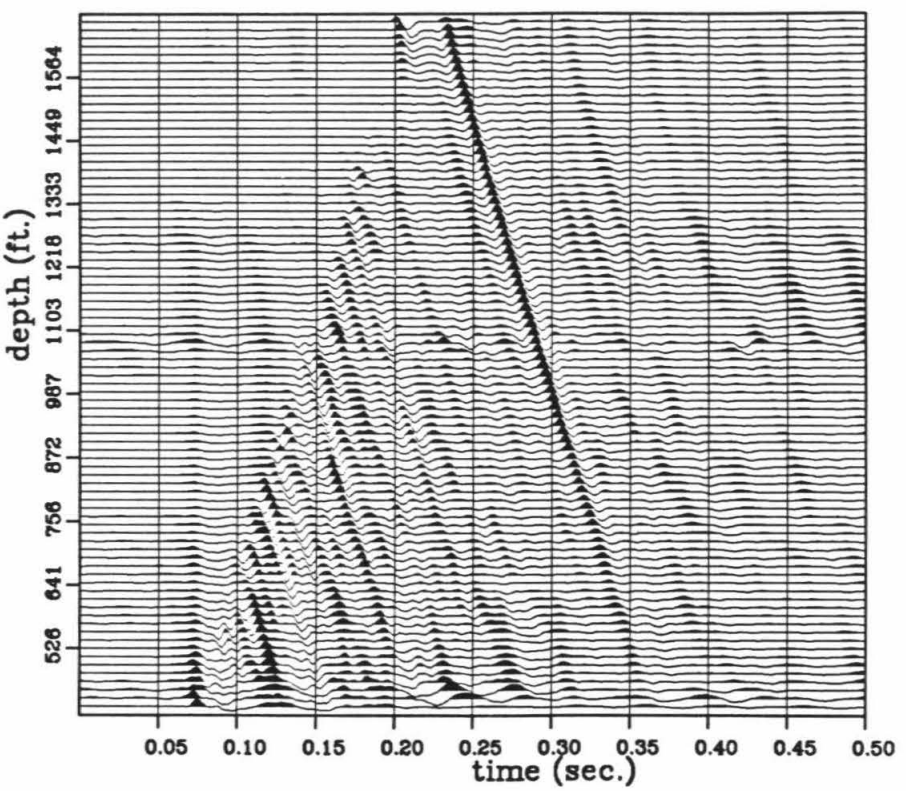

Figure 5.6: Same as Figure 5.5 for well 307.

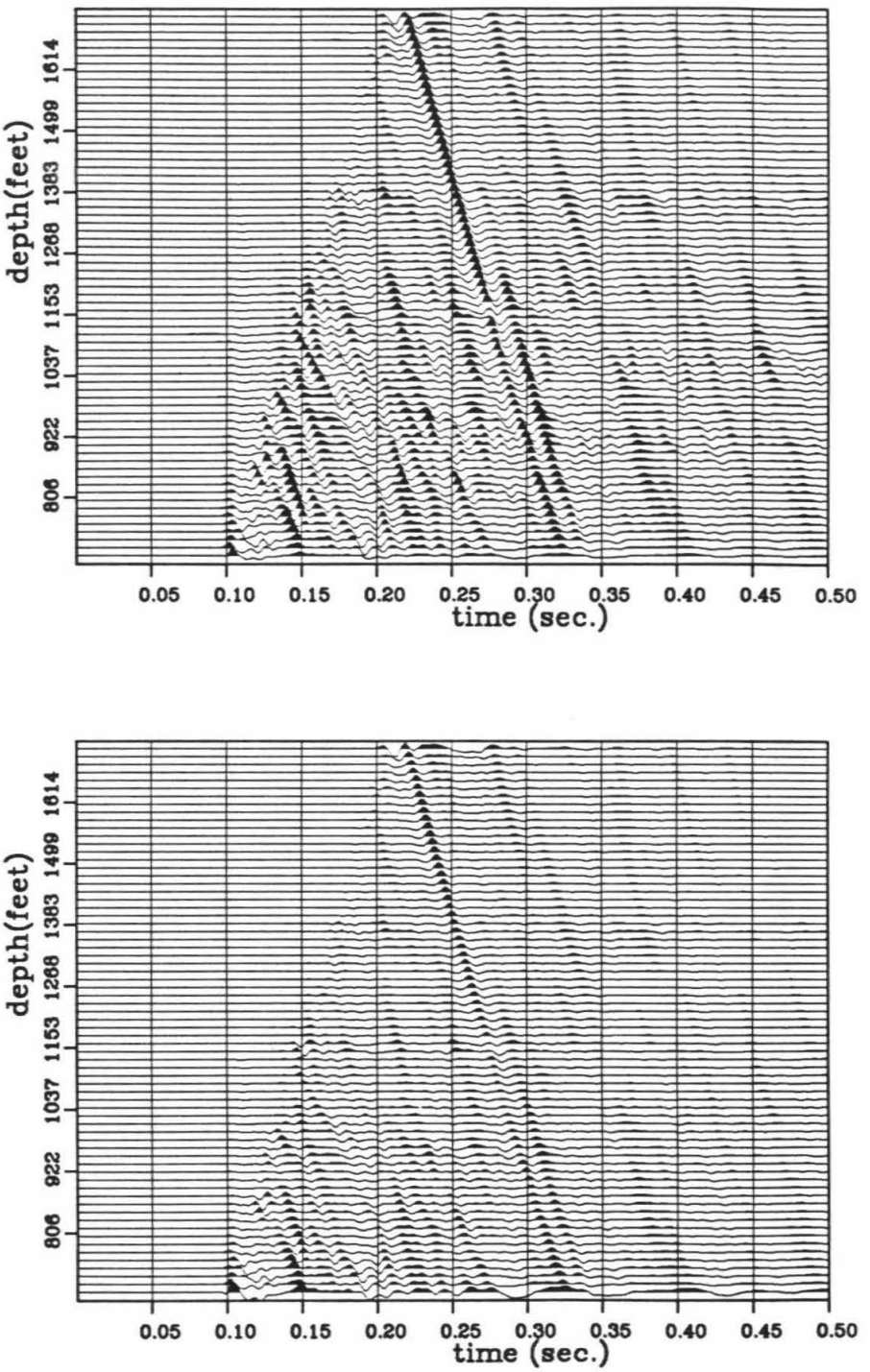

Figure 5.7: Medium-offset section of vertical components for well 306 after notch filtering, shape filtering and upgoing wave separation. The top section traces are scaled individually. The bottom section has the same scale for all traces.

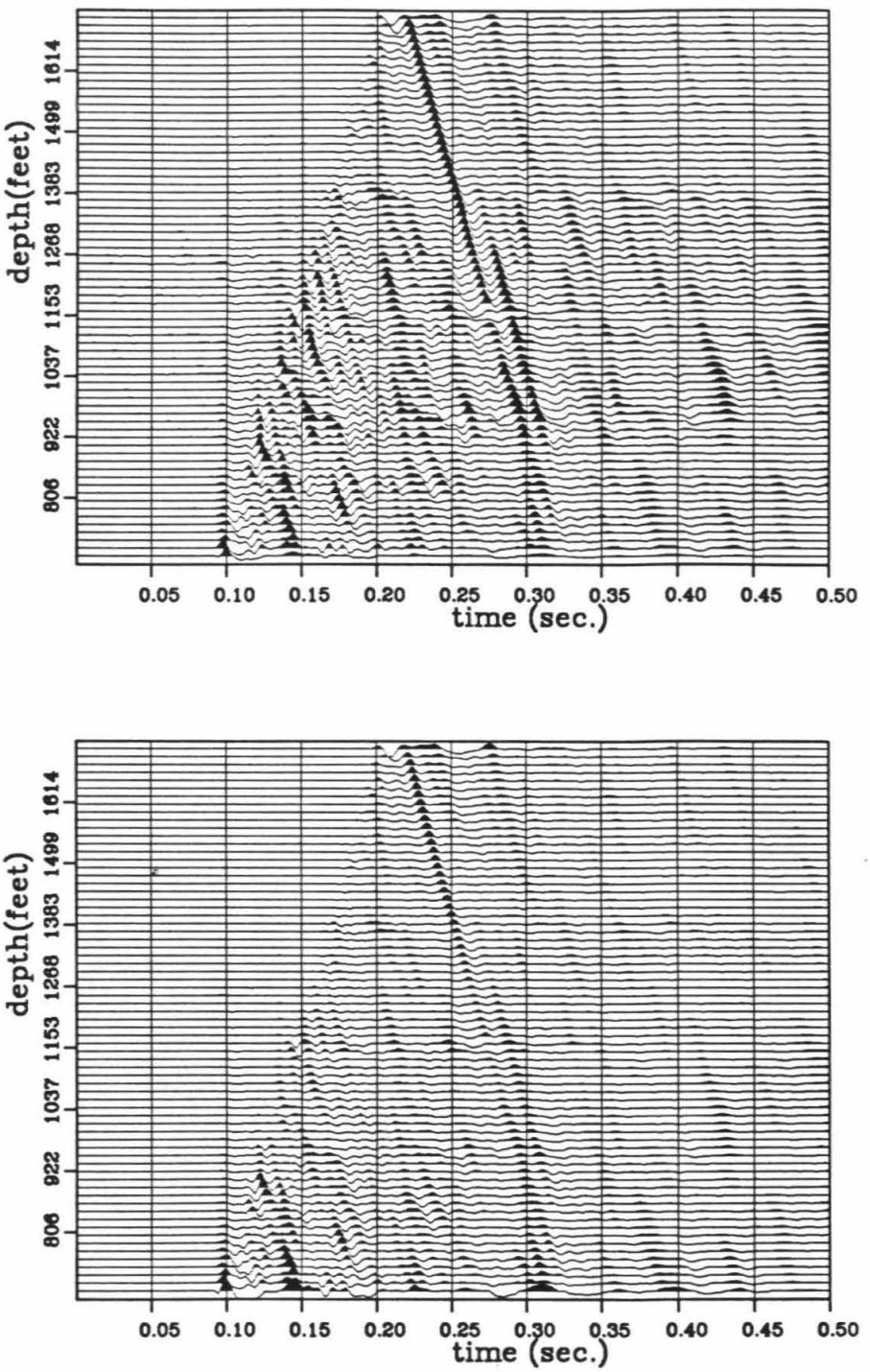

Figure 5.8: Same as Figure 5.7 for well 307.

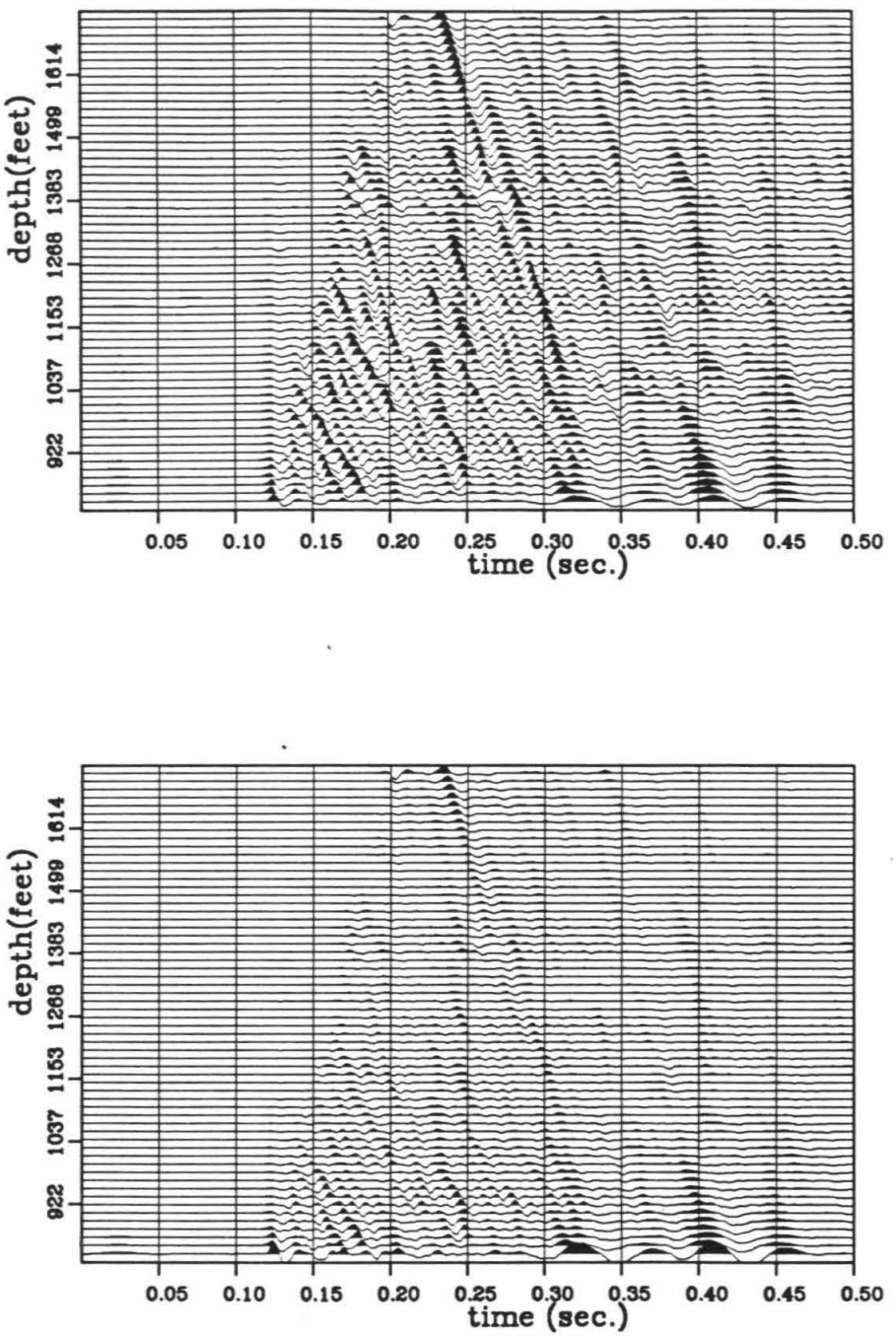

Figure 5.9: Far-offset section of vertical components for well 306 after notch filtering, shape filtering and upgoing wave separation. The top section traces are scaled individually. The bottom section has the same scale for all traces. Note the presence of large converted P to S waves.

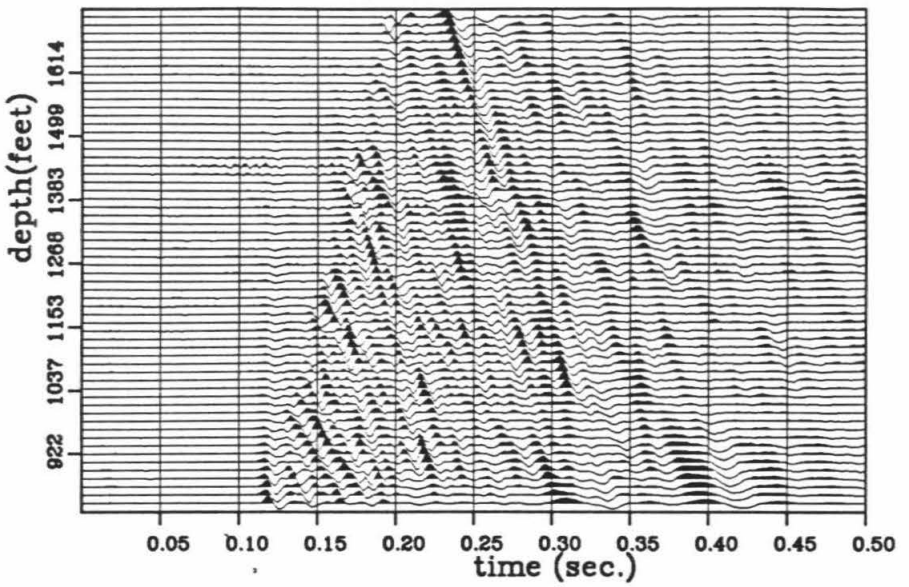

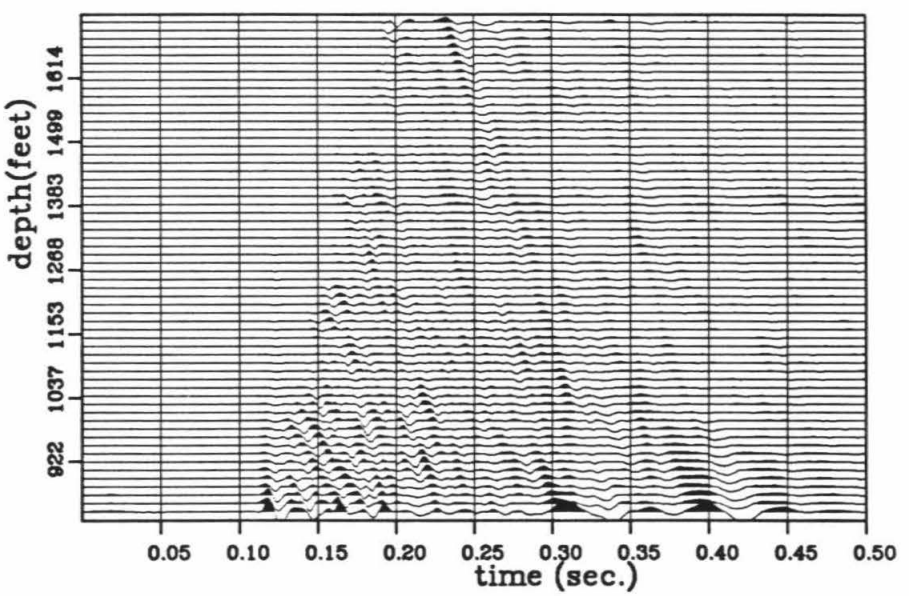

Figure 5.10: Same as Figure 5.9 for well 307.

and far-offset also show some converted waves, especially the far-offset, where a substantial part of the energy is in the P to S converted waves.

The three offset experiments were conducted at different sites and there might be fluctuations in the source strength for these different offsets. To account for this, we compared the amplitude decay with the depth of the vertical components of the direct compressional waves against a simple model consisting in a constant velocity and no anelastic attenuation. This model predicts an amplitude variation due to geometrical spreading and source pattern for the vertical component of the displacement field as $\frac{A\cos^2\theta}{R}$, where A is a constant, θ, the angle between the incident ray and the vertical. One of the $\cos\theta$ factors comes from the source radiation pattern (approximation for a vertical point force), and the other from the projection of the compressional motion on the vertical direction. R is the geometrical decay expected in a whole space for constant velocity. Figures 5.11, 5.12 and 5.13 show a least-squares fit of the function $\frac{A\cos^2\theta}{R}$ to the amplitude variation with the depth of the downgoing wave. The misfit is systematically in the same way, with the actual amplitudes decaying more rapidly than predicted by the model. This is probably mostly due to the loss of energy to anelastic attenuation and transmission. The misfit for the far-offset sections might be in part explained by a discrepancy between the model of constant velocity and the actual model which presents an increase with depth. From this fit, we deduce the coefficients necessary to calibrate the amplitudes of the sections for the three different offsets.

One of the limitations of the Born-backprojection methods that have been developed in this thesis is that they rely on several approximations on the wavefield.

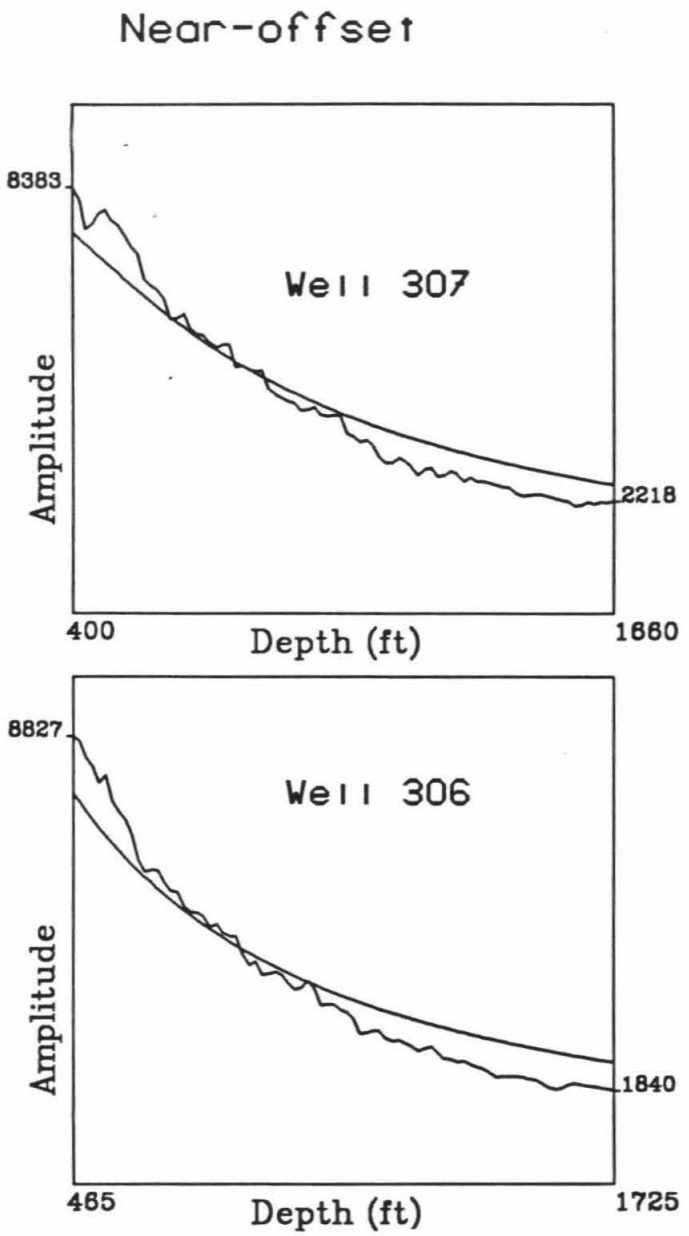

Figure 5.11: Fit of $\frac{A\cos^2\theta}{R}$ to the amplitude variation with depth of the direct arrival for the near-offset sections of wells 306 and 307.

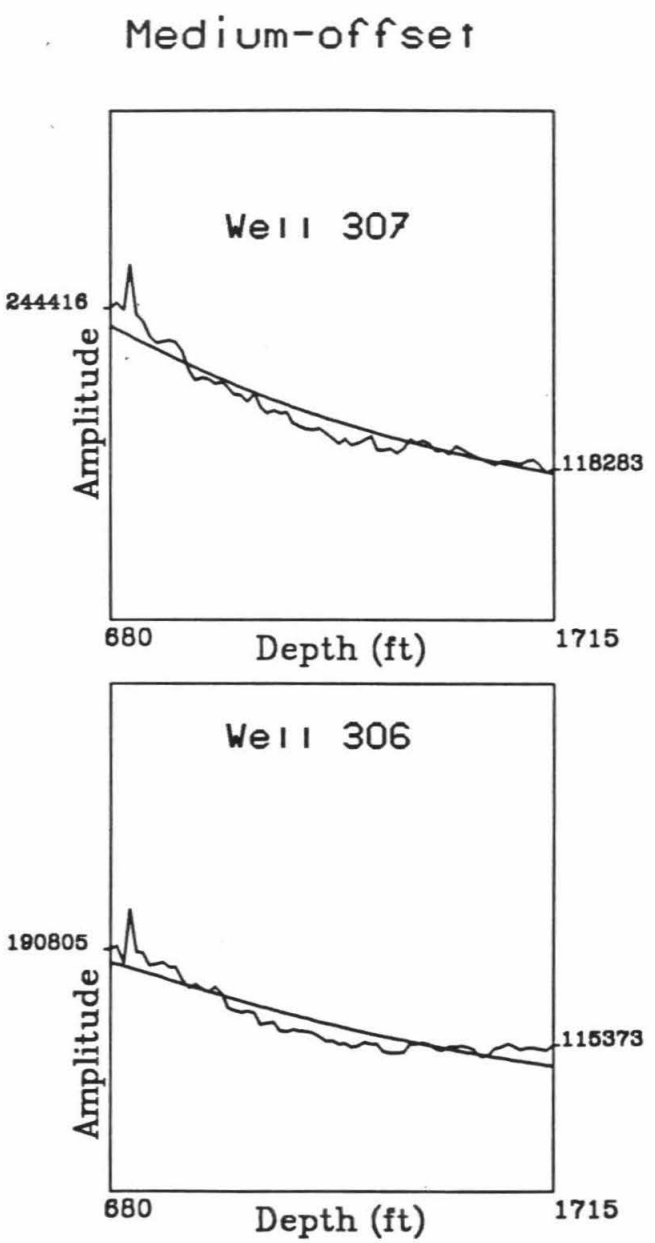

Figure 5.12: Same as Figure 5.11 for the medium-offset sections.

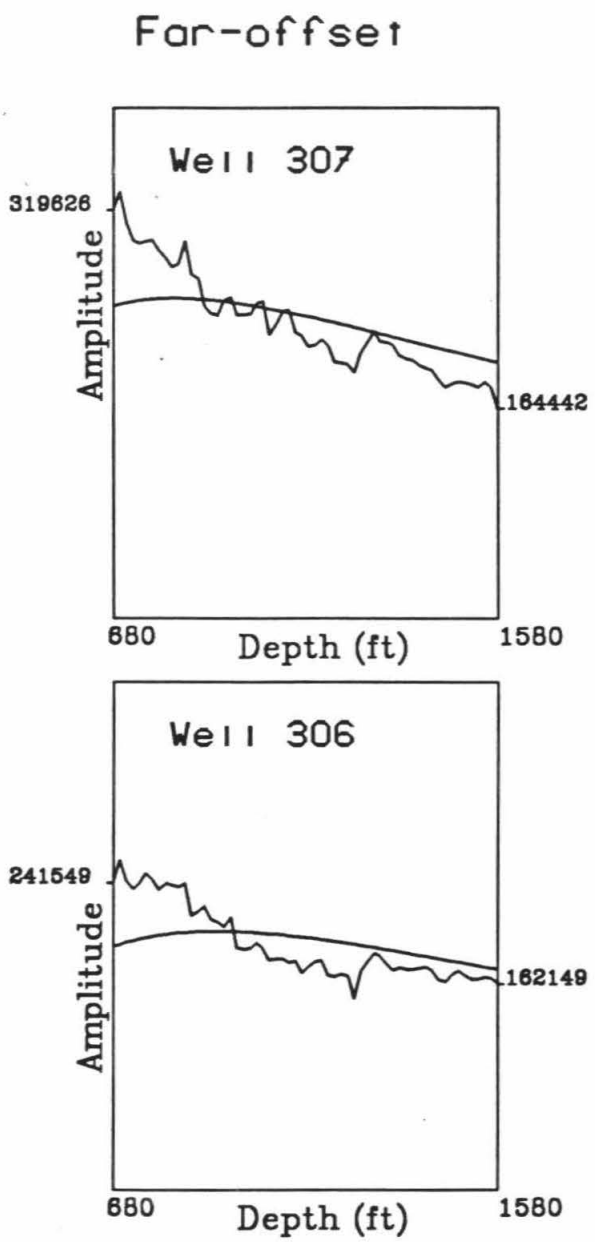

Figure 5.13: Same as Figure 5.11 for the far-offset sections.

The parts of the subsurface to be imaged have to be at least a few wavelengths away from the receiver as well as the source. This comes from the introduction of the Born approximation which considers each point of the medium as a source, and therefore an irregularity. In the VSP geometry, this means that the area directly surrounding the receiver is not appropriate for a reconstruction using the Born approximation. We reconstructed a part of the subsurface below a depth of 600 ft using the receivers situated above that depth, for all three offsets. Figure 5.14 shows the first iteration for the inversion of impedance. We chose to invert for impedance, since the angular coverage on the section is not sufficient for a multiparameter inversion and the upgoing energy is mostly due to the impedance contrast because it presents a maximum in the backscattering direction. The backprojected section is placed at its actual location with respect to the wells.

One of the reasons for this VSP experiment is the observation of the presence of a reservoir layer on the sonic and density logs in well 306, between 1630 and 1670 feet. This layer is not observed on the logs for well 307. The question is to know whether or not a reflection can be obtained from the VSP experiment, and if it can, what happens to it between the two wells. From the near-field data, there appears to be a reflection on the section from well 306 corresponding to a reflector at about the right depth for it to be interpreted as the reservoir. This reflection is not observed on the near-offset section for well 307. Figure 5.15 shows the comparison of the two sections at depths between 1725 and 1425 feet and times between 0.15 and 0.3 second. The arrow indicates the reflection that we attribute to the reservoir. Note the absence of a corresponding reflection on the 307 section. Figure 5.15 also shows simple backprojections of the individual sections and the reconstructed reservoir reflection. The

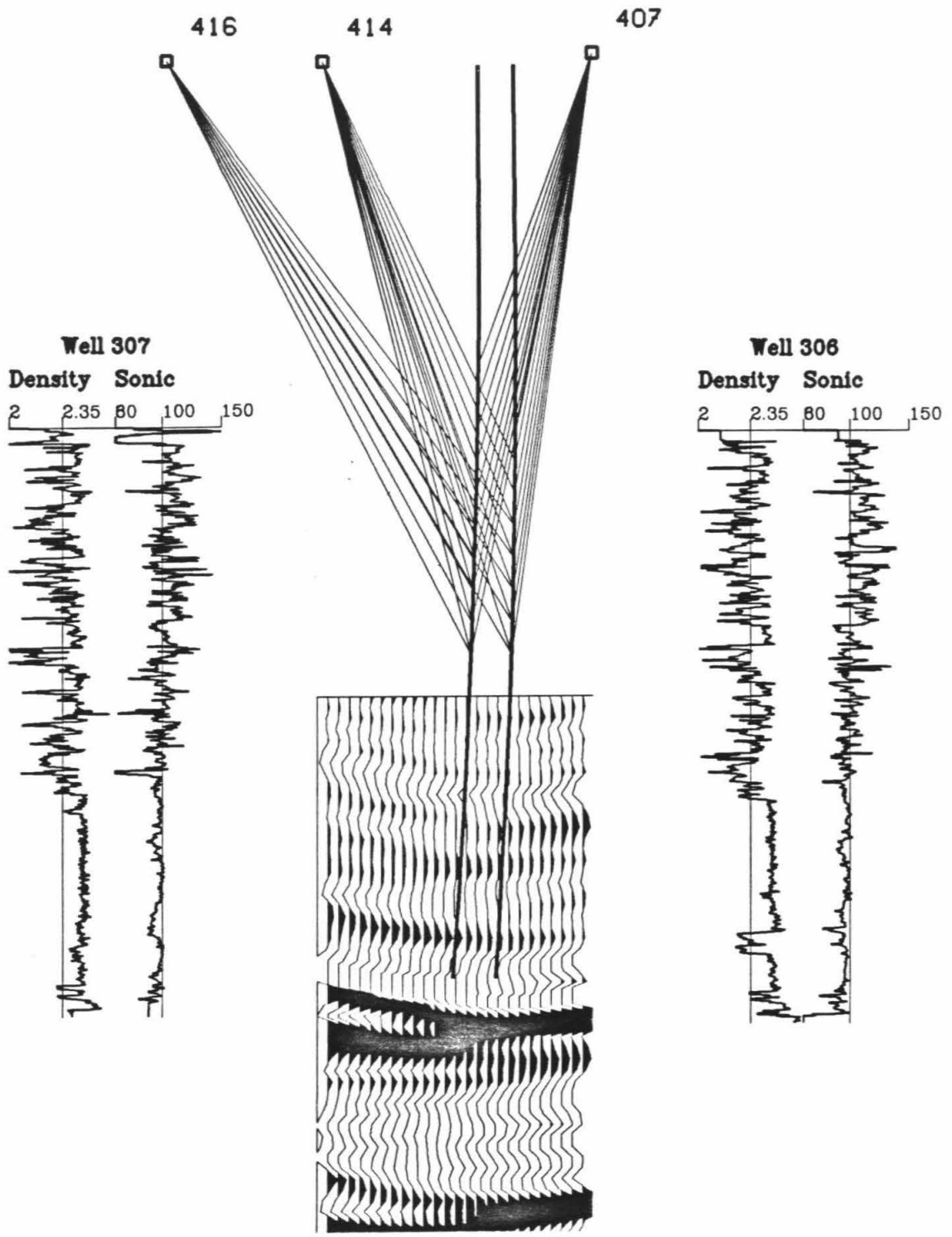

Figure 5.14: First iteration of the Born-elastic inversion for P-wave impedance. The two thick lines represent the wells. The lighter lines are the ray paths between the sources and the receivers used in the inversion. The section imaged is positioned with respect to the wells and sources.

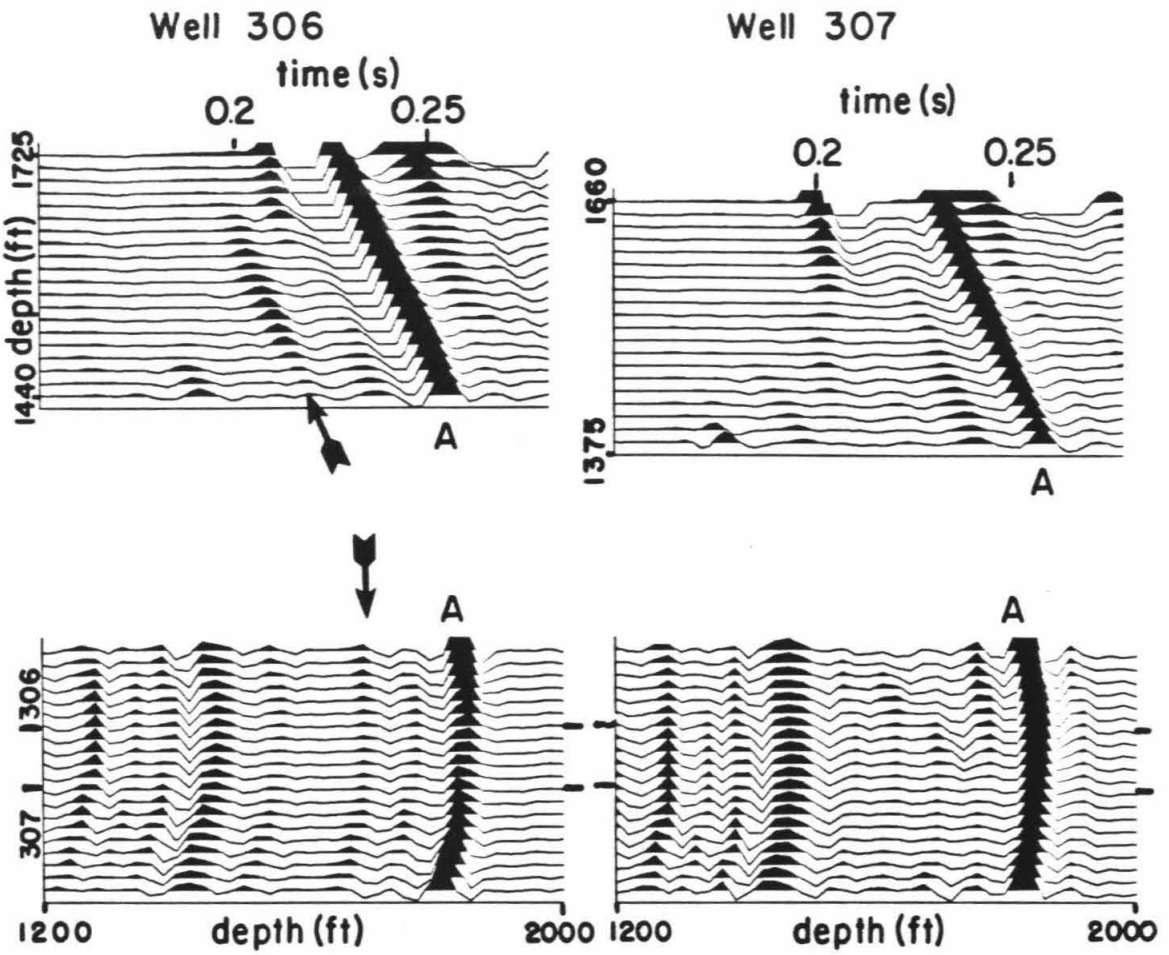

Figure 5.15: The top two sections are the time-depth near-offset sections for wells 306 and 307 (portions of the sections shown on Figure 5.5 and 5.6). The arrow points to the reflection which arises from the reservoir layer. The letter A indicates the position of the very prominent reflector seen on Figures 5.5 to 5.10. The bottom sections are the single-offset back-projections for the time-depth sections of the top of the figure. The arrow shows the position of the imaged reflector. Note its discontinuity on the backprojection from well 307. The short segments on the top and bottom of the bottom figures indicate the positions of wells 306 and 307.

backprojections were performed with no weighing for the angular dependence or the geometric decay, in order to use all of the data in the sections, including the lower depths. The backprojection for section 306 shows a continuous reflector marked by the arrow, directly above the very prominent reflector marked A. The backprojection for section 307 shows the same reflector to be discontinuous, the discontinuity being compatible with the absence of the reservoir on the logs for well 307. On Figure 5.14, which is the impedance inversion using only part of the data, the reflector at 1650 feet depth seems to pinch out towards well 307, giving us a possible explanation for the absence of the reservoir at well 307.

Conclusion

A data set consisting in seismograms recorded in two wells for three different offsets was processed in order to invert it for the P-wave impedance variations. It was shown that it is possible to process this good quality data in order to take advantage of the amplitude information it contains. Although the offset coverage is not sufficient to allow a determination of the reflector characteristics using the backprojection method developed in this thesis, it was shown that the geometry of a reservoir layer can be inferred from the comparison between the backprojections of the near-offset sections for the two wells.

References

Aki, K. and Richards, P., 1980, *Quantitative seismology - Theory and methods,* v.1 and 2, San Francisco, W.H. Freeman and Company.

Bleistein, N. and Cohen, J.K., 1982, The velocity inversion problem. Present status-New directions : *Geophysics,* v.47, pp.1497-1511.

Carrion, P.M. and Patton, W.A., 1983, Resolution and Reconstruction of Acoustic Impedance: *Jour. Geoph. Res.,* v.88, pp.10349-10358.

Clayton, R.W., 1981, Wavefield inversion methods for refraction and reflection data: Ph.D. thesis Stanford University, Stanford, 96 pp.

Clayton, R.W. and Stolt R., 1981, A Born-WKBJ inversion method for acoustic reflection data: *Geophysics,* v.46, pp.1559-1567.

Clayton, R.W. and R.P. Comer, 1985, Whole Earth tomography, submitted: *Jour. Geoph. Res.*

Fletcher, R., 1980, *Practical Methods of Optimization.* New York, John Wiley & Sons.

Gal'perin, E.I., 1974, Vertical seismic profiling: *Soc. of Expl. Geophys., Special Publication # 12*

Gardner, G.H., Gardner, L.W. and Gregory A.R., 1974, Formation velocity and density - the diagnosis basics for stratigraphic traps: *Geophysics,* v.39, pp.770-780.

Gassaway, G.S. and Richgels, H.J., 1983, SAMPLE: Seismic Amplitude Measurement for Primary Lithology Estimation: *Proceedings of the S.E.G. 53 Annual international Meeting,* pp.610-613.

Hearn, T.M., 1985, Crustal structure in southern California from array data: Ph.D. thesis, California Institute of Technology, Pasadena , 130 pp.

Humphreys, G., Clayton, R.W. and Hager, B.H., 1984, A tomographic image of Mantle structure beneath Southern California: *Geophs. Res. Lett.,* v.11, pp.625-627.

Jain, S. and Wren, A.E., 1980, Migration before stack-Procedure and significance : *Geophysics,*v.45, pp.204-212.

Kennet, B.L.N., 1979, Theoretical Reflection Seismograms for Elastic Media: *Geophysical Prospecting,*v.27, pp.301-321.

Knopoff, L. and Gilbert, F., 1959, First Motion Methods in Theoretical Seismology: *The Journal of the Acoustical Society of America,* v.31, pp.1161-1168.

Miklowitz, J., 1978, *Elastic waves and waveguides,* Amsterdam, North-Holland Publishing Company.

Morse, P.M. and Feshbach, H., 1953, *Methods of Theoretical Physics,* New-York, McGraw-Hill Book Company.

Nercessian, A., Hirn, A. and Tarantola, A., 1984, Three-dimensional seismic transmission prospecting of the Mont Dore volcano, France: *Geophys. J. R. astr. Soc.,* v.76, pp.307-315.

Oldenburg, D.W., Scheuer, T. and Levy, S., 1983, Recovery of the acoustic impedance from reflection seismograms: *Geophysics,* v.48, pp.1318-1337.

Ostrander, W.J., 1984, Plane-wave reflection coefficients for gas sands at nonnormal angles of incidence: *Geophysics,* v.49, pp.1637-1648.

Rao, S.S., 1977, *Optimization. Theory and Applications.* New York, John Wiley & Sons.

Raz, S., 1981, Three-dimensional velocity profile inversion from finite-offset scattering data: *Geophysics,* v.46, pp.837-842.

Schiff, L.I., 1968, *Quantum Mechanics,* New York, McGraw- Hill Book Company.

Stolt R., 1978, Migration by Fourier Transform: *Geophysics,* v.43, pp.23-48.

Tanimoto, T., 1984a, A simple derivation of the formula to calculate synthetic long-period seismograms in a heterogeneous Earth by normal mode summation: *Geophys. J. R. astr. Soc.,*v.77, pp.225-278.

Tanimoto, T., 1984b, Waveform inversion of mantle Love waves : the Born seismogram approach:*Geophys. J. R. astr. Soc.,*v.78, pp.641-660.

Tarantola, A., 1984a, Linearized inversion of seismic reflection data: *Geophysical Prospecting,*v.32, pp.998-1015.

Tarantola, A., 1984b, Inversion of seismic reflection data in the acoustic approximation: *Geophysics,* v.49, pp.1259-1266.

Tarantola, A. and Nercessian, A., 1984, Three-dimensional inversion without blocks:*Geophys. J. R. astr. Soc.,*v.76, pp.299-306.

Taner, M.T. and Koehler, F., 1969, Velocity spectra. Digital computer derivation and applications of velocity functions: *Geophysics,* v.44, pp.1088-1096.

Wu, R.S., and Aki, K., 1985, Scattering characteristics of elastic waves by an elastic heterogeneity: *Geophysics,* v.50, pp.582-595.

Appendix A. Linearization of the Cagniard-de Hoop reflection coefficients and equivalence with the Born reflection coefficient in the case of a single plane interface.

Consider two acoustic half-spaces and a line source situated at a distance z_0 from their interface. The Laplace transform of the wave reflected from the interface at a distance x from the line source and z_0 from the interface can be expressed (e.g., Aki and Richards, 1980) as :

$$\Phi_R(x,0,s)=\frac{F(s)}{\pi}\,\mathrm{Im}\left\{\int_0^{i\infty} e^{-s(px+2\eta_1 z_0)}\frac{R(p)}{2\eta_1}dp\right\}. \qquad (A.1)$$

F(s) is the Laplace transform of the source time function, Im denotes the imaginary parts, R(p) is the reflection coefficient given explicitly by :

$$R(p)=\frac{\rho_2\eta_1-\rho_1\eta_2}{\rho_2\eta_1+\rho_1\eta_2} \qquad \eta_\alpha=\left(\frac{1}{c^2}-p^2\right)^{1/2}$$

where index 1 refers to the half-space containing the source and index 2 to the other one ρ is the density, c the velocity and p the horizontal slowness.

The path of integration can be deformed such that the quantity $px+2\eta_1 z_0$ is real and can be readily identified to time. This allows a direct inversion of the Laplace transform of the reflected wave into the time domain. This is in essence the Cagniard-de Hoop method.

Clayton and Stolt (1981) showed that the reflected wave can be expressed as :

$$D(k_h, k_z) = \frac{k_z^2 + k_h^2}{4k_z^2} \frac{\Delta\kappa}{\kappa}(k_z) + \frac{k_z^2 - k_h^2}{4k_z^2} \frac{\Delta\rho}{\rho}(k_z), \qquad (A.2)$$

with $k_m = 0$ (wavenumber associated with the midpoint coordinate) since there is no variation with midpoint in our case.

$\frac{\Delta\kappa}{\kappa}(k_z)$ and $\frac{\Delta\rho}{\rho}(k_z)$ are the Fourier transforms of the relative variations in depth of, respectively, bulk modulus and density. k_z and k_h are, respectively, the vertical wavenumber and the wavenumber associated with the half-offset h.

If the relative variation of bulk modulus with depth is small enough, the following substitution can be made :

$$\frac{\Delta\kappa}{\kappa} = \frac{\Delta\rho}{\rho} + 2\frac{\Delta c}{c}.$$

Then equation (2) becomes :

$$D(k_h, k_z) = \frac{k_z^2 + k_h^2}{2k_z^2} \frac{\Delta c}{c}(k_z) + \frac{1}{2} \frac{\Delta\rho}{\rho}(k_z).$$

Note that the coefficient of $\frac{\Delta\rho}{\rho}$ is not dependent of k_z or k_h. Raz (1981) followed a different approach in time-space domain and notes similarly the independence of the coefficient of the perturbation in density from the incidence angle. He further takes advantage of this to construct his inversion algorithm for the velocity perturbations.

Consider now that the velocity and density vary as step functions at depth z_0. Their Fourier transforms are :

$$\frac{\Delta\rho}{\rho} = \alpha \frac{e^{ik_z z_0}}{ik_z} \qquad \frac{\Delta c}{c} = \beta \frac{e^{ik_z z_0}}{ik_z}$$

where α and β are the magnitudes of the step. Using the relation :

$$k_h^2+k_z^2=4\frac{\omega^2}{v^2}=-4\frac{s^2}{v^2}$$

we get :

$$D(k_h,s)=\frac{\beta}{2}\frac{\frac{-4s^2}{v^2}}{(k_h^2+4\frac{s^2}{v^2})^{3/2}}e^{-(4\frac{s^2}{v^2}+k_h^2)^{1/2}z_0}-\frac{\alpha}{2}\frac{1}{(k_h^2+4\frac{s^2}{v^2})^{1/2}}e^{-(4\frac{s^2}{v^2}+k_h^2)^{1/2}z_0}.$$

Transforming back over k_h and substituting $k_h=2isp$, we get :

$$D(h,s)=\frac{-1}{2\pi}\int_{-i\infty}^{i\infty}\alpha\frac{ie^{-2s(ph+\eta_1 z_0)}}{4\eta_1}+\beta\frac{ie^{-2s(ph+\eta_1 z_0)}}{4\eta_1(1-v^2p^2)}dp$$

and, using the Schwarz theorem of reflection (Morse and Feschback, 1953) :

$$D(h,s)=\frac{1}{\pi}\mathrm{Im}\left\{\int_0^{i\infty}\frac{1}{2}\left[\alpha+\frac{\beta}{(1-v^2p^2)}\right]\frac{e^{-2s(ph+\eta_1 z_0)}}{2\eta_1}dp\right\}.$$

We can now identify the expression in square brackets with a reflection coefficient and compare it to the exact reflection coefficient:

$$R(p)=\frac{\rho_2\eta_1-\rho_1\eta_2}{\rho_2\eta_1+\rho_1\eta_2}.$$

Suppose that $\rho_2-\rho_1$ is small compared to ρ_1 and that c_2-c_1 is small compared to c_1; the exact reflection coefficient can be expressed as :

$$\rho_2=\rho_1(1+\alpha) \qquad \text{and} \qquad \eta_2=\eta_1\left[1-\frac{\beta}{(1-p^2c_1^2)}\right]$$

where: $\alpha=\frac{\Delta\rho}{\rho_1}$ $\beta=\frac{\Delta c}{c_1}$;

keeping the first order terms in α and β, we get :

$$R(p) \approx \frac{1}{2}\left[\alpha + \frac{\beta}{(1-p^2 c_1^2)}\right].$$

This is exactly the expression we found for the Born approximation. These two approximations are therefore equivalent in the case of a single plane interface. This facilitates the interpretation of the Born approximation for this case, as a linearization of the reflection coefficient with respect to small variations in the densities and velocities of the medium. When the medium is more complex, the Born approximation also involves considering only primary reflections and neglects transmission losses.

Appendix B. WKBJ and far-field Approximations.

The expression for the scattered part of the wavefield in a slowly varying medium, using the WKBJ approximation is given by the following expression :

$$D(x_s,x_g,\omega)=\int_\Omega d\Omega \frac{[\rho(z)\rho(z_g)]^{1/2}}{2\pi}\int dk_g\, e^{ik_g(z_g-z)} e^{i\int_{z_g}^{z_{Pg}} du\ q_g(u)+i\frac{\pi}{4}} \frac{\cos\left(\int_{z_{Pg}}^{z} du q_g(u)-\frac{\pi}{4}\right)}{2[q(z)q(z_g)]^{1/2}}$$

$$[\omega^2\frac{a1}{\kappa}+\nabla\cdot\frac{a2}{\rho}\nabla]\frac{[\rho(z)\rho(z_s)]^{1/2}}{2\pi}\int dk_s\, e^{ik_s(z-z_s)} e^{i\int_{z_s}^{z_{Ps}} du\ q_s(u)+i\frac{\pi}{4}} \frac{\cos\left(\int_{z_{Ps}}^{z} du q_s(u)-\frac{\pi}{4}\right)}{2[q(z)q(z_s)]^{1/2}}.$$

The notation z_{Ps} is used for the turning point corresponding to the ray joining the source point $(x_s,0)$ to the current point (x,z). The notation z_{Pg} is used for the turning point of the ray joining the current point to the geophone. The cosine has been chosen so that the solution to the WKBJ equation decays with depth under the turning point (e.g., Aki and Richards, 1980). We integrate by parts with respect to the x and z variables and suppose that :

$$[G(x_g,0;x,z)V(x,z)G(x,z;x_s,0)]_{\partial\Omega}=0,$$

where $\partial\Omega$ denotes the boundary of the area Ω. This condition is achieved if the anomalies are supposed to be totally contained within the area Ω where we want to image them. Since the source and geophone are at the surface, the scattered field is then expressed as :

$$D(x_s, x_g, \omega) = \int_\Omega d\Omega \frac{\rho(z)\rho(0)}{4\pi^2}$$

$$\int dk_g \int dk_s \, e^{ik_s(x-x_s)+k_g(x_g-x)} e^{i\int_{z_s}^{z_{P_s}} du \; q_s(u)+i\frac{\pi}{4}} \frac{\cos\left(\int_{z_{P_s}}^{z} du \; q_s(u)-\frac{\pi}{4}\right)}{2i\,[q_s(0)q_s(z)]^{1/2}}$$

$$\left\{\omega^2 \frac{a\,1}{\kappa}+[k_g\, k_s - q_s(z)q_g(z)]\frac{a\,2}{\rho}\right\} e^{i\int_{z_g}^{z_{P_g}} du \; q_g(u)+i\frac{\pi}{4}} \frac{\cos\left(\int_{z_{P_g}}^{z} du \; q_g(u)-\frac{\pi}{4}\right)}{2i\,[q_g(0)q_g(z)]^{1/2}}$$

An asymptotic approximation can be applied to the two integrals over wavenumbers k_s and k_g. The two integrals are sums of terms of the form :

$$I(\omega) = \int_{-\infty}^{\infty} dp \; \omega p F(p) e^{i\omega G(p)}$$

where :

$$\omega p = k \quad \text{and} \quad G(p) = px + \int_0^{z_P} \gamma(z)\, dz \pm \int_{z_P}^{z} \gamma(z)\, dz$$

where :

$$\gamma(z) = \left(\frac{1}{v^2} - p^2\right)^{1/2}.$$

The main contribution for large frequencies in the integral can be estimated using the stationary phase method. The stationary points are obtained for $\frac{\partial G}{\partial p} = 0$. This can be interpreted physically as the Fermat principle for a ray joining the source and receiver points. It says that the travel time (to which $G(p)$ can be identified) is minimum for the ray parameters p_0 that satisfy the stationary condition. It is possible for several ray parameters to satisfy this condition for a pair of source and receiver points. This corresponds physically to multipathing. In some cases, no

stationary point exists for the integral. This happens in shadow zones. In this calculation, we suppose there is no multipathing between the two points and no shadow zone for the background velocity model chosen.

Depending on whether the ray joining the pair of points passes through a turning point or not, the stationary condition is going to be reached for $G(p)$ in the term of the sum that has a positive sign in the exponential or a negative sign. The stationary phase theorem says that the integral can be approximated by the following expression for large frequencies :

$$\omega F(p_0)\left[\frac{2\pi}{\omega\left|\frac{\partial^2 G}{\partial p^2}\right|_{p_0}}\right]^{1/2} e^{i\omega G(p_0)} e^{\pm i\frac{\pi}{4}}$$

where the $\pm$ is according to the sign of the second derivative of G with respect to p. Then we note that (e.g., Aki and Richards, 1980):

$$\frac{\partial^2 G}{\partial p^2} = -\left(\frac{\partial x}{\partial p}\right)_{p_0}.$$

The term on the right-hand side of the equation is part of the geometric spreading term. Applying the formula to both integrals over wavenumbers, we get the following expression for the high frequency scattered wavefield within the Born approximation :

$$D(x_s, x_g, \omega) \rightarrow \int_\Omega d\Omega \frac{\rho(0)\rho(z)}{\left[\gamma_s(0)\gamma_s(z)\right]^{1/2}\left[\gamma_g(0)\gamma_g(z)\right]^{1/2}}$$

$$\frac{\left[\frac{a1}{\kappa(0)} + \frac{a2}{\rho(0)}(p_s p_g - \gamma_s \gamma_g)\right]}{\left|\frac{\partial x}{\partial p}\right|_{p_s}^{1/2}\left|\frac{\partial x}{\partial p}\right|_{p_g}^{1/2}} (-i\omega) S(\omega) \frac{e^{i\omega(t1+t2)}}{8\pi}$$

where $t1$ is the travel time between the source and current point of integration and $t2$ the travel time between the current point of integration and the geophone. p_s is the value of p for which the integral over the source wavenumber k_s is stationary. Similarly, p_g is the value of p for which the geophone wavenumber integral is stationary. γ_s and γ_g are the values of γ for $p = p_s$ and $p = p_g$, respectively.

Thus the expression we derived for the scattered field under the assumptions of the Born approximation and the far-field, or high frequency approximation consists simply of a phase term and an amplitude term. The phase term represents the travel times between the source, scattering point and receiver. The amplitude term is made of two factors. The first factor is the geometrical spreading of the classical ray theory and the second factor is the Born reflection coefficient term that depends on the density and bulk modulus of the medium.

The inverse Fourier transform of the wavefield is trivially computed and the final result for the wavefield in the time and physical domain is :

$$D(x_s, x_g, t) = \int_{\Omega} d\Omega \quad A(x_s, x_g, x) \left[a1 + a2\cos\theta \right] \dot{S}(t - t1 - t2).$$

where θ is the angle between incident and scattered rays at the scatterer. t_1 and t_2 are, respectively, the travel times between the source and scatterer and between the scatterer and the receiver. $A(x_s, x_g, x)$ is the amplitude factor due to geometrical spreading.

Appendix C. The Born elastic scattering coefficients.

Equation (4.12) in the text gives the expression for the scattered wavefield. It is made up of propagation terms between the source and scatterers on one hand and the scatterers and receiver on the other hand, and of a scattering potential term (V). It can be further separated into four terms. Each of the four terms represents the contribution of one type of scattered wave as discussed in the text. From the first term, we isolate the following expression :

$$\begin{pmatrix} 1 & 0 \\ 0 & 0 \end{pmatrix} \begin{pmatrix} ik_g & i\nu_g \\ -i\nu_g & ik_g \end{pmatrix} V(k_g, -\nu_g \mid k_s, \nu_s) \begin{pmatrix} ik_s & i\nu_s \\ -i\nu_s & ik_s \end{pmatrix} \begin{pmatrix} 1 & 0 \\ 0 & 0 \end{pmatrix}$$

where q has been replaced by ν which corresponds to the ray joining the source to the scatterer for ν_s, and the scatterer to the receiver for ν_g. This comes from the assumption of far-field approximation. Replacing V by its explicit expression (Appendix E), and going through the algebra the above expression becomes:

$$R_{PP} \begin{pmatrix} 1 & 0 \\ 0 & 0 \end{pmatrix}$$

where:

$$R_{PP} = a_1(k_g k_s + \nu_g \nu_s) - a_2(k_s^2 + \nu_s^2)(k_g^2 + \nu_g^2) + 2a_3(k_g \nu_s - \nu_g k_s)^2.$$

In the same way, the three other scattering coefficients can be computed and we obtain the following results :

$$R_{SP}\begin{pmatrix}0 & 1\\ 0 & 0\end{pmatrix}, \quad R_{PS}\begin{pmatrix}0 & 0\\ 1 & 0\end{pmatrix}, \quad R_{SS}\begin{pmatrix}0 & 0\\ 0 & 1\end{pmatrix}$$

where :

$$R_{SP} = a_1(-k_g\,\eta_s + k_s\,\nu_g) - 2a_3\frac{\beta^2}{\omega^2}\left[\nu_g\,k_g\,(k_s^2-\eta_s^2) + k_s\,\eta_s\,(\nu_g^2-k_g^2)\right]$$

$$R_{PS} = a_1(-\eta_g\,k_s + \nu_s\,k_g) + 2a_3\frac{\beta^2}{\omega^2}\left[k_s\,\nu_s\,(k_g^2-\eta_g^2) + k_g\,\eta_g\,(\nu_s^2-k_s^2)\right]$$

$$R_{SS} = a_1(k_s\,k_g + \eta_s\,\eta_g) + a_3\frac{\beta^2}{\omega^2}\left[(k_s\,k_g + \eta_s\,\eta_g)^2 + (k_s\,\eta_g - k_g\,\eta_s)^2\right].$$

When the far-field approximation is computed for the integrals over wavenumber, the expressions for the above scattering coefficients are simplified. If the following angles are introduced, where θ_1 is the angle formed between the vertical and the incident wave and θ_2 the angle between the vertical and the scattered wave:

$$\sin\theta_1 = \frac{\alpha}{\omega}\,k_s\cos\theta_1 = \frac{\alpha}{\omega}\,\nu_s\sin\theta_2 = \frac{\alpha}{\omega}\,k_g\cos\theta_2 = \frac{\alpha}{\omega}\,\nu_g$$

for incident and scattered P waves.

$$\sin\lambda_1 = \frac{\beta}{\omega}\,k_s\cos\lambda_1 = \frac{\beta}{\omega}\,\eta_s\sin\lambda_2 = \frac{\beta}{\omega}\,k_g\cos\lambda_2 = \frac{\beta}{\omega}\,\eta_g$$

for incident and scattered S waves.

Using these relations in the expressions for the four scattering coefficients, it becomes clear that the scattering coefficients depend only on the angle between incident and scattered wave that we call θ:

$$R_{PP} = \left[a_1\cos\theta - a_2 + 2\frac{\beta^2}{\alpha^2}\,a_3\sin^2\theta\right]\frac{\omega^2}{\alpha^2}$$

$$R_{PS} = \left[a_1\sin\theta \qquad -\frac{\beta}{\alpha}\,a_3\sin 2\theta\right]\frac{\omega^2}{\alpha\beta}$$

$$R_{SP} = \left[-a_1 \sin\theta \qquad + \frac{\beta}{\alpha} a_3 \sin 2\theta \right] \frac{\omega^2}{\alpha\beta}$$

$$R_{SS} = \left[a_1 \cos\theta \qquad + a_3 \cos 2\theta \right] \frac{\omega^2}{\beta^2}.$$

Appendix D. Comparison of our expressions for the scattering coefficients with Wu and Aki's (1985) expressions.

Wu and Aki (1985) gave expressions for the scatterred wave due to the interaction between an incident plane wave and a spherical inclusion in an elastic medium. Under the Born approximation, their expressions should compare to ours (Appendix C), taking into account that they are for a three-dimensional inclusion and that his coordinate system is slightly different. Setting the azimuthal angle to zero, we get the expressions for the reflection coefficient part of Wu and Aki's expressions for an incident plane P wave :

$$U^{PP} = \frac{\delta\rho}{\rho}\cos\theta - \frac{\delta\lambda}{\gamma} - 2\frac{\delta\mu}{\gamma}\cos^2\theta.$$

Since $\delta\gamma = \delta\lambda + 2\delta\mu$

$$U^{PP} = \frac{\delta\rho}{\rho}\cos\theta - \frac{\delta\gamma}{\gamma} + 2\frac{\delta\mu}{\gamma}\sin^2\theta$$

$$= \frac{\delta\rho}{\rho}\cos\theta - \frac{\delta\gamma}{\gamma} + 2\frac{\delta\mu}{\mu}\frac{\beta^2}{\alpha^2}\sin^2\theta,$$

and :

$$U^{PS} = -\frac{\delta\rho}{\rho}\sin\theta + \frac{\beta}{\alpha}\frac{\delta\mu}{\mu}\sin 2\theta.$$

These expressions compare with equations (4.17) and (4.18) in the text if we change the sign of θ, since we used the opposite convention for it.

For an S incident wave , his expressions are :

$$U^{SP} = \frac{\delta\rho}{\rho}\sin\theta' - \frac{\beta}{\alpha}\frac{\delta\mu}{\mu}\sin 2\theta' ,$$

and for the S to S scattered wave:

$$U^{SS} = \frac{\delta\rho}{\rho}\cos\theta' + \frac{\delta\mu}{\mu}\cos 2\theta' .$$

In this case, their chose a coordinate system where the zero of the θ' angle is the direction of polarization of the incident S wave. This angle relates to our θ as $\theta' = \theta - \frac{\pi}{2}$ and therefore our expressions are equivalent to theirs.